

# Rhenium–Osmium Isotope and Platinum-Group Element Constraints on the Origin and Evolution of the 1.27 Ga Muskox Layered Intrusion

JAMES M. D. DAY<sup>1,2\*</sup>, D. GRAHAM PEARSON<sup>1</sup> AND LARRY J. HULBERT<sup>3</sup>

<sup>1</sup>DEPARTMENT OF EARTH SCIENCES, UNIVERSITY OF DURHAM, SCIENCE LABORATORIES, SOUTH ROAD, DURHAM DH1 3LE, UK

<sup>2</sup>DEPARTMENT OF GEOLOGY, UNIVERSITY OF MARYLAND, COLLEGE PARK, MD 20742, USA

<sup>3</sup>GEOLOGICAL SURVEY OF CANADA, 601 BOOTH STREET, OTTAWA, ONT. K1A 0E8, CANADA

RECEIVED MAY 22, 2007; ACCEPTED APRIL 18, 2008  
ADVANCE ACCESS PUBLICATION MAY 25, 2008

Platinum-group element (PGE: Os, Ir, Ru, Pt, Pd) and Re–Os isotope systematics determined for the entire preserved stratigraphy of the 1.27 Ga Muskox intrusion provide an exceptional view of magma chamber processes and mineralization in the main plutonic system of the Mackenzie large igneous province (LIP). We present new Re–Os isotope data for the intrusion, together with PGE and trace element abundances, and oxygen and Sm–Nd isotope data on samples that include local crustal materials, layered series peridotites, stratiform chromitites, marginal and roof zone rocks, and the Muskox Keel feeder dyke. Intrusive rocks span wide ranges in initial isotopic compositions ( $\gamma_{Os,i} = +1.0$  to  $+87.6$ ;  $\epsilon_{Nd,i} = -0.4$  to  $-6.6$ ;  $\delta^{18}O_{O_i} = +5.5$  to  $+6.9\%$ ) and highly siderophile element abundances (HSE: PGE and Re; Re =  $0.02$ – $105$  ppb; Pt =  $0.23$ – $115$  ppb; Os =  $0.02$  to  $> 200$  ppb). HSE and fluid-immobile trace element abundance variations are consistent with relative compatibilities expected for cumulate rocks. The most radiogenic Os and unradiogenic Nd isotope compositions occur in the Muskox marginal and roof zones. Negative  $\gamma_{Os,i}$  values in these rocks and their non-isochronous relations result from mobilization of Re in the intrusion through post-magmatic hydrothermal processes. The most significant process causing Os and Nd isotope variations in the layered series of the intrusion is crustal contamination of mantle-derived magma batches feeding individual cyclic units. This process may be directly responsible for formation of chromitite horizons within the intrusion. Accounting for crustal assimilation, the Muskox intrusion parental magma has  $\gamma_{Os,i} = +1.2 \pm 0.3$ ,  $\epsilon_{Nd,i} > -1.0 \pm 0.4$ ,  $\delta^{18}O \sim +5.5\%$  and HSE abundances similar to those expected from

$\geq 15\%$  partial melting of the Mackenzie LIP mantle source. This composition is similar to that calculated for 1.27 Ga primitive upper mantle. Parental magmas were probably derived from a mantle source unaffected by long-term, large-scale melt depletion, with no appreciable input from recycled crust and lithosphere, or putative core contributions.

KEY WORDS: chromitite seams; crustal contamination; mantle source; Muskox layered intrusion; O; Re–Os; Sm–Nd; isotopes; platinum-group elements (PGE); sulphide

## INTRODUCTION

A long-standing debate in geology has been the relative roles played by the Earth's crust and mantle in generating the geochemical signatures of large igneous provinces (LIPs), and the influence these reservoirs have in the formation of mineral deposits in magmatic systems. Layered intrusions are central for addressing these issues, because they record periods of magmatic activity intimately associated with LIPs, and generally host precious metal mineralization within the system. Application of the Re–Os isotope system to these problems has allowed effective discrimination of crustal and mantle signatures, because Re and Os track the behaviour of the platinum-group element [PGE; Os, Ir, Ru, Rh, Pt, Pd—with Re and Au collectively

\*Corresponding author. Telephone: +1 301-405-2707.  
E-mail: jamesday@geol.umd.edu

termed highly siderophile elements (HSE)] enrichments more faithfully than lithophile isotope systems (e.g. Lambert *et al.*, 1989, 1994, 1998; Marcantonio *et al.*, 1993; Walker *et al.*, 1994, 1997a; Puchtel *et al.*, 1999; Schoenberg *et al.*, 1999, 2003; Hanski *et al.*, 2001; Horan *et al.*, 2001; Marques *et al.*, 2003). Furthermore, in contrast to the less than 200 Myr snapshot provided by ocean island basalts, LIP magmatism has occurred over much of Earth history, providing important constraints on the secular evolution of the terrestrial mantle.

Here, we present a new major- and trace-element, HSE, and Os–Nd–O isotope study of the Muskox intrusion in northern Canada. Several characteristics of the Muskox intrusion make it attractive for study. First, it is well developed and structurally undeformed and features a complete rock differentiation series from dunite cumulates, peridotites, pyroxenites, and gabbros, to granophyres. Second, it is one of the most ultramafic large layered intrusions so far recognized on Earth and has been considered to be related in space and time to the extensive 1.27 Ga giant Mackenzie dyke swarm and Coppermine River continental flood basalts (CFB) (Baragar, 1969; Francis, 1994; Baragar *et al.*, 1996; Day *et al.*, 2003b), collectively known as the Mackenzie LIP. Detailed geochemical study of the Muskox intrusion is therefore likely to provide important insights into the process of crustal contamination of mantle-derived magmas feeding flood basalt magmatism. The Mackenzie LIP event also coincides with a period in the geological record that is poorly constrained in the context of Os isotope mantle evolution models. In this study, the effects of magma chamber processes (assimilation, magma-mixing through recharge) are considered on the isotopic and elemental compositions of Muskox intrusion rocks. We explore the implications this has for understanding modification of mantle-derived melts and generation of chromitite horizons in layered intrusions, and examine the origin and possible effects of secondary hydrothermal processes on the distribution of the PGE in the intrusion. Finally, we consider the HSE, Nd and O isotope compositions of the mantle source of the Mackenzie LIP, and constraints that can be placed on the mantle Re–Os isotope evolution curve.

## THE MUSKOX INTRUSION: GEOLOGICAL SETTING AND SAMPLE DETAILS

The Muskox intrusion is situated at the edge of the Bear structural province, on the northwestern edge of the Canadian Shield (Fig. 1), and is a classic example of an upper crustal layered intrusion. It forms part of the mid-Proterozoic Mackenzie LIP, which comprises the Coppermine River CFB, and the largest preserved terrestrial dyke swarm, the Mackenzie dykes (Ernst *et al.*, 1995).

Combined volumes estimated for the structural components of the Mackenzie LIP indicate that it is one of the most extensive LIPs recognized.

The geology and structure of the Muskox intrusion has been described in detail previously (Findlay & Smith, 1965; Irvine & Smith, 1967; Francis, 1994) and its stratigraphy is summarized in Fig. 2. The intrusion was emplaced into the Coppermine Homocline (Hofmann, 1980; Kerans *et al.*, 1981), an Aphebian basement complex of >1.8 Ga Wopmay para- and ortho-gneiss, metavolcanic rocks and metasediments at the base of the 3–5° northward dipping Helikian sequence. The overall structure of the intrusion is that of a giant funnel-shaped dyke (~125 km long, 11 km wide in the north, and 0.1 km wide in the south) that merges into a vertical dyke extending to the south, known as the Keel feeder dyke (Fig. 3). Aeromagnetic and gravity anomaly studies show the intrusion extends northward for at least 250 km under younger cover where it becomes more laterally extensive (Fig. 1). The present exposure probably represents a thin, oblique slice through a much larger intrusion (Francis, 1994), with an estimated original volume in excess of 20 000 km<sup>3</sup>. The intrusion can be divided into a 'Keel' feeder dyke, two marginal zones (east and west), a layered series composed entirely of cumulates, and a granophyric roof zone (Irvine, 1980). Twenty-five cyclic units have been identified within the layered series (Findlay & Smith, 1965; Irvine & Smith, 1967), which have been interpreted as replenishment episodes of mantle-derived mafic magma. Two thin (<10 cm) stratiform chromitite horizons occur in the intrusion, in the middle of cyclic unit 21 and at the base of cyclic unit 22. In this study, the chromitite unit at the base of cyclic unit 22 was analysed. In addition to these horizons, a laterally discontinuous lower chromitite layer has been inferred based on cryptic chemical variations (L. J. Hulbert, unpublished data; DDH-MX-S-137; hereafter all samples listed in Table 1 are abbreviated to their drill-hole number, e.g. S-137).

Emplacement of the Muskox intrusion occurred early in the Mackenzie event and has been precisely dated using baddeleyite–zircon U–Pb dating, at 1269 ± 1 Ma (LeCheminant & Heaman, 1989; French *et al.*, 2002). This age is within error of that for the giant Mackenzie diabase dyke swarm (1267 ± 2 Ma; LeCheminant & Heaman, 1989), although field relations indicate that the dykes cross-cut parts of the intrusion (Findlay & Smith, 1965) and hence the Muskox intrusion is probably one of the earliest parts of the system (LeCheminant & Heaman, 1989). Re–Os isochron (Day *et al.*, in preparation) and zircon U–Pb ages (M. Hamilton, personal communication, 2004), for the lower portions of the Coppermine River CFB are within error of the Muskox intrusion age, suggesting that the inception of the CFB and emplacement of the intrusion were essentially contemporaneous and that

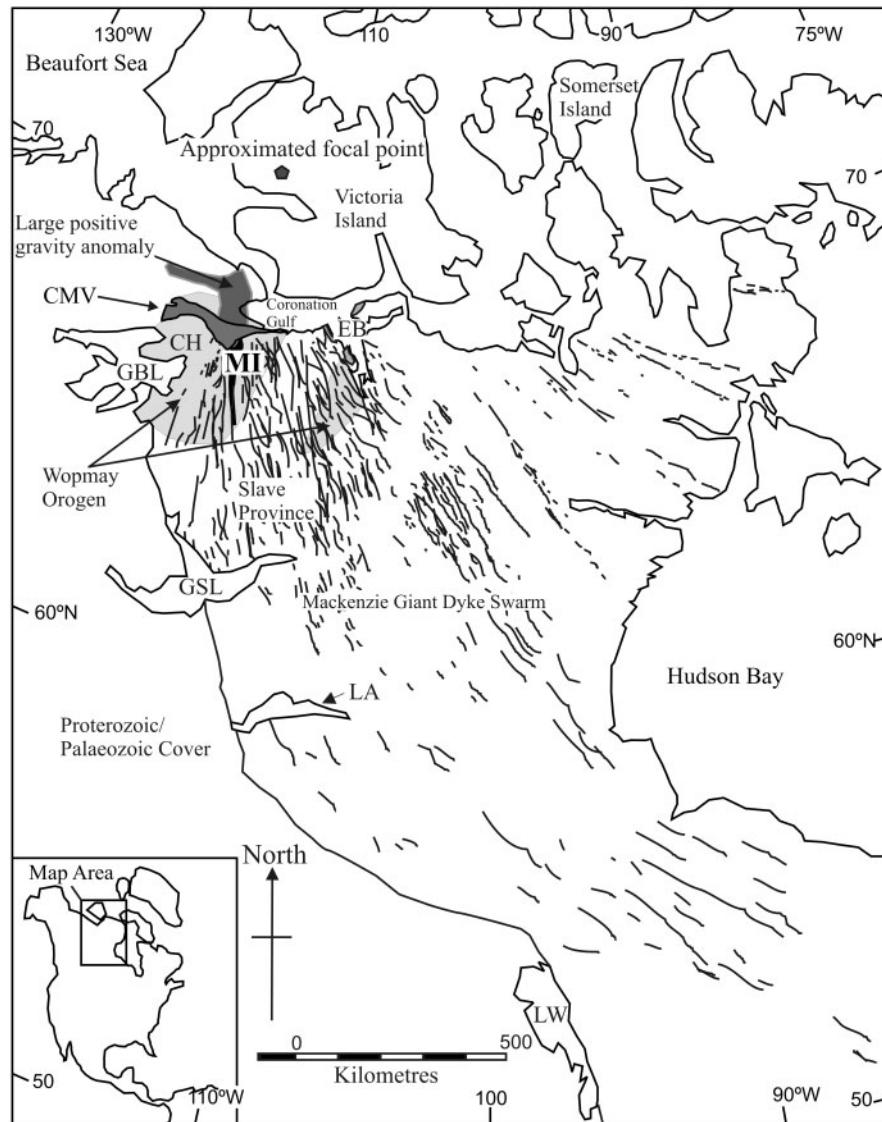


**Fig. 1.** Map of the Mackenzie large igneous province, including the Mackenzie Giant Dyke Swarm and Coppermine Volcanics (CMV) continental flood basalts and location of the Muskox intrusion (MI). Approximate focal point for  $\sim 1.27$  Ga igneous activity and the large positive gravity anomaly associated with the intrusion are from Baragar *et al.* (1996). EB, Ekalulia basalts; CH, Coppermine homocline; GBL, Great Bear Lake; GSL, Great Slave Lake; LA, Lake Athabasca; LW, Lake Winnipeg. Modified from LeCheminant & Heaman (1989).

volcanic and plutonic activity occurred over a similar time-span to other LIP magmatic systems (e.g. Hamilton *et al.*, 1998).

Fifty-seven samples were analysed for major- and trace-element analysis, with 41 selected for Re–Os isotope and HSE abundance analysis (29 for Sm–Nd isotopes compositions; nine for O isotope analysis of mineral separates) from a large ( $\sim 600$  samples), well-characterized suite from the Muskox Drilling Project (Findlay & Smith, 1965). All initial sample masses exceeded 100 g, and were selected in 2001 from materials preserved at the Geological Survey of Canada, Ottawa. The majority of

samples were from the north and south diamond drill-hole cores, which preserve a  $>1800$  m thick stratigraphy of the Muskox intrusion. Relative locations of samples within the drill cores are shown in Fig. 2, and the lithology, petrology, degree of alteration (e.g. serpentinization) and locations of samples are given in Table 1. Outcrop samples of three Keel dyke and three main chromitite specimens, as well as drill-core samples of the 1.66 Ga Hornby Bay sandstone roof rock (Bowring & Ross, 1985), and the  $>1.8$  Ga Wopmay Orogen paragneiss basement country rock (Hofmann, 1980) were also analysed for their Os–Nd isotope and HSE compositions.

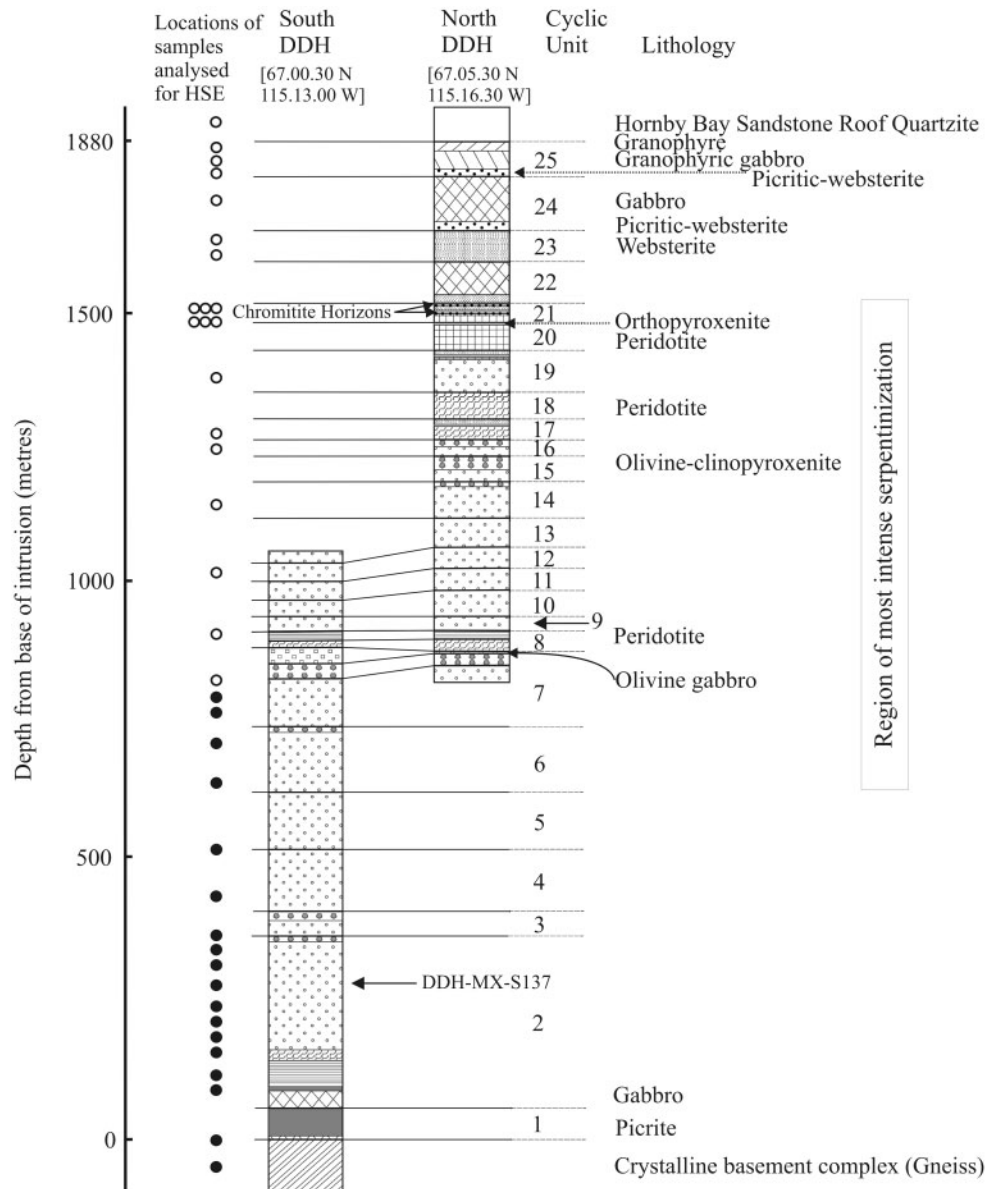


**Fig. 2.** Stratigraphy of the Muskox intrusion drill-core sections with positions of samples analysed for Re–Os isotopes and HSE (●, south diamond drill-hole (DDH); ○, north DDH) and location of the heavily serpentinized zone within the intrusion [based on data from Chamberlain (1967)]. The location of Chamberlain's heavily serpentinized zone matches well with petrographic observations (Table 1) and total measured water contents for the samples (Table 3). Cross-cutting diabase dykes have been omitted from the diagram for clarity. Francis (1994) has further subdivided portions of the intrusion into megacycle 1 (cyclic units 2 and 3), megacycle 2 (cyclic units 4–8), megacycle 3 (cyclic units 9–19) and megacycle 4 (cyclic units 20–25). Further detailed description of the drill core and samples has been given by Findlay & Smith (1965).

## ANALYTICAL METHODS

Major elements and S were analysed using standard X-ray fluorescence fusion and S analysis techniques at the Geological Survey of Canada (GSC); major elements have been corrected to anhydrous proportions. Trace element concentrations were determined by digesting 100 mg of sample powder prior to analysis by inductively coupled

plasma-mass spectrometry (ICP-MS) using an ELAN 6000 quadrupole ICP-MS system at the University of Durham, following procedures outlined by Ottley *et al.* (2003). Data quality was ensured via repeated analysis of in-house standards and international reference materials (W2, BHVO-1, AGV-1, BE-N, BIR-1, SRM 688), together with regular monitoring of total procedural blanks. Internal and external reproducibility of standard values

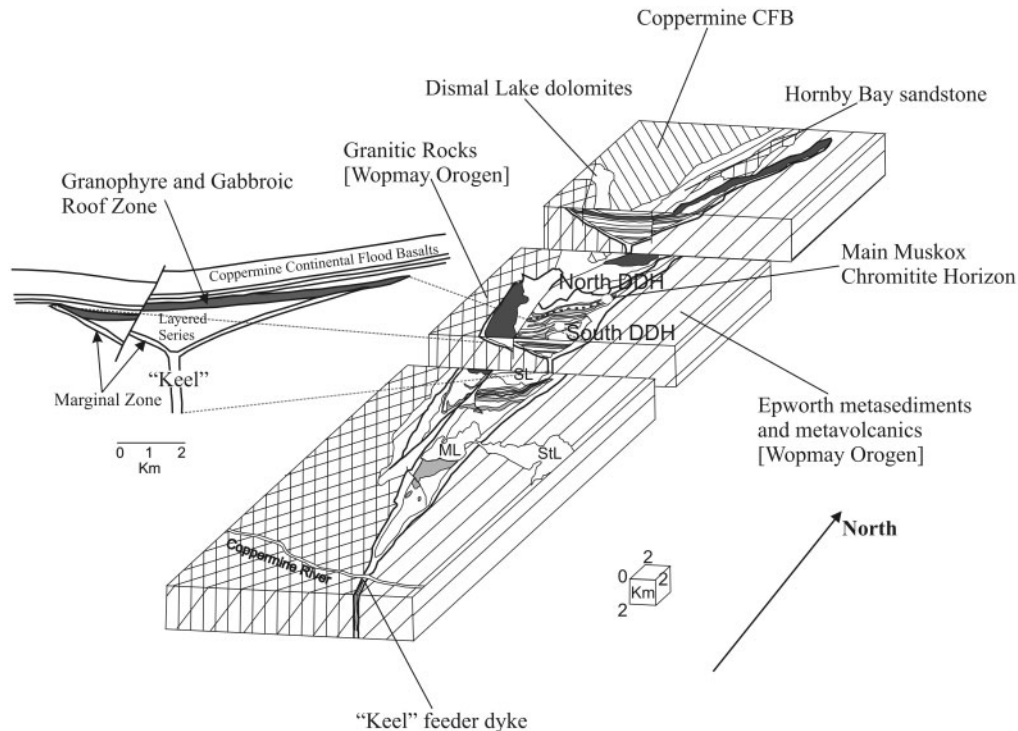


**Fig. 3.** Exploded block diagram of the Muscox intrusion, showing its structural relations with country rocks, including >1.8 Ga Wopmay Orogen rocks, 1.66 Ga Hornby Bay sandstone and younger Dismal Lake dolomites. Also shown is a restored cross-section of the exposed portions of the intrusion and the location of the north (north DDH) and south (south DDH) diamond drill-holes [modified from Irvine & Smith (1967) and Irvine (1980)]. Stanbridge (StL), McGregor (ML) and Speers (SL) lakes also shown.

was better than  $\pm 3\%$  for all elements, except Pb and Sc, which were better than  $\pm 5\%$ .

Oxygen isotope analyses were performed on visibly 'fresh', inclusion-free mafic minerals. These were separated by hand and ultrasonically cleaned in MQ-H<sub>2</sub>O and methanol.  $\delta^{18}\text{O}$  values  $\{\delta^{18}\text{O}_n$  is the per mil (‰) deviation of  $^{18}\text{O}/^{16}\text{O}$  in  $n$  from the international standard (std) V-SMOW, given by the relationship  $\delta^{18}\text{O}_n = 1000 \times [({}^{18}\text{O}/^{16}\text{O}_n)/({}^{18}\text{O}/^{16}\text{O}_{\text{std}}) - 1]\}$ , were measured at Royal Holloway, University of London on 1–2 mg splits using the laser fluorination protocols of Matthey & Macpherson (1993) for silicates and Lowry *et al.* (2003) for oxides. Yields for all unknowns and standards in this study were  $95 \pm 5\%$ . Precision and accuracy of analyses was monitored with three internal standards: two olivines from San Carlos and a garnet. The isotopic composition of these minerals relative to the international standard biotite NBS-30, and  $2\sigma$  deviations of replicate analyses over the analytical period were: RHUL SCOL I  $+4.84\%$  ( $\pm 0.18$ ,  $n=23$ ), RHUL SCOL II  $+5.22\%$  ( $\pm 0.16$ ,  $n=19$ ) and UW GMG 2 garnet  $+5.71\%$  ( $\pm 0.18$ ,  $n=22$ ).

Nd isotope analyses were performed at the University of Durham, using 0.1–0.5 g of powder that was digested in Savillex Teflon beakers in a 4:1 HF–HNO<sub>3</sub> mixture for 72 h on a hotplate, at 150°C. Neodymium was separated using Bio-Rad® AG50W-X8 cation resin. Procedures for

obtaining Nd-bearing fractions from this column procedure have been outlined previously (Dowall *et al.*, 2003). Sample solutions were measured by multi-collector (MC)-ICP-MS on a Neptune® system and were introduced into the plasma using an Elemental Scientific Inc. (ESI) PFA-50 microflow nebulizer and an ESI dual cyclonic Scott double pass (CSDP) quartz spray chamber. Typical sample uptake rates were 70–100  $\mu\text{l}/\text{min}$ . Each analysis is based on the average of 50 measurement cycles with an integration time of 4.1 s per cycle. Repeat measurements of  $^{143}\text{Nd}/^{144}\text{Nd}$  for undoped and Sm-doped 200 ppb Johnson & Matthey (J&M) standards for two analytical sessions were  $0.511108 \pm 15$  ( $2\sigma$ ,  $n=10$ ) and  $0.511116 \pm 17$  ( $2\sigma$ ,  $n=21$ ). Samples are normalized to a nominal J&M  $^{143}\text{Nd}/^{144}\text{Nd}$  standard value of 0.511111. This level of reproducibility and accuracy is in line with the long-term performance of the Durham Neptune® (Pearson & Nowell, 2005). Blank and yield data for Nd preparation chemistry have been given by Dowall *et al.* (2003). Sm and Nd concentrations were measured using an ELAN 6000 ICP-MS system. The reproducibility of Sm/Nd ratios using this procedure for ultramafic rocks was estimated by analysis of in-house peridotite standard GPI3 and is 1.8% ( $2\text{ SD}$ ; Ottley *et al.*, 2003). This gives a typical uncertainty on age-corrected  $\epsilon_{\text{Nd}}$  ratios of 0.38% ( $2\sigma$ ).

Table 1: Lithology, petrology, degree of alteration and locations of Muskox intrusion samples

| Sample <sup>1</sup>  | DFB <sup>2</sup> | Rock type               | Cyclic unit <sup>3</sup> | Texture <sup>4</sup>      | Mineral phases <sup>5</sup>                     |
|--|------------------|-------------------------|--------------------------|---------------------------|---|
| <i>Muskox north diamond drill hole—67°05'30"N, 115°16'30"W</i> |                  |                         |                          |                           |   |
| DDH-MX-N-1   | 1880.7           | Hornby Bay sandstone    | CR                       | Statically recrystallized | Qtz (95), Chl, Mu, Cal                          |
| DDH-MX-N-3   | 1878.0           | Granophytic gabbro      | 25 (35)                  | Coarsely crystalline      | K-Fd (60), Qtz (15), Chl (15), Mt (8), Cal, Cpy |
| DDH-MX-N-11  | 1834.7           | Granophytic gabbro      | 25 (35)                  | Crystalline granophytic   | K-Fd, Px, Ol, Mt, Pl, Qtz, Bt, Chl, Cal, Ser    |
| DDH-MX-N-14  | 1821.3           | Picritic websterite     | 25 (34)                  | Granophytic               | Ser, Cal, Chl, Tit, Ep, Ilm?, Qtz               |
| DDH-MX-N-18  | 1800.9           | Gabbro                  | 24 (33)                  | Heterocumulate            | Pl, Cpx, Opx, Mt, Bt, C, Qtz, Mu                |
| DDH-MX-N-27  | 1746.3           | Gabbro                  | 24 (33)                  | Granophytic               | Pl, Cpx, Opx, Qtz, Mt, Cal, Chl, Bt             |
| DDH-MX-N-35  | 1700.3           | Websterite              | 23 (31)                  | Granophytic               | Pl, Cpx, Mt, Ser, C                             |
| DDH-MX-N-46  | 1633.6           | Websterite              | 23 (31)                  | Granophytic               | Pl, Cpx, Opx, Mt, Ep, Cal, Bt, Chl veins        |
| DDH-MX-N-54  | 1571.4           | Websterite              | 22 (29)                  | Orthocumulate             | Opx, Cpx, Ser, C, Mt, Pl                        |
| DDH-MX-N-55  | 1568.2           | Websterite              | 21 (27)                  | Mesocumulate              | Cpx, Opx, Mt, Ser, Cal, Bt                      |
| DDH-MX-N-56  | 1564.4           | Websterite              | 21 (27)                  | Granular                  | Cpx, Opx, Pl, Cal                               |
| DDH-MX-N-59  | 1542.7           | Peridotite              | 21 (26)                  | Orthocumulate             | Ser, Cpx, Ol, Cr, Chl                           |
| DDH-MX-N-66  | 1505.2           | Peridotite              | 20 (24)                  | Orthocumulate             | Ser, Cpx, Cr, Mt, Opx, Chl, Ol                  |
| DDH-MX-N-75  | 1458.3           | Dunite                  | 19 (21)                  | Mesocumulate              | Ser, Cr (2), Chl, Mu, Fe*                       |
| DDH-MX-N-85  | 1397.4           | Peridotite              | 18 (20)                  | Mesocumulate              | Ser, Cr, Mt, Bt, Cpx                            |
| DDH-MX-N-97  | 1334.0           | Peridotite              | 17 (18)                  | Mesocumulate              | Ser, Cr, Mt, Chl                                |
| DDH-MX-N-100   | 1307.3           | Olivine clinopyroxenite | 16 (17)                  | Adcumulate                | Cpx (>80), Ser, Ol, Mt                          |
| DDH-MX-N-101   | 1302.5           | Olivine clinopyroxenite | 16 (17)                  | Adcumulate                | Cpx (>70), Ser, Ol, Cr                          |
| DDH-MX-N-104   | 1288.2           | Peridotite              | 16 (16)                  | Ad/Meso-cumulate          | Ser, Cpx, Cr, Mt                                |
| DDH-MX-N-111   | 1232.2           | Dunite                  | 15 (14)                  | Ad/Meso-cumulate          | Ser, Cpx, Cr, Mt, Bt, Chl                       |
| DDH-MX-N-115   | 1214.5           | Dunite                  | 14 (12)                  | Mesocumulate              | Ser, Cr, Cpx, Mt, Bt                            |
| DDH-MX-N-122   | 1171.8           | Dunite                  | 14 (12)                  | Ad/Meso-cumulate          | Ser, Mt, Cr, Bt, Chl                            |
| DDH-MX-N-129   | 1061.5           | Dunite                  | 12 (12)                  | Mesocumulate              | Ser, Mt, Cr, Chl, Fe*                           |
| DDH-MX-N-141   | 990.8            | Dunite                  | 11 (12)                  | Adcumulate                | Ser, Mt, Cr, Tit, Chl, Fe*                      |
| DDH-MX-N-151   | 936.5            | Dunite                  | 8 (11)                   | Orthocumulate             | Ser, Cpx, Ol, Pl, Cal                           |
| DDH-MX-N-157   | 893.5            | Olivine clinopyroxenite | 7 (8)                    | Orthocumulate             | Cpx, Ser, Mt, Chl                               |
| <i>Muskox south diamond drill hole—67°00'30"N, 115°13'00"W</i> |                  |                         |                          |                           |   |
| DDH-MX-S-44  | 845.4            | Dunite (serpentinite)   | 7 (7)                    | Adcumulate                | Ser, Mt, Cr, Chl, Fe*                           |
| DDH-MX-S-51  | 803.0            | Dunite (serpentinite)   | 7 (7)                    | Mesocumulate              | Ser, Mt, Cr, Chl, Cpx, Fe*                      |
| DDH-MX-S-60  | 759.1            | Dunite                  | 6 (5)                    | Adcumulate                | Ser, Mu, Chl, Mt, Tit, Fe*                      |
| DDH-MX-S-69  | 704.3            | Dunite                  | 6 (5)                    | Ad/Meso-cumulate          | Ser, Chl, Mt, Cr, Tit, Fe*                      |
| DDH-MX-S-76  | 662.2            | Dunite                  | 6 (5)                    | Adcumulate                | Ser, Ol, Cr, Mt, Chl, Fe*                       |
| DDH-MX-S-85  | 606.7            | Dunite                  | 5 (5)                    | Mesocumulate              | Ol, Ser, Cr, Mt, Chl, Fe*                       |
| DDH-MX-S-93  | 557.7            | Dunite                  | 5 (5)                    | Adcumulate                | Ol, Cr, Ser, Mt, Chl, Cal                       |
| DDH-MX-S-102   | 502.2            | Dunite                  | 4 (5)                    | Orthocumulate             | Ol, Cpx, Ser, Cr, Mt, Chl, Bt, Fe*              |
| DDH-MX-S-110   | 454.6            | Dunite                  | 4 (5)                    | Mesocumulate              | Ol, Cpx, Ser, Cr, Bt, Mt, Chl, Fe*              |
| DDH-MX-S-121   | 391.2            | Dunite                  | 3 (3)                    | Adcumulate                | Ol, Cpx, Pl, Cr, Mt, Bt, Ser, Chl, Fe*          |
| DDH-MX-S-123   | 387.2            | Olivine clinopyroxenite | 2 (2)                    | Mesocumulate              | Cpx, Ol, Mt, Tit?, Chl, Fe*                     |
| DDH-MX-S-124   | 383.2            | Olivine clinopyroxenite | 2 (2)                    | Mesocumulate              | Cpx, Ol, Mt, Bt, Opx, Ser, Chl, Bt, Fe*         |
| DDH-MX-S-128   | 363.8            | Dunite                  | 2 (1)                    | Adcumulate                | Ol, Cr, Mt, Chl, Bt, Fe*                        |
| DDH-MX-S-133   | 333.3            | Dunite                  | 2 (1)                    | Ad/Meso-cumulate          | Ol, Cpx, Cr, Mt, Chl, Bt, Fe*                   |
| DDH-MX-S-137   | 309.0            | Dunite                  | 2 (1)                    | Adcumulate                | Ol, Cpx, Cr, Mt, Bt, Fe*                        |
| DDH-MX-S-144   | 266.8            | Dunite                  | 2 (1)                    | Adcumulate                | Ol, Cpx, Opx, Cr, Mt, Bt, Ser, Chl, Fe*         |
| DDH-MX-S-151   | 223.6            | Dunite                  | 2 (1)                    | Mesocumulate              | Ol, Cpx, Cr, Mt, Fe*                            |
| DDH-MX-S-154   | 205.3            | Dunite                  | 2 (1)                    | Ad/Meso-cumulate          | Ol, Cpx, Opx, Cr, Mt, Bt, Fe*                   |

(continued)

Table 1: Continued

| Sample <sup>1</sup>                   | DFB <sup>2</sup> | Rock type          | Cyclic unit <sup>3</sup> | Texture <sup>4</sup> | Mineral phases <sup>5</sup>                 |
|---------------------------------------|------------------|--------------------|--------------------------|----------------------|---|
| DDH-MX-S-156                          | 193.1            | Dunite             | 2 (1)                    | Mesocumulate         | Ol, Cpx, Opx, Cr, Mt, Bt, Fe*               |
| DDH-MX-S-160                          | 174.2            | Peridotite         | 2 (MZ)                   | Mesocumulate         | Ol, Cpx, Pl, Cr, Mt, Bt, Chl, Fe*           |
| DDH-MX-S-164                          | 152.0            | Peridotite         | 2 (MZ)                   | Orthocumulate        | Ol, Cpx, Pl, Opx, Cr, Mt, Bt, Chl, Cal      |
| DDH-MX-S-171                          | 110.5            | Peridotite         | 2 (MZ)                   | Orthocumulate        | Ol, Cpx, Pl, Opx, Cr, Mt, Bt, Chl           |
| DDH-MX-S-182                          | 52.6             | Picrite            | 1 (MZ)                   | Orthocumulate        | Cpx, Opx, Ol, Pl, Mt, Cr, Bt, Chl, Ser      |
| DDH-MX-S-192                          | 0.2              | Gabbro             | 1 (MZ)                   | Granophyric          | Cpx, Opx, Qtz, Cal, Bt, Mt, Cpy             |
| DDH-MX-S-195                          | -2.1             | Wopmay paragneiss  | CR                       | Crystalline, banded  | Fd, Qtz, Opx, Mt, Bt, Zr, Fe*               |
| <i>Muskox main chromitite horizon</i> |                  |                    |                          |                      |   |
| HDB-2000-MX-04a                       |                  | Chromitite horizon | 22                       |                      | Cr, Cpx, Opx, Pl, Ser, Cpy (12-15), Po, Pn  |
| HDB-2000-MX-26a                       |                  | Chromitite horizon | 22                       |                      | Cr (10), Opx, Pl, Mt, Cpx, Ser, Cpy, Po, Pn |
| HDB-2000-MX-40a                       |                  | Chromitite horizon | 22                       |                      | Cr (30), Opx, Pl, Cpx, Ser, Bt, Cpy         |
| <i>Muskox Keel feeder dyke</i>        |                  |                    |                          |                      |   |
| MU 033-241-21                         |                  | Gabbro norite      | Keel                     |                      | Ol, Pl, Px, Fe-Ti, Bt, Ser, Cal             |
| MU 033-252-76                         |                  | Gabbro norite      | Keel                     |                      | Ol, Pl, Px, Fe-Ti, Bt, Ser, Cal             |
| HDB-2001-MX5                          |                  | Gabbro norite      | Keel                     |                      | Ol, Pl, Px, Fe-Ti, Bt, Ser, Cal             |

<sup>1</sup>Diamond drill-hole (DDH) samples denoted north (N) and south (S) upper mantle project cores. Chromitite and Keel dyke samples collected at outcrop.

<sup>2</sup>Depth from the base of the intrusion (DFB) in metres; defined as the distance from the intrusive margin.

<sup>3</sup>Cyclic units defined by Findlay & Smith (1965) (see Fig. 2 for additional details). Numbers in parentheses denote the layer numbers identified by Irvine (1975).

<sup>4</sup>Based on definitions of Wager & Brown (1968).

<sup>5</sup>Petrological descriptions based on transmitted light petrographic inspection. Numbers in parentheses represent approximate proportions based on minerals in the thin-sections studied and all mineral phases listed in relative order of abundance: Bt, biotite; C, clay alteration minerals; Cal, calcite; Chl, chlorite; Cpy, chalcopyrite; Cpx, clinopyroxene; Cr, chromite ( $\pm$  opaques and sulphides); Ep, epidote; Fe\*, Iron-hydroxide alteration; Fe-Ti, Iron-titanium oxides ( $\pm$  opaques and sulphides); Ilm, ilmenite; K-Fd, potassium-feldspar; Mt, magnetite ( $\pm$  opaques and sulphides); Mu, muscovite; Ol, olivine; Opx, orthopyroxene; Pl, plagioclase; Po, pyrrhotite; Pn, pentlandite; Px, pyroxene; Qtz, quartz; Ser, serpentinite; Tit, titanite; Zr, zircon.

Os isotope and platinum-group element analyses were performed at the University of Durham. Approximately 2–3 g of homogenized whole-rock powders were sealed in an externally cooled ( $-10^{\circ}\text{C}$ ), single-use, annealed, Pyrex<sup>TM</sup> borosilicate Carius tube (after Shirey & Walker, 1995), with an isotopically enriched multi-element spike (<sup>99</sup>Ru, <sup>106</sup>Pd, <sup>185</sup>Re, <sup>190</sup>Os, <sup>191</sup>Ir, <sup>194</sup>Pt), and 7–8 ml of inverse aqua regia. The charged Carius tubes, normally prepared in batches of 6–8, and including at least one total procedural blank, were kept at 220–230°C in an oven for >72 h. Os was triply extracted from the inverse aqua regia using CCl<sub>4</sub> (Cohen & Waters, 1996) and then back-extracted into HBr, prior to purification via micro-distillation (Birck *et al.*, 1997). Re and the PGE were recovered and purified from the residual solutions using an anion exchange separation technique (Pearson & Woodland, 2000). Through the course of this study, total procedural blanks ( $n=10$ ) had an average <sup>187</sup>Os/<sup>188</sup>Os isotope composition of  $0.22 \pm 0.05$ , with average concentrations of  $2.9 \pm 1.9$  pg [Re],  $8.9 \pm 3.7$  pg [Pd],  $12.8 \pm 10.5$  pg [Pt],  $3.5 \pm 3.5$  pg [Ru],  $1.0 \pm 1.9$  pg [Ir] and  $0.5 \pm 0.2$  pg [Os]. Isotopic compositions of Os were measured by

thermal ionization mass spectrometry (TIMS) using negative ion mode on a Triton<sup>®</sup> instrument. Re, Pd, Pt, Ru and Ir were measured using an ELAN 6000 Quadrupole ICP-MS and a Neptune<sup>®</sup> multi-collector ICP-MS instrument using methods outlined by Pearson & Woodland (2000) and Day *et al.* (2003a). Offline corrections for Os involved an oxide correction using <sup>16</sup>O/<sup>18</sup>O and <sup>17</sup>O/<sup>18</sup>O values from Nier (1950), an iterative fractionation correction using a <sup>192</sup>Os/<sup>188</sup>Os ratio of 3.08271 (see Shirey & Walker, 1998), a <sup>190</sup>Os spike subtraction, and finally an Os blank subtraction. External precision for <sup>187</sup>Os/<sup>188</sup>Os over the course of the study was better than 2.1‰ (2 $\sigma$ ) on the Durham Triton<sup>®</sup> instrument for two separate standards of variable load sizes provided by the University of Maryland (UMCP standard) and Carnegie Institution (DTM standard);  $0.017\text{--}3.5$  ng; UMCP =  $0.11382 \pm 0.00024$ , 2 $\sigma$ ,  $n=273$ ; DTM =  $0.17402 \pm 0.00027$ , 2 $\sigma$ ,  $n=21$ , measured during the analytical campaign. Measured <sup>187</sup>Re/<sup>185</sup>Re ratios for sample solutions were corrected for mass fractionation using either (1) the deviation for the standard average run on the day over the natural <sup>187</sup>Re/<sup>185</sup>Re (quadrupole analysis), or (2) Ir doping and external normalization to

Table 2: Measured HSE and Os isotope compositions for the GP13 peridotite standard

|                            | Os   |                  | Ir   |                  | Ru   |                  | Pt   |                  | Pd   |                  | Re   |                  | <sup>187</sup> Os/ <sup>188</sup> Os |                  |
|----------------------------|------|------------------|------|------------------|------|------------------|------|------------------|------|------------------|------|------------------|--------------------------------------|------------------|
|                            | ppb  | ±2σ <sup>1</sup> | measured                             | ±2σ <sup>1</sup> |
| GP13                       | 3.74 | 0.00             | 3.80 | 0.01             | 8.49 | 0.69             | 6.97 | 0.04             | 4.97 | 0.07             | 0.30 | 0.00             | 0.12643                              | 0.00008          |
| GP13                       | 3.51 | 0.00             | 3.29 | 0.02             | 8.09 | 0.37             | 7.15 | 0.04             | 5.82 | 0.07             | 0.29 | 0.00             | 0.12638                              | 0.00010          |
| GP13                       | 3.50 | 0.02             | 4.12 | 0.05             | 7.25 | 0.88             | 7.90 | 0.01             | 5.52 | 0.07             | 0.27 | 0.00             | 0.12632                              | 0.00008          |
| GP13                       | 3.57 | 0.02             | 3.88 | 0.07             | 8.13 | 0.43             | 8.61 | 0.01             | 6.55 | 0.02             | 0.29 | 0.00             | 0.12625                              | 0.00008          |
| GP13 <sup>2</sup>          | 3.73 | 0.03             | 3.39 | 0.01             | 6.35 | 0.11             | 8.25 | 1.50             | —    | —                | 0.31 | 0.00             | 0.12623                              | 0.00008          |
|                            | Mean | SD               | Mean                                 | SD               |
| Average <sup>3</sup>       | 3.61 | 0.12             | 3.70 | 0.35             | 7.66 | 0.87             | 7.77 | 0.70             | 5.71 | 0.66             | 0.29 | 0.01             | 0.12632                              | 0.00009          |
| %RSD                       | 3.2  |                  | 9.4  |                  | 11.3 |                  | 9.0  |                  | 11.6 |                  | 4.5  |                  |                                      |                  |
| Durham (n=8) <sup>4</sup>  | 3.87 | 0.17             | 3.56 | 0.33             | 6.97 | 0.23             | 7.00 | 0.52             | 5.64 | 0.35             | 0.33 | 0.01             | 0.1262                               | —                |
| Leoben (n=4) <sup>5</sup>  | 4.06 | 0.03             | 3.33 | 0.09             | 6.25 | 0.39             | 6.69 | 0.69             | 5.68 | 0.27             | 0.31 | 0.01             | —                                    | —                |
| DLC (n=9) <sup>4</sup>     | 3.38 | —                | —    | —                | 6.43 | 0.75             | 5.42 | 0.71             | —    | —                | —    | —                | —                                    | —                |
| Chicago (n=1) <sup>4</sup> | 3.60 | —                | 3.35 | —                | 7.23 | —                | 6.15 | —                | 5.75 | —                | —    | —                | —                                    | —                |

<sup>1</sup>Internal analytical precision of measurement.

<sup>2</sup>Measured using the University of Leoben enriched PGE spike.

<sup>3</sup>Average HSE abundance and Os isotope data for GP13E from five separate digestions during the course of this study.

<sup>4</sup>From Pearson *et al.* (2004). Single <sup>187</sup>Os/<sup>188</sup>Os ratio reported for GP13.

<sup>5</sup>From Meisel & Moser (2004). Two reported values for Os abundance and three reported values for Re abundance.

a <sup>193</sup>Ir/<sup>191</sup>Ir ratio derived on a daily basis relative to a reference <sup>187</sup>Re/<sup>185</sup>Re isotope ratio of 1.67392 (Neptune<sup>®</sup> analysis) (Day *et al.*, 2003a). During the period of analysis five separate digestions and analyses of peridotite standard GP13 were analysed and are presented in Table 2. GP13 has been measured multiple times for PGE and Re in different laboratories using isotope dilution and digestion via Carius tube and high-pressure asher methods (Meisel & Moser, 2004; Pearson *et al.*, 2004; Becker *et al.*, 2006). Reproducibility of GP13 data from the present study ranges from 3.2% RSD for Os to 11.6% RSD for Pd. Some of this variability probably results from inhomogeneous PGE distribution within the sample powder. Inhomogeneous HSE distribution through ‘nuggeting’ is a commonly observed phenomenon, even in standard materials typically measured for isotope-dilution HSE analysis, such as GP13 (Becker *et al.*, 2006).

## RESULTS

### Major and trace elements

The layered series of the Muskox intrusion are cumulate rocks and as such the minerals they accumulate dominantly control their major and trace element compositions (Table 3), with the fractional crystallization trends observed in the intrusion representing a form of cryptic layering (see Wager & Brown, 1968). There is a trend of increasing Mg-number and compatible element (e.g. Cr, Ni) contents progressing upwards within the lower 1000 m

of the intrusion and a sharp decrease in MgO and increase in SiO<sub>2</sub> at the juncture of the main chromitite horizon to the roof rocks (Fig. 4). Characteristic inflections are also evident in MgO and SiO<sub>2</sub> from pyroxenite layers (cyclic units 8 and 16) sandwiched between dunite and peridotite units with relatively invariant SiO<sub>2</sub> <50 wt % and MgO >35 wt %. Considering the Mg-rich nature of the dunite units in the intrusion, the olivine is relatively homogeneous and Fe-rich (Fo<sub>84–86</sub>; L. J. Hulbert, unpublished data), similar to those of other large mafic–ultramafic intrusions (e.g. Eales & Cawthorn, 1996). High total alkali (Na<sub>2</sub>O + K<sub>2</sub>O) contents are observed only in the differentiated rocks of the marginal and roof zones and, with P<sub>2</sub>O<sub>5</sub>, are at levels often below detection limits (<0.01 wt %), within the layered series units. This is especially true for the most serpentinized units, which lie in the centre of the intrusion; there is also a good correlation between total water (H<sub>2</sub>O<sup>T</sup>) and degree of serpentinization (~500 to 1500 m depth from base; Table 1 and Fig. 2). Keel dyke samples have restricted ranges in Mg-number and SiO<sub>2</sub>, and Mg/Fe similar to Coppermine CFB picrite lavas (Day *et al.*, in preparation). In contrast, the country rocks of the intrusion have high SiO<sub>2</sub>, MnO and total Fe<sub>2</sub>O<sub>3</sub> contents.

Mafic–ultramafic layers in the Muskox intrusion have low absolute incompatible trace element abundances and, when combined with compatible element variations, reflect the role of olivine and chromite accumulation in the intrusion, as well as replenishment of new batches of magma to form the observed cyclic units. Compatible trace elements

Table 3: Muskox intrusion whole-rock major and trace element data

| Sample:                                     | N-1        | N-3        | N-11       | N-14       | N-18   | N-27   | N-35   | N-46   | N-54   |
|---|------------|------------|------------|------------|--------|--------|--------|--------|--------|
| DFB (m):                                    | 1880-7     | 1878-0     | 1834-7     | 1821-3     | 1800-9 | 1746-3 | 1700-3 | 1633-6 | 1571-4 |
| Lithology:                                  | Hornby Bay | Granophyre | Granophyre | Pic. webs. | Gabbro | Gabbro | Webs.  | Webs.  | Webs.  |
| Cyclic unit:                                | Sst        | 25         | 25         | 25         | 24     | 24     | 23     | 23     | 22     |
| <i>wt % anhydrous corrected</i>             |            |            |            |            |        |        |        |        |        |
| SiO <sub>2</sub>                            | 89.8       | 58.1       | 52.5       | 42.7       | 51.4   | 50.5   | 51.9   | 51.8   | 51.8   |
| TiO <sub>2</sub>                            | 0.06       | 2.40       | 1.56       | 1.66       | 0.84   | 0.73   | 0.86   | 0.54   | 0.68   |
| Al <sub>2</sub> O <sub>3</sub>              | 3.56       | 12.3       | 14.8       | 14.1       | 14.2   | 15.5   | 10.3   | 10.6   | 3.82   |
| Fe <sub>2</sub> O <sub>3</sub> <sup>T</sup> | 3.16       | 13.4       | 10.5       | 17.7       | 8.65   | 7.98   | 9.44   | 8.27   | 15.0   |
| MgO   | 2.94       | 4.01       | 7.62       | 23.0       | 9.35   | 10.0   | 11.7   | 13.7   | 23.9   |
| MnO   | 0.01       | 0.10       | 0.15       | 0.14       | 0.15   | 0.12   | 0.15   | 0.15   | 0.22   |
| CaO   | 0.21       | 4.10       | 8.60       | 0.54       | 12.8   | 12.8   | 13.8   | 13.4   | 4.23   |
| Na <sub>2</sub> O                           | <0.01      | 1.94       | 1.63       | <0.01      | 1.41   | 1.72   | 1.21   | 1.11   | 0.30   |
| K <sub>2</sub> O                            | 0.17       | 3.35       | 2.51       | 0.04       | 1.14   | 0.63   | 0.47   | 0.40   | 0.07   |
| P <sub>2</sub> O <sub>5</sub>               | 0.05       | 0.34       | 0.14       | 0.17       | 0.06   | 0.07   | 0.08   | 0.04   | 0.06   |
| Mg-no.                                      | 64.9       | 37.3       | 59.0       | 72.0       | 68.2   | 71.3   | 71.1   | 76.6   | 75.9   |
| H <sub>2</sub> O <sup>T</sup>               | 1.9        | 2.3        | 2.0        | 11.0       | 1.7    | 2.1    | 1.1    | 1.8    | 1.8    |
| CO <sub>2</sub> <sup>T</sup>                | 0.2        | 0.3        | 0.2        | 0.2        | 0.2    | 0.2    | 0.2    | 0.2    | 0.2    |
| S (ppm)                                     | 1071       | 7070       | 283        | 638        | 321    | 508    | 2989   | 165    | 3257   |
| <i>ppm (ICP-MS)</i>                         |            |            |            |            |        |        |        |        |        |
| Sc  | 0.85       | 29.1       | 25.7       | 35.2       | 38.3   | 25.8   | 39.3   | 36.4   | 24.3   |
| V   | 46.5       | 334        | 284        | 290        | 268    | 182    | 230    | 189    | 166    |
| Cr  | 13.3       | 9.10       | 113        | 840        | 79.3   | 480    | 872    | 822    | 2564   |
| Co  | 37.5       | 32.6       | 40.6       | 66.8       | 43.9   | 41.2   | 59.8   | 49.9   | 120    |
| Ni  | 5.71       | 31.9       | 124        | 226        | 91.2   | 176    | 769    | 342    | 1242   |
| Cu  | 5.44       | 29.9       | 148        | 27.2       | 55.0   | 156    | 1370   | 41.2   | 679    |
| Zn  | 165        | 43.5       | 84.4       | 159        | 56.6   | 48.9   | 58.8   | 52.8   | 91.9   |
| Ga  | 3.98       | 21.6       | 17.2       | 18.3       | 15.5   | 14.7   | 11.8   | 11.2   | 6.15   |
| Rb  | 8.34       | 68.6       | 42.5       | 0.65       | 27.8   | 15.9   | 12.9   | 10.5   | 3.27   |
| Sr  | 39.4       | 359        | 295        | 14.6       | 266    | 227    | 166    | 175    | 51.2   |
| Y   | 6.13       | 51.9       | 19.0       | 21.1       | 14.3   | 10.8   | 13.2   | 8.72   | 8.57   |
| Zr  | 73.2       | 311        | 119        | 109        | 58.7   | 49.5   | 50.7   | 27.0   | 46.5   |
| Nb  | 2.84       | 17.2       | 10.0       | 7.18       | 3.57   | 3.21   | 3.51   | 1.72   | 3.05   |
| Cs  | 0.40       | 0.30       | 0.72       | 0.23       | 0.46   | 0.56   | 0.40   | 0.33   | 0.66   |
| Ba  | 52.3       | 866        | 332        | 8.85       | 170    | 125    | 141    | 87.6   | 47.5   |
| La  | 39.9       | 39.0       | 13.5       | 31.2       | 5.77   | 5.33   | 5.75   | 2.89   | 4.77   |
| Ce  | 52.0       | 81.7       | 29.3       | 59.8       | 13.2   | 11.9   | 13.0   | 6.66   | 11.1   |
| Pr  | 4.88       | 11.3       | 4.04       | 6.98       | 1.91   | 1.70   | 1.87   | 1.01   | 1.59   |
| Nd  | 17.1       | 48.7       | 17.5       | 26.9       | 8.98   | 7.72   | 8.74   | 4.83   | 7.10   |
| Sm  | 2.97       | 11.1       | 3.96       | 4.66       | 2.34   | 1.89   | 2.23   | 1.35   | 1.69   |
| Eu  | 0.50       | 2.87       | 1.38       | 0.93       | 0.80   | 0.66   | 0.77   | 0.52   | 0.41   |
| Gd  | 2.23       | 11.1       | 4.02       | 4.03       | 2.71   | 2.12   | 2.66   | 1.67   | 1.85   |
| Tb  | 0.28       | 1.68       | 0.62       | 0.62       | 0.44   | 0.33   | 0.43   | 0.27   | 0.28   |
| Dy  | 1.27       | 9.64       | 3.45       | 3.61       | 2.54   | 1.93   | 2.45   | 1.58   | 1.58   |
| Ho  | 0.22       | 1.89       | 0.68       | 0.78       | 0.50   | 0.39   | 0.47   | 0.31   | 0.31   |
| Er  | 0.55       | 4.86       | 1.74       | 2.20       | 1.30   | 0.99   | 1.22   | 0.79   | 0.80   |
| Tm  | 0.09       | 0.78       | 0.28       | 0.37       | 0.20   | 0.15   | 0.19   | 0.12   | 0.12   |
| Yb  | 0.54       | 4.45       | 1.61       | 2.46       | 1.18   | 0.93   | 1.10   | 0.72   | 0.77   |
| Lu  | 0.09       | 0.70       | 0.25       | 0.41       | 0.19   | 0.15   | 0.18   | 0.11   | 0.12   |
| Hf  | 2.01       | 8.26       | 3.15       | 2.98       | 1.62   | 1.37   | 1.44   | 0.78   | 1.28   |
| Ta  | 0.23       | 1.22       | 0.65       | 0.49       | 0.31   | 0.24   | 0.28   | 0.17   | 0.25   |
| Pb  | 8.29       | 22.9       | 5.51       | 11.40      | 4.58   | 5.89   | 7.14   | 5.09   | 5.89   |
| Th  | 8.29       | 11.9       | 2.20       | 2.28       | 1.15   | 1.04   | 1.00   | 0.48   | 0.93   |
| U   | 3.82       | 3.11       | 0.58       | 0.69       | 0.31   | 0.27   | 0.26   | 0.12   | 0.24   |

(continued)

Table 3: Continued

| Sample:                                     | N-55   | N-56   | N-59       | N-66       | N-75   | N-85       | N-97       | N-100        | N-101        |
|---|--------|--------|------------|------------|--------|------------|------------|--------------|--------------|
| DFB (m):                                    | 1560.0 | 1555.0 | 1542.7     | 1505.2     | 1458.3 | 1397.3     | 1334.0     | 1311.0       | 1305.0       |
| Lithology:                                  | Webs.  | Webs.  | Peridotite | Peridotite | Dunite | Peridotite | Peridotite | Ol. Cpxenite | Ol. Cpxenite |
| Cyclic unit:                                | 21     | 21     | 21         | 20         | 19     | 18         | 17         | 16           | 16           |
| <i>wt % anhydrous corrected</i>             |        |        |            |            |        |            |            |              |              |
| SiO <sub>2</sub>                            | 51.3   | 53.4   | 44.0       | 42.4       | 40.5   | 42.0       | 41.1       | 51.6         | 51.8         |
| TiO <sub>2</sub>                            | 0.72   | 0.58   | 0.21       | 0.34       | 0.21   | 0.30       | 0.12       | 0.27         | 0.27         |
| Al <sub>2</sub> O <sub>3</sub>              | 4.02   | 4.59   | 4.32       | 2.42       | 1.73   | 3.43       | 1.38       | 1.83         | 1.85         |
| Fe <sub>2</sub> O <sub>3</sub> <sup>T</sup> | 9.54   | 8.78   | 13.2       | 16.4       | 15.5   | 13.6       | 15.3       | 7.33         | 7.19         |
| MgO   | 17.9   | 18.1   | 35.0       | 35.5       | 41.8   | 39.9       | 41.7       | 21.2         | 21.4         |
| MnO   | 0.18   | 0.17   | 0.18       | 0.21       | 0.20   | 0.16       | 0.17       | 0.16         | 0.16         |
| CaO   | 15.9   | 13.7   | 3.09       | 2.66       | 0.02   | 0.56       | 0.13       | 17.3         | 17.4         |
| Na <sub>2</sub> O                           | 0.30   | 0.60   | <0.01      | <0.01      | <0.01  | <0.01      | <0.01      | 0.31         | <0.01        |
| K <sub>2</sub> O                            | 0.03   | 0.12   | 0.02       | 0.07       | <0.01  | 0.03       | <0.01      | 0.01         | <0.01        |
| P <sub>2</sub> O <sub>5</sub>               | 0.04   | 0.04   | 0.02       | 0.03       | 0.01   | 0.03       | 0.02       | 0.01         | 0.01         |
| Mg-no.                                      | 78.8   | 80.3   | 84.0       | 81.2       | 84.3   | 85.3       | 84.4       | 85.1         | 85.5         |
| H <sub>2</sub> O <sup>T</sup>               | 1.6    | 0.6    | 10.5       | 9.1        | 12.3   | 11.4       | 12.4       | 2.5          | 3.2          |
| CO <sub>2</sub> <sup>T</sup>                | 0.2    | 0.1    | 0.2        | 0.1        | 0.3    | 0.1        | 0.2        | 0.1          | 0.2          |
| S (ppm)                                     | 181    | 111    | 378        | 192        | 1441   | 942        | 4258       | 80           | 165          |
| <i>ppm (ICP-MS)</i>                         |        |        |            |            |        |            |            |              |              |
| Sc  | 48.3   | 44.9   | 11.7       | 11.3       | 7.38   | 6.92       | 6.76       | 42.6         | 54.1         |
| V   | 244    | 216    | 75.7       | 87.9       | 64.9   | 61.2       | 44.7       | 187          | 236          |
| Cr  | 2738   | 3024   | 3520       | 3336       | 4449   | 3556       | 1695       | 3100         | 4843         |
| Co  | 61.9   | 57.7   | 124        | 120        | 117    | 125        | 165        | 47.5         | 73.0         |
| Ni  | 438    | 439    | 1358       | 1751       | 1371   | 1863       | 3388       | 238          | 514          |
| Cu  | 38.7   | 19.6   | 46.3       | 44.3       | 328    | 112        | 1134       | 1.65         | 3.69         |
| Zn  | 74.5   | 42.2   | 46.5       | 70.3       | 46.6   | 46.6       | 319        | 20.8         | 25.6         |
| Ga  | 6.62   | 7.05   | 4.29       | 3.45       | 2.60   | 3.39       | 1.35       | 2.35         | 3.21         |
| Rb  | 1.82   | 2.97   | 0.89       | 2.43       | 0.30   | 1.68       | 0.19       | 0.45         | 0.03         |
| Sr  | 28.6   | 81.5   | 10.6       | 27.7       | 0.52   | 2.84       | 1.93       | 10.2         | 12.6         |
| Y   | 11.6   | 10.0   | 2.72       | 4.54       | 1.03   | 3.37       | 1.54       | 4.66         | 6.47         |
| Zr  | 36.1   | 26.8   | 6.41       | 15.8       | 4.54   | 13.6       | 4.39       | 3.40         | 3.64         |
| Nb  | 2.42   | 1.74   | 0.36       | 1.19       | 0.73   | 0.78       | 0.26       | 0.08         | 0.04         |
| Cs  | 0.21   | 0.11   | 0.21       | 0.11       | 0.03   | 0.09       | 0.02       | 0.13         | 0.01         |
| Ba  | 11.0   | 39.5   | 7.90       | 29.3       | 2.17   | 9.22       | 1.56       | 4.49         | 3.53         |
| La  | 3.84   | 2.73   | 0.74       | 2.02       | 0.22   | 1.62       | 0.45       | 0.27         | 0.25         |
| Ce  | 9.06   | 6.60   | 1.76       | 4.59       | 0.56   | 3.48       | 1.02       | 0.95         | 1.05         |
| Pr  | 1.33   | 1.02   | 0.27       | 0.66       | 0.09   | 0.49       | 0.15       | 0.20         | 0.25         |
| Nd  | 6.60   | 5.16   | 1.31       | 3.03       | 0.43   | 2.24       | 0.72       | 1.29         | 1.67         |
| Sm  | 1.84   | 1.53   | 0.38       | 0.76       | 0.12   | 0.55       | 0.20       | 0.51         | 0.74         |
| Eu  | 0.59   | 0.50   | 0.15       | 0.23       | 0.05   | 0.18       | 0.06       | 0.17         | 0.25         |
| Gd  | 2.28   | 1.93   | 0.49       | 0.90       | 0.14   | 0.62       | 0.26       | 0.80         | 1.09         |
| Tb  | 0.36   | 0.31   | 0.08       | 0.14       | 0.02   | 0.10       | 0.04       | 0.14         | 0.19         |
| Dy  | 2.16   | 1.85   | 0.48       | 0.83       | 0.15   | 0.60       | 0.25       | 0.84         | 1.18         |
| Ho  | 0.43   | 0.37   | 0.10       | 0.17       | 0.03   | 0.12       | 0.05       | 0.17         | 0.24         |
| Er  | 1.09   | 0.95   | 0.25       | 0.42       | 0.11   | 0.32       | 0.15       | 0.44         | 0.62         |
| Tm  | 0.17   | 0.15   | 0.04       | 0.07       | 0.02   | 0.05       | 0.02       | 0.07         | 0.09         |
| Yb  | 0.98   | 0.86   | 0.25       | 0.41       | 0.15   | 0.31       | 0.16       | 0.39         | 0.56         |
| Lu  | 0.15   | 0.13   | 0.04       | 0.07       | 0.03   | 0.05       | 0.03       | 0.06         | 0.09         |
| Hf  | 1.05   | 0.80   | 0.20       | 0.47       | 0.13   | 0.37       | 0.14       | 0.15         | 0.20         |
| Ta  | 0.16   | 0.14   | 0.08       | 0.15       | 0.12   | 0.12       | 0.09       | 0.04         | 0.05         |
| Pb  | 2.54   | 2.10   | 2.96       | 1.48       | 4.03   | 4.62       | 1.46       | 0.94         | 0.49         |
| Th  | 0.68   | 0.48   | 0.13       | 0.38       | 0.08   | 0.27       | 0.09       | 0.03         | 0.01         |
| U   | 0.18   | 0.12   | 0.03       | 0.09       | 0.04   | 0.06       | 0.02       | 0.01         | 0.002        |

(continued)

Table 3: Continued

| Sample:                                     | N-104      | N-111  | N-115  | N-122  | N-129  | N-141  | N-151  | N-157    | S-44         |
|---|------------|--------|--------|--------|--------|--------|--------|----------|--------------|
| DFB (m):                                    | 1288-2     | 1232-2 | 1214-5 | 1171-8 | 1061-5 | 990-8  | 936-5  | 893-5    | 845-4        |
| Lithology:                                  | Peridotite | Dunite | Dunite | Dunite | Dunite | Dunite | Dunite | Cpxenite | Dunite (ser) |
| Cyclic unit:                                | 16         | 15     | 14     | 14     | 12     | 11     | 8      | 7        | 7            |
| <i>wt % anhydrous corrected</i>             |            |        |        |        |        |        |        |          |              |
| SiO <sub>2</sub>                            | 42.3       | 42.9   | 41.7   | 41.4   | 38.0   | 40.3   | 42.1   | 50.0     | 40.4         |
| TiO <sub>2</sub>                            | 0.20       | 0.17   | 0.18   | 0.21   | 0.14   | 0.03   | 0.01   | 0.21     | 0.05         |
| Al <sub>2</sub> O <sub>3</sub>              | 1.78       | 1.58   | 1.82   | 1.80   | 3.37   | 0.58   | 9.48   | 1.46     | 0.47         |
| Fe <sub>2</sub> O <sub>3</sub> <sup>T</sup> | 16.5       | 14.7   | 15.1   | 16.6   | 16.8   | 15.8   | 10.7   | 8.03     | 13.7         |
| MgO   | 35.5       | 38.9   | 40.2   | 39.1   | 41.4   | 43.1   | 32.1   | 25.3     | 44.8         |
| MnO   | 0.21       | 0.18   | 0.16   | 0.18   | 0.19   | 0.18   | 0.11   | 0.17     | 0.19         |
| CaO   | 3.47       | 1.54   | 0.75   | 0.52   | 0.01   | 0.02   | 5.45   | 14.8     | 0.30         |
| Na <sub>2</sub> O                           | <0.01      | <0.01  | <0.01  | <0.01  | <0.01  | <0.01  | <0.01  | <0.01    | <0.01        |
| K <sub>2</sub> O                            | <0.01      | 0.01   | 0.02   | 0.09   | 0.04   | <0.01  | 0.03   | <0.01    | <0.01        |
| P <sub>2</sub> O <sub>5</sub>               | 0.02       | 0.02   | 0.02   | 0.03   | 0.01   | 0.01   | 0.01   | 0.00     | 0.01         |
| Mg-no.                                      | 81.0       | 83.9   | 84.0   | 82.3   | 83.0   | 84.4   | 85.6   | 86.2     | 86.6         |
| H <sub>2</sub> O <sup>T</sup>               | 10.0       | 11.3   | 11.4   | 11.3   | 12.1   | 12.6   | 9.3    | 4.7      | 13.6         |
| CO <sub>2</sub> <sup>T</sup>                | 0.1        | 0.1    | 0.1    | 0.2    | 0.2    | 0.3    | 0.1    | 0.1      | 0.6          |
| S (ppm)                                     | 146        | 346    | 540    | 251    | 3572   | 243    | 136    | 77       | 25           |
| <i>ppm (ICP-MS)</i>                         |            |        |        |        |        |        |        |          |              |
| Sc  | 21.0       | 12.6   | 8.32   | 4.59   | 6.57   | 5.88   | 4.31   | 44.9     | 6.21         |
| V   | 152        | 52.5   | 49.6   | 53.2   | 121    | 34.2   | 13.9   | 211      | 28.5         |
| Cr  | 9310       | 2505   | 3470   | 3126   | 17647  | 2375   | 710    | 3425     | 2660         |
| Co  | 161        | 140    | 132    | 101    | 165    | 131    | 129    | 66.1     | 126          |
| Ni  | 2141       | 1111   | 1483   | 1787   | 4360   | 1682   | 1410   | 645      | 1781         |
| Cu  | 15.9       | 75.6   | 107    | 14.3   | 70.2   | 6.78   | 78.3   | 41.0     | 6.25         |
| Zn  | 92.9       | 31.9   | 65.3   | 57.6   | 272    | 50.4   | 51.1   | 33.2     | 43.5         |
| Ga  | 3.67       | 1.65   | 1.77   | 2.51   | 4.34   | 0.87   | 5.38   | 2.01     | 0.91         |
| Rb  | 0.53       | 0.88   | 1.41   | 3.44   | 2.12   | 0.43   | 2.69   | 0.09     | 0.25         |
| Sr  | 4.20       | 3.66   | 2.17   | 2.42   | 0.78   | 0.95   | 118    | 10.4     | 2.09         |
| Y   | 3.33       | 2.54   | 2.31   | 2.65   | 1.00   | 0.31   | 0.23   | 4.76     | 0.60         |
| Zr  | 6.89       | 10.4   | 12.0   | 16.6   | 6.14   | 0.99   | 0.52   | 3.06     | 2.18         |
| Nb  | 0.36       | 0.55   | 0.65   | 0.88   | 0.10   | 0.05   | 0.03   | 0.03     | 0.17         |
| Cs  | 0.02       | 0.04   | 0.08   | 0.16   | 0.07   | 0.02   | 0.77   | 0.02     | 0.03         |
| Ba  | 5.27       | 6.35   | 7.49   | 21.7   | 9.41   | 2.08   | 36.2   | 2.82     | 0.69         |
| La  | 0.70       | 0.98   | 0.87   | 0.93   | 0.05   | 0.07   | 0.13   | 0.28     | 0.26         |
| Ce  | 1.73       | 2.27   | 2.10   | 2.57   | 0.33   | 0.14   | 0.25   | 1.05     | 0.58         |
| Pr  | 0.28       | 0.32   | 0.31   | 0.41   | 0.02   | 0.02   | 0.03   | 0.23     | 0.08         |
| Nd  | 1.44       | 1.55   | 1.45   | 1.93   | 0.33   | 0.07   | 0.12   | 1.37     | 0.34         |
| Sm  | 0.45       | 0.40   | 0.37   | 0.47   | 0.09   | 0.02   | 0.03   | 0.54     | 0.08         |
| Eu  | 0.15       | 0.12   | 0.11   | 0.11   | 0.02   | 0.004  | 0.04   | 0.17     | 0.02         |
| Gd  | 0.58       | 0.47   | 0.43   | 0.51   | 0.13   | 0.02   | 0.04   | 0.81     | 0.09         |
| Tb  | 0.10       | 0.08   | 0.07   | 0.08   | 0.02   | 0.004  | 0.01   | 0.14     | 0.01         |
| Dy  | 0.60       | 0.45   | 0.41   | 0.47   | 0.15   | 0.04   | 0.04   | 0.85     | 0.09         |
| Ho  | 0.12       | 0.09   | 0.08   | 0.10   | 0.03   | 0.01   | 0.01   | 0.18     | 0.02         |
| Er  | 0.33       | 0.24   | 0.22   | 0.26   | 0.10   | 0.03   | 0.02   | 0.45     | 0.06         |
| Tm  | 0.06       | 0.04   | 0.03   | 0.04   | 0.02   | 0.01   | 0.004  | 0.07     | 0.01         |
| Yb  | 0.31       | 0.23   | 0.22   | 0.27   | 0.12   | 0.06   | 0.03   | 0.42     | 0.07         |
| Lu  | 0.05       | 0.04   | 0.03   | 0.05   | 0.02   | 0.01   | 0.005  | 0.06     | 0.01         |
| Hf  | 0.21       | 0.28   | 0.33   | 0.43   | 0.14   | 0.03   | 0.02   | 0.15     | 0.06         |
| Ta  | 0.03       | 0.12   | 0.11   | 0.12   | 0.01   | 0.08   | 0.08   | 0.05     | 0.02         |
| Pb  | 2.83       | 2.86   | 2.23   | 1.83   | 1.93   | 3.00   | 2.38   | 1.25     | 0.68         |
| Th  | 0.09       | 0.16   | 0.21   | 0.39   | 0.06   | 0.03   | 0.02   | 0.01     | 0.07         |
| U   | 0.03       | 0.04   | 0.05   | 0.10   | 0.02   | 0.01   | 0.005  | 0.004    | 0.02         |

(continued)

Table 3: Continued

| Sample:                                     | S-51         | S-60   | S-69   | S-76   | S-85   | S-93   | S-102  | S-110  | S-121  |
|---|--------------|--------|--------|--------|--------|--------|--------|--------|--------|
| DFB (m):                                    | 803.0        | 759.1  | 704.3  | 662.2  | 606.7  | 557.7  | 502.2  | 454.6  | 391.2  |
| Lithology:                                  | Dunite (ser) | Dunite |
| Cyclic unit:                                | 7            | 6      | 6      | 6      | 5      | 5      | 4      | 4      | 3      |
| <i>wt % anhydrous corrected</i>             |              |        |        |        |        |        |        |        |        |
| SiO <sub>2</sub>                            | 41.7         | 39.6   | 40.1   | 40.4   | 40.5   | 40.5   | 40.7   | 40.9   | 40.1   |
| TiO <sub>2</sub>                            | 0.12         | 0.05   | 0.10   | 0.08   | 0.12   | 0.17   | 0.16   | 0.20   | 0.19   |
| Al <sub>2</sub> O <sub>3</sub>              | 0.93         | 0.47   | 1.08   | 0.94   | 1.36   | 1.78   | 1.51   | 1.51   | 1.25   |
| Fe <sub>2</sub> O <sub>3</sub> <sup>T</sup> | 14.2         | 16.3   | 13.1   | 14.9   | 13.6   | 15.0   | 14.1   | 14.3   | 17.7   |
| MgO   | 42.1         | 43.0   | 44.6   | 43.0   | 43.0   | 40.8   | 42.2   | 41.3   | 39.2   |
| MnO   | 0.22         | 0.21   | 0.14   | 0.17   | 0.17   | 0.19   | 0.17   | 0.17   | 0.22   |
| CaO   | 0.66         | 0.29   | 0.69   | 0.54   | 1.30   | 1.47   | 1.06   | 1.54   | 1.29   |
| Na <sub>2</sub> O                           | <0.01        | <0.01  | <0.01  | <0.01  | <0.01  | <0.01  | <0.01  | <0.01  | <0.01  |
| K <sub>2</sub> O                            | 0.01         | 0.04   | 0.08   | 0.01   | 0.02   | 0.05   | 0.04   | 0.03   | 0.05   |
| P <sub>2</sub> O <sub>5</sub>               | 0.02         | 0.01   | 0.01   | 0.01   | 0.02   | 0.02   | 0.02   | 0.03   | 0.03   |
| Mg-no.                                      | 85.5         | 84.0   | 87.1   | 85.1   | 86.3   | 84.4   | 85.6   | 85.1   | 81.4   |
| H <sub>2</sub> O <sup>T</sup>               | 13.5         | 14.6   | 14.4   | 13.6   | 10.6   | 4.9    | 6.9    | 7.1    | 4.9    |
| CO <sub>2</sub> <sup>T</sup>                | 0.3          | 0.5    | 0.4    | 0.4    | 0.2    | 0.1    | 0.1    | 0.1    | 0.2    |
| S (ppm)                                     | 88           | 92     | 130    | 138    | 74     | 66     | 57     | 67     | 77     |
| <i>ppm (ICP-MS)</i>                         |              |        |        |        |        |        |        |        |        |
| Sc  | 11.6         | 3.59   | 3.61   | 6.11   | 4.65   | 6.51   | 6.03   | 9.94   | 6.91   |
| V   | 49.1         | 14.8   | 19.6   | 23.8   | 23.7   | 51.4   | 33.0   | 77.2   | 48.0   |
| Cr  | 2012         | 1258   | 1822   | 1595   | 1926   | 3468   | 2141   | 5079   | 1900   |
| Co  | 119          | 128    | 110    | 125    | 113    | 138    | 133    | 123    | 142    |
| Ni  | 1826         | 1363   | 1960   | 2442   | 2130   | 2746   | 2249   | 2367   | 1630   |
| Cu  | 37.2         | 4.19   | 2.96   | 41.3   | 20.8   | 38.7   | 26.8   | 34.4   | 25.5   |
| Zn  | 58.6         | 43.6   | 33.8   | 51.9   | 48.5   | 69.2   | 61.7   | 74.3   | 74.0   |
| Ga  | 1.05         | 0.49   | 0.73   | 0.66   | 1.03   | 2.05   | 1.84   | 2.85   | 1.82   |
| Rb  | 0.86         | 1.48   | 3.45   | 0.96   | 1.55   | 3.49   | 2.62   | 2.44   | 2.85   |
| Sr  | 3.09         | 2.78   | 3.57   | 2.85   | 27.5   | 48.1   | 23.5   | 24.4   | 32.1   |
| Y   | 2.17         | 0.37   | 1.03   | 1.32   | 1.72   | 2.28   | 2.29   | 2.64   | 2.62   |
| Zr  | 7.24         | 1.85   | 3.72   | 3.79   | 6.41   | 9.94   | 12.5   | 11.5   | 13.4   |
| Nb  | 0.50         | 0.08   | 0.22   | 0.22   | 0.35   | 0.68   | 0.72   | 0.89   | 0.90   |
| Cs  | 0.13         | 0.08   | 0.39   | 0.14   | 0.12   | 0.28   | 0.20   | 0.13   | 0.22   |
| Ba  | 3.41         | 5.08   | 8.92   | 7.48   | 32.3   | 61.2   | 27.5   | 27.3   | 30.1   |
| La  | 0.74         | 0.06   | 0.25   | 0.65   | 0.72   | 1.07   | 1.24   | 1.34   | 1.31   |
| Ce  | 1.81         | 0.15   | 0.78   | 1.70   | 1.69   | 2.35   | 2.79   | 3.03   | 3.13   |
| Pr  | 0.27         | 0.03   | 0.13   | 0.24   | 0.25   | 0.34   | 0.39   | 0.44   | 0.45   |
| Nd  | 1.24         | 0.17   | 0.60   | 1.00   | 1.10   | 1.50   | 1.71   | 1.93   | 2.06   |
| Sm  | 0.33         | 0.04   | 0.15   | 0.23   | 0.27   | 0.38   | 0.42   | 0.48   | 0.50   |
| Eu  | 0.08         | 0.01   | 0.03   | 0.07   | 0.08   | 0.12   | 0.10   | 0.14   | 0.12   |
| Gd  | 0.37         | 0.05   | 0.18   | 0.26   | 0.30   | 0.44   | 0.44   | 0.53   | 0.50   |
| Tb  | 0.06         | 0.01   | 0.03   | 0.04   | 0.05   | 0.07   | 0.07   | 0.08   | 0.08   |
| Dy  | 0.39         | 0.05   | 0.18   | 0.24   | 0.31   | 0.40   | 0.41   | 0.48   | 0.46   |
| Ho  | 0.08         | 0.01   | 0.04   | 0.05   | 0.06   | 0.08   | 0.08   | 0.09   | 0.09   |
| Er  | 0.21         | 0.04   | 0.11   | 0.13   | 0.17   | 0.22   | 0.21   | 0.25   | 0.24   |
| Tm  | 0.03         | 0.01   | 0.02   | 0.02   | 0.03   | 0.03   | 0.03   | 0.04   | 0.04   |
| Yb  | 0.20         | 0.07   | 0.12   | 0.14   | 0.17   | 0.22   | 0.21   | 0.24   | 0.24   |
| Lu  | 0.03         | 0.01   | 0.02   | 0.02   | 0.03   | 0.04   | 0.04   | 0.04   | 0.04   |
| Hf  | 0.19         | 0.05   | 0.10   | 0.11   | 0.17   | 0.27   | 0.31   | 0.31   | 0.36   |
| Ta  | 0.11         | 0.10   | 0.08   | 0.09   | 0.09   | 0.11   | 0.13   | 0.07   | 0.13   |
| Pb  | 2.33         | 2.77   | 3.13   | 3.43   | 3.76   | 5.78   | 2.13   | 1.93   | 1.01   |
| Th  | 0.17         | 0.04   | 0.08   | 0.07   | 0.16   | 0.23   | 0.30   | 0.27   | 0.29   |
| U   | 0.04         | 0.02   | 0.02   | 0.02   | 0.04   | 0.06   | 0.08   | 0.07   | 0.07   |

(continued)

Table 3: Continued

| Sample:                                     | S-123        | S-124        | S-128  | S-133  | S-137  | S-144  | S-151  | S-154  | S-156  |
|---|--------------|--------------|--------|--------|--------|--------|--------|--------|--------|
| DFB (m):                                    | 378.0        | 372.0        | 363.8  | 333.3  | 309.0  | 264.0  | 223.6  | 205.3  | 193.1  |
| Lithology:                                  | Ol. cpxenite | Ol. cpxenite | Dunite |
| Cyclic unit:                                | 2            | 2            | 2      | 2      | 2      | 2      | 2      | 2      | 2      |
| <i>wt % anhydrous corrected</i>             |              |              |        |        |        |        |        |        |        |
| SiO <sub>2</sub>                            | 41.9         | 44.6         | 39.4   | 39.8   | 40.1   | 40.2   | 40.2   | 40.3   | 40.3   |
| TiO <sub>2</sub>                            | 0.20         | 0.25         | 0.15   | 0.24   | 0.23   | 0.22   | 0.30   | 0.33   | 0.36   |
| Al <sub>2</sub> O <sub>3</sub>              | 1.54         | 1.92         | 1.05   | 1.56   | 1.87   | 1.81   | 1.97   | 2.18   | 2.11   |
| Fe <sub>2</sub> O <sub>3</sub> <sup>T</sup> | 15.9         | 13.5         | 18.0   | 17.9   | 17.9   | 16.9   | 18.0   | 18.0   | 18.5   |
| MgO   | 36.1         | 31.5         | 40.1   | 38.8   | 37.8   | 38.8   | 37.5   | 37.0   | 36.6   |
| MnO   | 0.21         | 0.19         | 0.22   | 0.22   | 0.21   | 0.21   | 0.22   | 0.22   | 0.22   |
| CaO   | 4.07         | 7.86         | 1.05   | 1.33   | 1.68   | 1.60   | 1.71   | 1.77   | 1.77   |
| Na <sub>2</sub> O                           | <0.01        | <0.01        | <0.01  | 0.10   | <0.01  | <0.01  | <0.01  | 0.10   | <0.01  |
| K <sub>2</sub> O                            | 0.04         | 0.06         | 0.02   | 0.06   | 0.19   | 0.13   | 0.11   | 0.10   | 0.15   |
| P <sub>2</sub> O <sub>5</sub>               | 0.02         | 0.03         | 0.02   | 0.02   | 0.03   | 0.03   | 0.04   | 0.04   | 0.05   |
| Mg-no.                                      | 81.8         | 82.2         | 81.5   | 81.1   | 80.7   | 82.0   | 80.5   | 80.3   | 79.7   |
| H <sub>2</sub> O <sup>T</sup>               | 3.8          | 1.8          | 5.4    | 4.1    | 4.4    | n.m    | 4.0    | 4.4    | 5.1    |
| CO <sub>2</sub> <sup>T</sup>                | 0.1          | 0.1          | 0.1    | 0.1    | 0.2    | n.m    | 0.2    | 0.1    | 0.1    |
| S (ppm)                                     | 80           | 74           | 25     | 90     | 1106   | 700    | 158    | 147    | 107    |
| <i>ppm (ICP-MS)</i>                         |              |              |        |        |        |        |        |        |        |
| Sc  | 18.4         | 31.0         | 8.73   | 9.35   | 6.98   | 9.27   | 9.50   | 8.13   | 8.24   |
| V   | 112          | 154          | 91.9   | 106    | 60.9   | 77.5   | 103    | 96.3   | 97.6   |
| Cr  | 3679         | 2648         | 5918   | 6364   | 2567   | 4188   | 5034   | 4270   | 3893   |
| Co  | 142          | 112          | 165    | 158    | 152    | 146    | 147    | 143    | 140    |
| Ni  | 1672         | 860          | 2154   | 2131   | 2258   | 1580   | 1273   | 2041   | 1898   |
| Cu  | 20.9         | 27.9         | 35.6   | 34.8   | 56.2   | 2.58   | 99.7   | 75.6   | 46.4   |
| Zn  | 79.4         | 65.8         | 99.5   | 117    | 76.7   | 102    | 99.1   | 87.1   | 90.5   |
| Ga  | 2.85         | 2.74         | 2.84   | 3.40   | 2.29   | 2.80   | 3.55   | 3.40   | 3.52   |
| Rb  | 2.69         | 3.36         | 2.43   | 3.04   | 6.54   | 5.79   | 4.65   | 3.52   | 5.33   |
| Sr  | 31.2         | 49.1         | 34.7   | 28.8   | 26.1   | 29.3   | 39.1   | 34.3   | 33.3   |
| Y   | 2.93         | 4.80         | 1.96   | 2.50   | 3.03   | 2.79   | 3.85   | 4.08   | 4.65   |
| Zr  | 8.70         | 10.4         | 9.32   | 11.9   | 13.2   | 14.5   | 20.4   | 19.0   | 26.1   |
| Nb  | 0.61         | 0.62         | 0.66   | 0.83   | 0.89   | 0.93   | 1.39   | 1.42   | 2.02   |
| Cs  | 0.25         | 0.29         | 0.19   | 0.21   | 0.41   | 0.50   | 0.24   | 0.12   | 0.18   |
| Ba  | 29.3         | 54.3         | 42.0   | 30.9   | 36.5   | 31.1   | 46.4   | 35.0   | 42.6   |
| La  | 0.85         | 1.05         | 0.99   | 1.22   | 1.24   | 1.01   | 2.19   | 2.23   | 2.73   |
| Ce  | 2.16         | 2.60         | 2.36   | 2.97   | 3.03   | 2.56   | 4.94   | 5.13   | 6.28   |
| Pr  | 0.30         | 0.42         | 0.30   | 0.39   | 0.46   | 0.38   | 0.70   | 0.74   | 0.89   |
| Nd  | 1.62         | 2.17         | 1.53   | 1.93   | 2.12   | 1.87   | 3.08   | 3.27   | 4.00   |
| Sm  | 0.46         | 0.67         | 0.37   | 0.46   | 0.54   | 0.49   | 0.72   | 0.77   | 0.92   |
| Eu  | 0.14         | 0.22         | 0.11   | 0.14   | 0.14   | 0.12   | 0.21   | 0.22   | 0.23   |
| Gd  | 0.52         | 0.85         | 0.38   | 0.48   | 0.59   | 0.53   | 0.75   | 0.81   | 1.01   |
| Tb  | 0.09         | 0.14         | 0.06   | 0.08   | 0.10   | 0.09   | 0.12   | 0.13   | 0.15   |
| Dy  | 0.53         | 0.84         | 0.36   | 0.46   | 0.55   | 0.50   | 0.69   | 0.74   | 0.86   |
| Ho  | 0.10         | 0.17         | 0.07   | 0.09   | 0.11   | 0.10   | 0.14   | 0.15   | 0.16   |
| Er  | 0.28         | 0.44         | 0.19   | 0.24   | 0.28   | 0.26   | 0.35   | 0.38   | 0.43   |
| Tm  | 0.04         | 0.07         | 0.03   | 0.04   | 0.04   | 0.04   | 0.05   | 0.06   | 0.06   |
| Yb  | 0.28         | 0.41         | 0.18   | 0.23   | 0.27   | 0.25   | 0.33   | 0.37   | 0.41   |
| Lu  | 0.05         | 0.07         | 0.03   | 0.04   | 0.04   | 0.04   | 0.06   | 0.06   | 0.07   |
| Hf  | 0.26         | 0.33         | 0.25   | 0.31   | 0.36   | 0.37   | 0.53   | 0.51   | 0.70   |
| Ta  | 0.04         | 0.15         | 0.05   | 0.06   | 0.13   | 0.13   | 0.15   | 0.16   | 0.21   |
| Pb  | 1.88         | 2.71         | 2.09   | 2.26   | 1.36   | 0.71   | 4.14   | 1.32   | 1.02   |
| Th  | 0.17         | 0.17         | 0.21   | 0.26   | 0.28   | 0.31   | 0.42   | 0.39   | 0.53   |
| U   | 0.04         | 0.04         | 0.06   | 0.07   | 0.07   | 0.09   | 0.10   | 0.09   | 0.13   |

(continued)

Table 3: Continued

| Sample:                                     | S-160      | S-164      | S-171      | S-182   | S-192    | S-195                |
|---|------------|------------|------------|---------|----------|----------------------|
| DFB (m):                                    | 174.2      | 152.0      | 110.5      | 52.6    | 0.2      | -2.1                 |
| Lithology:                                  | Peridotite | Peridotite | Peridotite | Picrite | Gabbro   | Wopmay<br>paragneiss |
| Cyclic unit:                                | 2          | 2          | 2          | 1       | 1        |                      |
| <i>wt % anhydrous corrected</i>             |            |            |            |         |          |                      |
| SiO <sub>2</sub>                            | 40.4       | 41.0       | 43.1       | 44.2    | 49.5     | 47.1                 |
| TiO <sub>2</sub>                            | 0.36       | 0.48       | 0.63       | 0.64    | 0.71     | 0.35                 |
| Al <sub>2</sub> O <sub>3</sub>              | 2.24       | 3.08       | 5.15       | 6.73    | 8.52     | 9.69                 |
| Fe <sub>2</sub> O <sub>3</sub> <sup>T</sup> | 18.7       | 18.0       | 16.9       | 14.8    | 20.9     | 30.0                 |
| MgO   | 35.9       | 34.4       | 28.7       | 27.3    | 12.1     | 6.79                 |
| MnO   | 0.21       | 0.21       | 0.20       | 0.18    | 0.24     | 2.84                 |
| CaO   | 1.87       | 2.50       | 4.56       | 5.17    | 5.45     | 1.16                 |
| Na <sub>2</sub> O                           | <0.01      | 0.11       | 0.41       | 0.52    | 1.16     | 0.60                 |
| K <sub>2</sub> O                            | 0.15       | 0.19       | 0.27       | 0.29    | 1.33     | 1.45                 |
| P <sub>2</sub> O <sub>5</sub>               | 0.04       | 0.05       | 0.07       | 0.07    | 0.07     | 0.08                 |
| Mg-no.                                      | 79.2       | 79.1       | 77.1       | 78.5    | 53.4     | 31.0                 |
| H <sub>2</sub> O <sup>T</sup>               | 6.0        | 5.9        | 4.3        | 4.7     | negative | 1.9                  |
| CO <sub>2</sub> <sup>T</sup>                | 0.1        | 0.1        | 0.1        | 0.1     | 0.2      | 1.3                  |
| S (ppm)                                     | 1946       | 158        | 199        | 216     | 46 800   | 5769                 |
| <i>ppm (ICP-MS)</i>                         |            |            |            |         |          |                      |
| Sc  | 10.5       | 13.0       | 17.5       | 19.4    | 37.8     | 17.0                 |
| V   | 115        | 133        | 179        | 166     | 466      | 136                  |
| Cr  | 4519       | 4513       | 4010       | 3373    | 685      | 144                  |
| Co  | 157        | 143        | 130        | 111     | 476      | 64.1                 |
| Ni  | 1520       | 566        | 1543       | 404     | 1779     | 136                  |
| Cu  | 880        | 62.2       | 120        | 83.3    | 1287     | 883                  |
| Zn  | 97.8       | 102        | 119        | 85.5    | 78.7     | 148                  |
| Ga  | 4.34       | 5.09       | 7.59       | 8.07    | 12.1     | 16.1                 |
| Rb  | 6.13       | 6.81       | 9.09       | 10.7    | 40.9     | 74.8                 |
| Sr  | 38.8       | 68.9       | 89.3       | 87.3    | 145      | 167                  |
| Y   | 4.58       | 6.23       | 7.21       | 9.05    | 20.1     | 15.5                 |
| Zr  | 23.8       | 34.4       | 38.4       | 45.9    | 77.0     | 52.1                 |
| Nb  | 1.88       | 2.43       | 3.33       | 3.60    | 6.69     | 5.40                 |
| Cs  | 0.35       | 0.30       | 0.25       | 1.22    | 1.06     | 7.76                 |
| Ba  | 50.7       | 67.0       | 79.9       | 78.5    | 210      | 589                  |
| La  | 2.62       | 3.81       | 4.09       | 4.93    | 8.04     | 12.3                 |
| Ce  | 6.05       | 8.58       | 9.24       | 10.8    | 23.4     | 25.1                 |
| Pr  | 0.84       | 1.20       | 1.24       | 1.48    | 3.77     | 2.91                 |
| Nd  | 3.81       | 5.30       | 5.75       | 6.54    | 17.6     | 17.1                 |
| Sm  | 0.90       | 1.22       | 1.33       | 1.56    | 3.91     | 2.20                 |
| Eu  | 0.24       | 0.33       | 0.44       | 0.47    | 0.65     | 0.73                 |
| Gd  | 0.91       | 1.29       | 1.45       | 1.66    | 3.59     | 2.19                 |
| Tb  | 0.14       | 0.20       | 0.23       | 0.28    | 0.57     | 0.37                 |
| Dy  | 0.81       | 1.12       | 1.31       | 1.57    | 3.33     | 2.38                 |
| Ho  | 0.16       | 0.22       | 0.26       | 0.32    | 0.70     | 0.52                 |
| Er  | 0.42       | 0.57       | 0.68       | 0.87    | 1.98     | 1.54                 |
| Tm  | 0.07       | 0.08       | 0.11       | 0.13    | 0.32     | 0.28                 |
| Yb  | 0.40       | 0.53       | 0.65       | 0.83    | 2.09     | 1.78                 |
| Lu  | 0.06       | 0.09       | 0.11       | 0.13    | 0.35     | 0.31                 |
| Hf  | 0.64       | 0.90       | 1.02       | 1.21    | 2.21     | 1.56                 |
| Ta  | 0.15       | 0.22       | 0.22       | 0.28    | 0.51     | 0.43                 |
| Pb  | 2.21       | 2.89       | 1.90       | 2.39    | 12.7     | 23.7                 |
| Th  | 0.55       | 0.68       | 0.79       | 1.06    | 7.68     | 5.56                 |
| U   | 0.14       | 0.18       | 0.21       | 0.27    | 1.75     | 1.47                 |

(continued)

Table 3: Continued

| Sample:                                     | MX-04a     | MX-26a     | MX-40a     | MU 033.241.21 | MU 033.252.76 | HDB-2001-MX5  |
|---|------------|------------|------------|---------------|---------------|---------------|
| DFB (m):                                    |            |            |            |               |               |               |
| Lithology:                                  | Chromitite | Chromitite | Chromitite | Gabbro norite | Gabbro norite | Gabbro norite |
| Cyclic unit:                                | 22         | 22         | 22         | Keel          | Keel          | Keel          |
| <i>wt % anhydrous corrected</i>             |            |            |            |               |               |               |
| SiO <sub>2</sub>                            | 27.4       | 33.8       | 22.4       | 45.6          | 45.9          | 46.5          |
| TiO <sub>2</sub>                            | 2.82       | 1.95       | 3.14       | 0.52          | 0.50          | 0.58          |
| Al <sub>2</sub> O <sub>3</sub>              | 10.1       | 10.5       | 15.2       | 8.44          | 8.86          | 8.17          |
| Fe <sub>2</sub> O <sub>3</sub> <sup>T</sup> | 35.6       | 29.4       | 32.9       | 12.7          | 12.3          | 12.5          |
| MgO   | 15.1       | 18.4       | 17.7       | 23.7          | 22.9          | 22.4          |
| MnO   | 0.27       | 0.26       | 0.28       | 0.18          | 0.18          | 0.18          |
| CaO   | 8.20       | 5.06       | 8.20       | 7.96          | 8.50          | 8.43          |
| Na <sub>2</sub> O                           | 0.32       | 0.45       | 0.10       | 0.64          | 0.64          | 0.81          |
| K <sub>2</sub> O                            | 0.13       | 0.16       | 0.08       | 0.21          | 0.21          | 0.31          |
| P <sub>2</sub> O <sub>5</sub>               | <0.01      | <0.01      | <0.01      | 0.04          | 0.04          | 0.05          |
| Mg-no.                                      | 45.6       | 55.3       | 51.6       | 78.7          | 78.7          | 78.1          |
| H <sub>2</sub> O <sup>T</sup>               | -0.8       | -0.4       | 1.5        | 3.9           | 3.7           | 2.0           |
| CO <sub>2</sub> <sup>T</sup>                | n.m.       | n.m.       | n.m.       | n.m.          | n.m.          | n.m.          |
| S (ppm)                                     | n.m.       | n.m.       | n.m.       | n.m.          | n.m.          | n.m.          |
| <i>ppm (ICP-MS)</i>                         |            |            |            |               |               |               |
| Sc  | 23.9       | 20.3       | 16.7       | 27.0          | 25.9          | 32.4          |
| V   | 1141       | 525        | 1211       | 175           | 161           | 197           |
| Cr  | 87365      | 37517      | 109303     | 2966          | 2745          | 2416          |
| Co  | 132        | 106        | 149        | 96.2          | 89.9          | 97.9          |
| Ni  | 1712       | 1564       | 895        | 327           | 303           | 268           |
| Cu  | 5949       | 2348       | 312        | 85.1          | 67.9          | 146.5         |
| Zn  | 256        | 128        | 283        | 77.0          | 76.5          | 86.2          |
| Ga  | 26.8       | 14.7       | 41.5       | 8.62          | 8.57          | 9.01          |
| Rb  | 2.46       | 2.71       | 1.48       | 7.02          | 6.00          | 9.66          |
| Sr  | 31.1       | 54.1       | 40.3       | 108           | 114           | 107           |
| Y   | 5.87       | 5.44       | 4.34       | 8.67          | 7.81          | 11.7          |
| Zr  | 17.1       | 18.6       | 14.4       | 32.4          | 26.9          | 42.6          |
| Nb  | 1.23       | 1.14       | 1.07       | 2.01          | 1.72          | 2.43          |
| Cs  | 0.12       | 0.18       | 0.09       | 0.35          | 0.30          | 0.54          |
| Ba  | 39.2       | 53.7       | 25.7       | 60.2          | 69.1          | 84.4          |
| La  | 1.75       | 2.02       | 1.47       | 3.53          | 3.08          | 4.55          |
| Ce  | 4.32       | 4.74       | 3.36       | 8.00          | 7.00          | 10.0          |
| Pr  | 0.66       | 0.68       | 0.50       | 1.13          | 1.00          | 1.40          |
| Nd  | 3.38       | 3.23       | 2.45       | 5.16          | 4.63          | 6.29          |
| Sm  | 0.96       | 0.87       | 0.68       | 1.31          | 1.17          | 1.64          |
| Eu  | 0.31       | 0.31       | 0.31       | 0.45          | 0.43          | 0.52          |
| Gd  | 1.20       | 1.03       | 0.83       | 1.54          | 1.38          | 1.88          |
| Tb  | 0.19       | 0.16       | 0.13       | 0.24          | 0.23          | 0.32          |
| Dy  | 1.12       | 0.97       | 0.80       | 1.46          | 1.35          | 1.94          |
| Ho  | 0.21       | 0.19       | 0.16       | 0.30          | 0.28          | 0.40          |
| Er  | 0.56       | 0.52       | 0.41       | 0.81          | 0.74          | 1.11          |
| Tm  | 0.08       | 0.08       | 0.06       | 0.12          | 0.11          | 0.17          |
| Yb  | 0.50       | 0.49       | 0.38       | 0.79          | 0.72          | 1.05          |
| Lu  | 0.07       | 0.08       | 0.06       | 0.12          | 0.12          | 0.17          |
| Hf  | 0.53       | 0.51       | 0.46       | 0.86          | 0.74          | 1.14          |
| Ta  | 0.08       | 0.08       | 0.08       | 0.17          | 0.15          | 0.21          |
| Pb  | 4.34       | 4.23       | 2.65       | 1.97          | 6.60          | 8.08          |
| Th  | 0.29       | 0.34       | 0.18       | 0.67          | 0.55          | 1.02          |
| U   | 0.07       | 0.08       | 0.05       | 0.17          | 0.14          | 0.26          |

Webs., websterite; n.m., not measured.

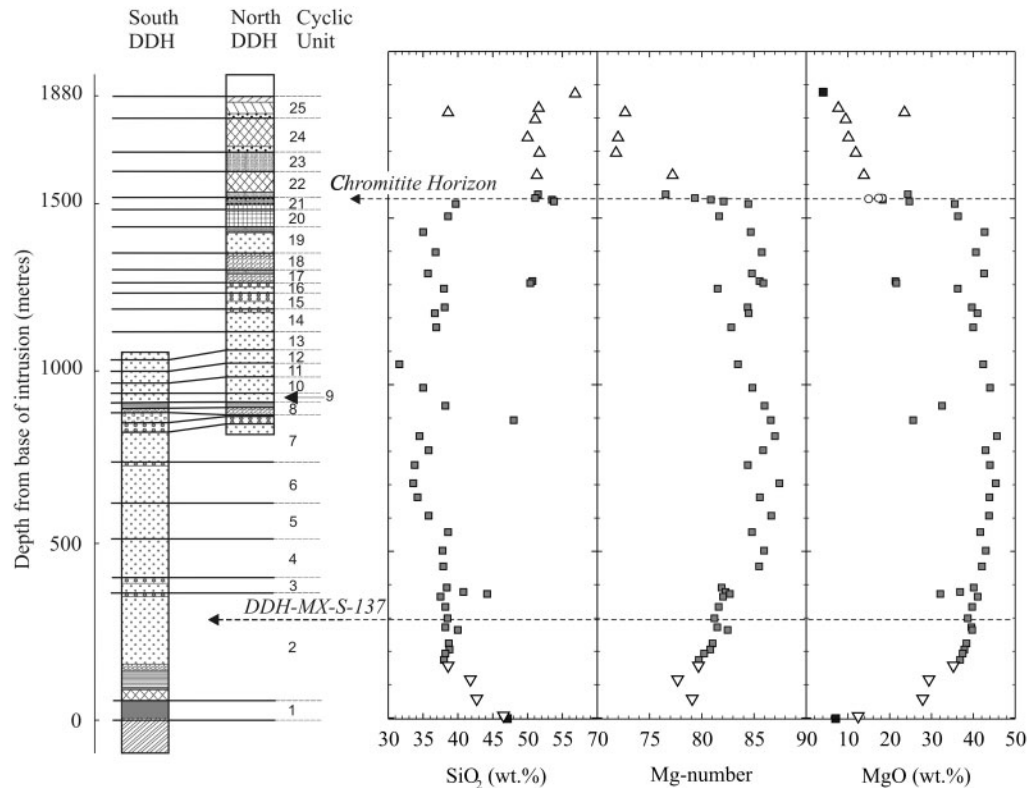


**Fig. 4.** Variation of major elements (corrected to anhydrous proportions) with depth from base in the Muskox intrusion. The intrusion is dominantly composed of dunites and peridotites, with a 300 m roof zone (also known as the upper border zone) predominantly composed of silica-rich granophyres. The main chromitite horizon occurs at the juncture between the layered series and the high-silica granophyres of the roof zone. Mg-number: magnesian number [ $\text{Mg}/(\text{Mg} + \text{Fe}^{2+})$ ]. {■}, Country rocks; {△}, roof zone; grey squares, layered series; {▽}, marginal zone.

correlate with Mg-number such that variations with stratigraphic height of Cr and Ni are similar to refractory major element variations. Rare earth element (REE) profiles vary greatly in the intrusion, and correspond to lower concentrations in ultramafic compositions and cyclic units relative to roof rock and marginal zone rocks (Fig. 5). The majority of samples have enrichments in light REE (LREE, e.g. La) relative to the middle REE (MREE, e.g. Sm) and heavy REE (HREE, e.g. Yb) such that  $(\text{La}/\text{Sm})_n$  and  $(\text{La}/\text{Yb})_n$  ratios are supra-chondritic. This results in REE patterns with negative slopes from the LREE to HREE, apart from for pyroxenites (N-100; -101; -157, S-123; -124), which have characteristic LREE-depleted patterns. Keel dyke samples and the main chromitite horizon have negative REE profiles. The REE profiles of the Wopmay paragneiss and Hornby Bay sandstone are highly distinctive and differ from those of most of the Muskox intrusion rocks, especially the REE profiles of the layered series rocks. Effects of plagioclase fractionation are apparent in the REE profiles of the layered series rocks. There are variations in Eu anomalies, from negligible in Muskox Keel dyke samples ( $\text{Eu}/\text{Eu}^* = 0.92\text{--}1.06$ ) to large positive and negative anomalies in cyclic units 7–21

( $\text{Eu}/\text{Eu}^* = 0.67\text{--}3.09$ ). A troctolite (N-151) has the most positive Eu anomaly of all the layered series rocks and the main chromitite layer also has minor Eu anomalies.

Primitive-mantle normalized multi element plots of Muskox Keel, marginal zone, roof zone and layered series rocks reveal similar profiles for cyclic unit 2 dunites and the Muskox Keel feeder dyke (Fig. 6). There are large variations for large ion lithophile elements (LILE; Rb, Ba, Sr) and Ta, generally negative anomalies for Ti and Nb, and positive anomalies for Pb and Th. Elevated Pb, Rb, Ba, Sr and Th, and negative Nb, Ta and Ti anomalies are characteristic of the Wopmay orogen gneiss and these same features are also prominent in the Keel dyke and cyclic layer 2. Thorium excess in the Hornby Bay sandstone roof rock (N-1) is also observed in N-3 and N-14 but not in other roof rocks. Samples with notable trace element compositions include the main chromitite layer, which exhibits positive Ti anomalies, from Ti-rich chromite, and distinct Nb, Ta and Pb anomalies. The relatively elevated Ti content of the chromitites is consistent with greater  $\text{Fe}^{3+}$ , Ti and  $\text{Fe}^{2+}/(\text{Fe}^{2+} + \text{Mg})$  in the Muskox intrusion chromitites than chromitite reefs in other large mafic–ultramafic layered intrusions, possibly relating to chromitite

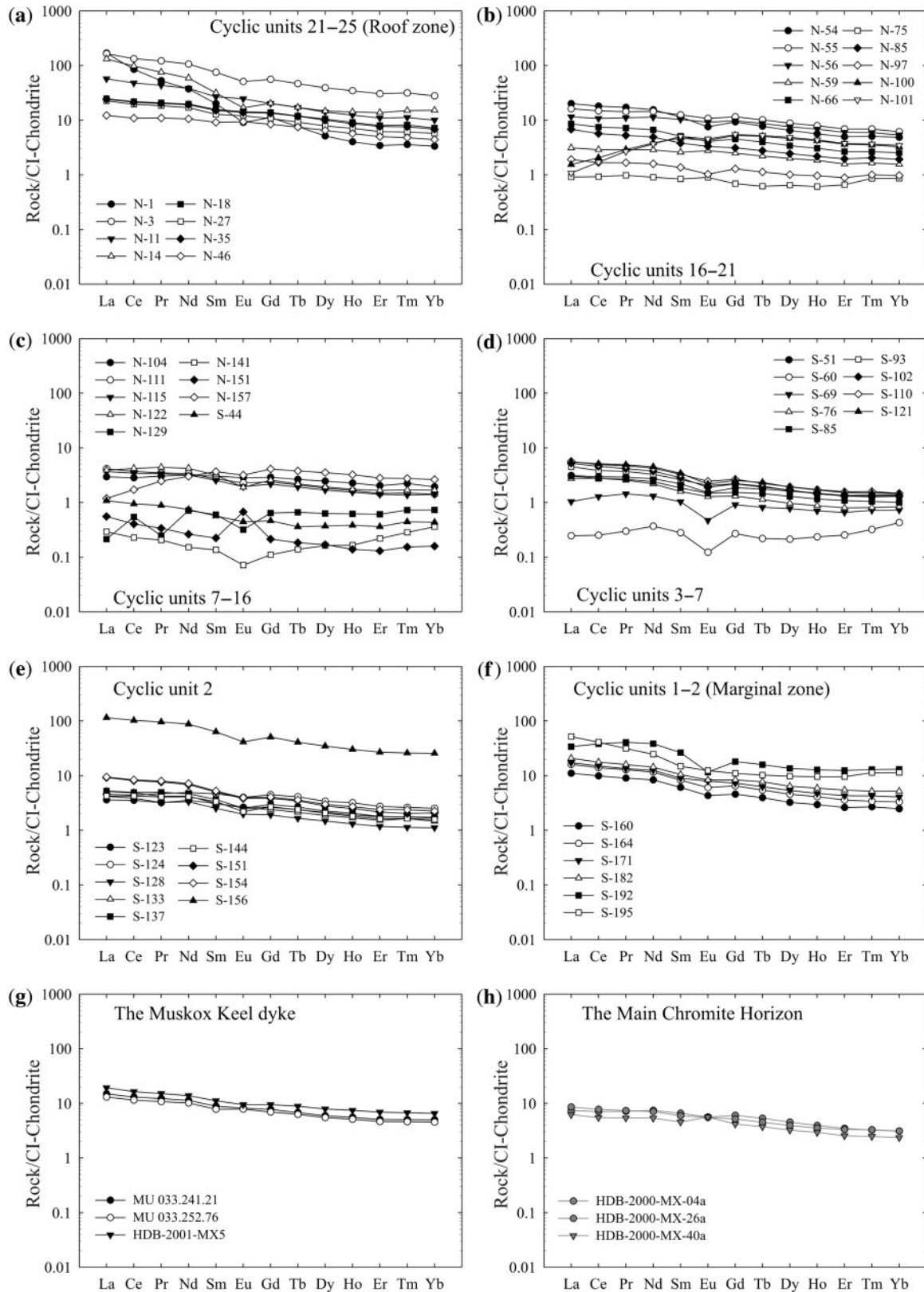


**Fig. 5.** Rare-earth element (REE) profiles for the Muskox intrusion, including (a) the roof zone; (b) cyclic units 16–21; (c) cyclic units 7–16; (d) cyclic units 3–7; (e) cyclic unit 2; (f) cyclic units 1 and 2; (g) the Muskox Keel dyke; (h) the main chromitite horizon. Most samples have LREE-enriched REE profiles with the notable exception of the pyroxenites (N-100, N-101, N-157, S-123, S-124), which have LREE-depleted patterns. Cyclic units 4–8 have the lowest REE abundances in the intrusion (c and d)—these are some of the most ultramafic units in the intrusion. Chondrite normalization values are from McDonough & Sun (1995).

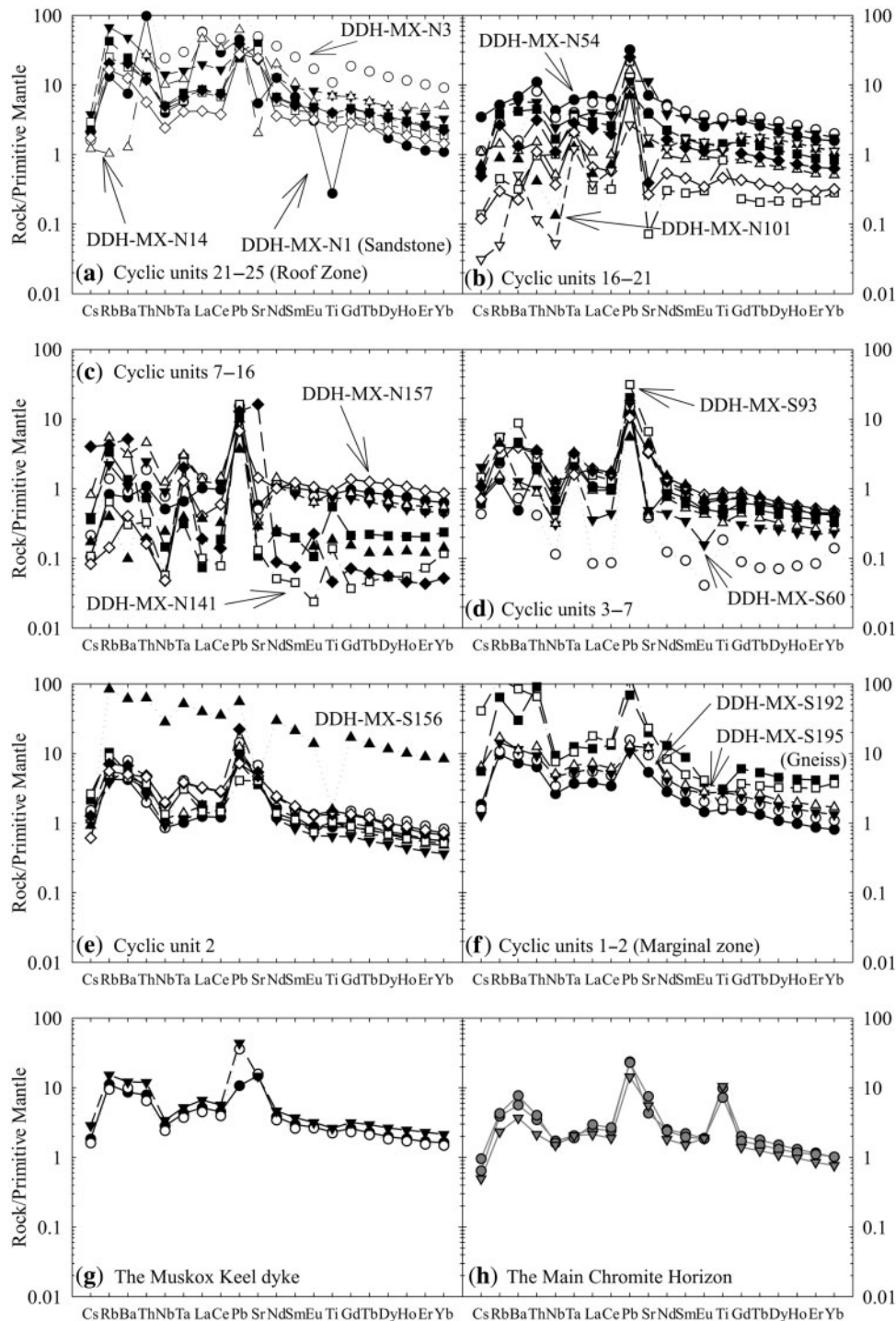


**Fig. 6.** Primitive mantle normalized multi-element variation diagrams for the Muskox intrusion including (a) the roof zone; (b) cyclic units 16–21; (c) cyclic units 7–16; (d) cyclic units 3–7; (e) cyclic unit 2; (f) cyclic units 1 and 2; (g) the Muskox Keel dyke; (h) the main chromitite horizon. Positive Pb anomalies occur in all Muskox intrusion and Keel dyke samples. Marginal and roof zone rocks exhibit higher concentrations and more diverse trace element patterns than layered series rocks, with large variations in fluid-mobile elements (e.g. Rb, Sr, Ba). Fluid-mobile element ratios and abundances also vary between serpentinized (e.g. S-51) and fresher (e.g. S-133) layered series rocks. Keel dyke and chromitite horizon samples have different absolute abundances but similar multi-element patterns, with the notable exception of Ti. Marginal and roof zone samples share multi-element pattern characteristics with country rock samples. Symbols are as for Fig. 5. Primitive mantle normalization values are from Sun & McDonough (1989).

Table 4: *O* isotope results for the Muskox intrusion

| Sample                  | Rock type               | $\delta^{18}\text{O}$ |
|-------------------------|-------------------------|-----------------------|
| <i>Cyclic units</i>     |                         |                       |
| N-56 OI                 | Websterite              | 6.88                  |
| N-100 Cpx               | Olivine clinopyroxenite | 6.19                  |
| S-123 OI                | Olivine clinopyroxenite | 5.54                  |
| S-137 OI                | Dunite                  | 5.65                  |
| <i>Chromite horizon</i> |                         |                       |
| MX04A Chr               | Chromitite              | 4.83                  |
| MX26A OI                | Chromitite              | 7.14                  |
| MX26A Chr               | Chromitite              | 4.25                  |
| <i>Keel dyke</i>        |                         |                       |
| MU-033.241.21 OI        | Gabbro norite           | 6.27                  |
| MU-033.252.76 OI        | Gabbro norite           | 6.05                  |
| HDB-2001-MX5 OI         | Gabbro norite           | 6.10                  |

OI, olivine; Cpx, clinopyroxene; Chr, chromite.  $\delta^{18}\text{O}_n$  is the per mille (‰) deviation of  $^{18}\text{O}/^{16}\text{O}$  in  $n$  from the international standard (std) V-SMOW, given by the relationship  $\delta^{18}\text{O}_n = 1000 \times [(^{18}\text{O}/^{16}\text{O}_n)/(^{18}\text{O}/^{16}\text{O}_{\text{std}} - 1)]$ .

formation relatively higher in the stratigraphic section in the Muskox intrusion. Pb abundances vary at the base of the marginal zone and top of the roof zone, and appear to follow cryptic layering trends in the cyclic units, similar to those seen in the major element profiles. Ce/Pb ratios for the serpentinized layered series rocks fall to abnormally low ratios of  $\sim 0.08$  and to  $\sim 1$ – $8$  for the cyclic unit 2 dunites [for comparison, depleted mid-ocean ridge basalt mantle (DMM) Ce/Pb is  $\sim 30$ , bulk crust Ce/Pb is  $\sim 3$ – $3$ ].

### Oxygen isotopes

In the classic work by Taylor (1968) on the oxygen isotope geochemistry of igneous rocks, he noted that the Muskox intrusion is markedly  $\delta^{18}\text{O}$ -rich relative to typical mafic-ultramafic intrusions. Our  $\delta^{18}\text{O}$  values for olivine in four cyclic units, including one pyroxenite ( $\delta^{18}\text{O}_{\text{Cpx}} = 6.19\%$ ,  $\delta^{18}\text{O}_{\text{OI}} = 5.9$  assuming  $\Delta^{18}\text{O}_{\text{OI-Cpx}} = -0.3$ ), range from  $+5.54$  to  $+6.88\%$  (Table 4), and are consistent with Taylor's observations. Keel dyke  $\delta^{18}\text{O}_{\text{OI}}$  values cover a restricted range ( $+6.10$  to  $+6.27\%$ ). Lowest  $\delta^{18}\text{O}_{\text{OI}}$  measured values ( $+5.5\%$ ) lie within the range of values typically observed in mid-oceanic ridge basalts (Eiler *et al.*, 2000a), ocean islands (Eiler *et al.*, 1996, 1997), arc volcanic rocks (Eiler *et al.*, 2000b) and mantle peridotites (Mattey *et al.*, 1994). Two chromites and one olivine from the chromite reef were also analysed yielding a silicate-oxide fractionation factor ( $\Delta^{18}\text{O}_{\text{OI-Cr}}$ ) equal to  $-2.9$  and  $\delta^{18}\text{O}_{\text{OI}} = +7.14$  to  $+7.7\%$ . The  $\Delta^{18}\text{O}_{\text{OI-Cr}}$  is consistent with the value of  $-3.0 \pm 0.9$  ( $n = 10$ , 1 SD) obtained on

chromites and olivines from an Archaean ultramafic body (Lowry *et al.*, 2003). Calculated whole-rock  $\delta^{18}\text{O}$  values correspond to  $+5.9$  to  $+8.1\%$ , in the range of published bomb-fluorination data for Muskox cyclic units ( $+6.3$  to  $+7.3\%$ ; Taylor, 1968).

### Sm–Nd isotope systematics

#### *Intrusive magmatic rocks*

Sm and Nd concentrations (Table 5) range from 0.04 to 11.1 ppm and 0.17 to 48.7 ppm, respectively, with a range in  $^{147}\text{Sm}/^{144}\text{Nd}$  of 0.109–0.197.  $^{147}\text{Sm}/^{144}\text{Nd}$  increases steadily from the base to the roof zone, where ratios again decrease (Fig. 7). Calculated initial Nd isotope ( $\epsilon_{\text{Nd}i}$ ) values (age corrected to 1270 Ma) are in agreement with previous whole-rock analyses of the layered series rocks (Fig. 7) (Stewart & DePaolo, 1996). The entire range in  $\epsilon_{\text{Nd}i}$  values can be found in the marginal and roof zone samples. A single  $\epsilon_{\text{Nd}i}$  value ( $-1.5$ ) obtained for a Keel sample, which was collected from the centre of the feeder dyke, is also similar to the value of a Keel sample ( $-1.6$ ) reported previously (Stewart & DePaolo, 1996). The least negative  $\epsilon_{\text{Nd}i}$  values of layered series rocks in the Muskox intrusion are similar to the isochron initial  $\epsilon_{\text{Nd}}$  compositions obtained from an olivine clinopyroxenite ( $-0.2 \pm 0.3$ ) and a gabbro ( $-0.6 \pm 0.1$ ) in the upper portions of the layered series (Stewart & DePaolo, 1996). Whole-rock Sm–Nd isotope data from this study show some scatter on a  $^{147}\text{Sm}/^{144}\text{Nd}$ – $^{143}\text{Nd}/^{144}\text{Nd}$  diagram (Fig. 8). Much of this variation can be explained by the low REE abundances in layered series rocks and excessive crustal disturbance for some of the marginal and roof zone rocks such that they define mixing lines with the country rocks in Fig. 8. Data for the layered series alone yield an apparent 'age' of  $1400 \pm 260$  Ma with initial  $\epsilon_{\text{Nd}} = -4.5 \pm 5.5$ , and data for roof and marginal zone rocks give apparent ages older than the intrusion ( $\sim 1900$  Ma), reflecting, at least partly, mixing between magmatic and local country rock compositions. Samples from cyclic units 21–25 yield an age of  $\sim 1270$  Ma and a best-fit 'isochron' age for upper layered series and roof zone rocks give an age of  $1267 \pm 66$  Ma with  $\epsilon_{\text{Nd}i} = -1.0 \pm 0.4$  (Fig. 8). This initial ratio is more radiogenic than that calculated for individual rock units by Stewart & DePaolo (1996); we suggest that the true parental magma composition had  $\epsilon_{\text{Nd}i} \geq -1$ .

#### *Country rocks*

Country rocks associated with the Muskox intrusion have negative  $\epsilon_{\text{Nd}i}$  values. Negative  $\epsilon_{\text{Nd}i}$  values have also been measured for the granitic wall-rocks of the intrusion ( $\epsilon_{\text{Nd}1270\text{Ma}} = -20.3$  to  $-22$ ) with a previously reported value for a Wopmay paragneiss ( $\epsilon_{\text{Nd}1270\text{Ma}} = -5.8$ ; Stewart & DePaolo, 1996) being similar to that for a different lithological unit from the same formation reported here ( $-8.7$ ); this may also reflect some degree of Nd isotope heterogeneity in local crustal rocks.

Table 5: Samarium–neodymium isotope data for the Muskox intrusion

| Sample                                 | Sm (ppm) | Nd (ppm) | $^{147}\text{Sm}/^{144}\text{Nd}$ | $^{143}\text{Nd}/^{144}\text{Nd}$ | $\pm 2\sigma$ | $\epsilon_{\text{Nd}}^{1270}$ | $\pm 2\sigma$ |
|--|----------|----------|-----------------------------------|-----------------------------------|---------------|-------------------------------|---------------|
| <i>Muskox intrusion layered series</i> |          |          |                                   |                                   |               |                               |               |
| DDH-MX-N-1                             | 2.97     | 17.1     | 0.1095                            | 0.511330                          | 0.000004      | −11.4                         | 0.2           |
| DDH-MX-N-3                             | 11.13    | 48.7     | 0.1440                            | 0.511945                          | 0.000004      | −5.0                          | 0.2           |
| DDH-MX-N-11                            | 3.96     | 17.5     | 0.1426                            | 0.512142                          | 0.000004      | −0.9                          | 0.2           |
| DDH-MX-N-14                            | 4.66     | 26.9     | 0.1089                            | 0.511843                          | 0.000004      | −1.2                          | 0.2           |
| DDH-MX-N-27                            | 1.89     | 7.72     | 0.1541                            | 0.512239                          | 0.000003      | −0.9                          | 0.1           |
| DDH-MX-N-35                            | 2.23     | 8.74     | 0.1603                            | 0.512310                          | 0.000005      | −0.5                          | 0.2           |
| DDH-MX-N-46                            | 1.35     | 4.83     | 0.1757                            | 0.512390                          | 0.000003      | −1.4                          | 0.1           |
| DDH-MX-N-56                            | 1.53     | 5.16     | 0.1865                            | 0.512498                          | 0.000004      | −1.1                          | 0.2           |
| DDH-MX-N-59                            | 0.38     | 1.31     | 0.1835                            | 0.512458                          | 0.000006      | −1.4                          | 0.3           |
| DDH-MX-N-75                            | 0.12     | 0.43     | 0.1755                            | 0.512331                          | 0.000033      | −2.6                          | 1.3           |
| DDH-MX-N-97                            | 0.20     | 0.72     | 0.1756                            | 0.512389                          | 0.000015      | −1.4                          | 0.6           |
| DDH-MX-N-104                           | 0.45     | 1.44     | 0.1966                            | 0.512616                          | 0.000010      | −0.4                          | 0.4           |
| DDH-MX-N-129                           | 0.09     | 0.33     | 0.1712                            | 0.512375                          | 0.000020      | −1.0                          | 0.8           |
| DDH-MX-S-44                            | 0.08     | 0.34     | 0.1559                            | 0.512069                          | 0.000022      | −4.5                          | 0.9           |
| DDH-MX-S-60                            | 0.04     | 0.17     | 0.1554                            | 0.512238                          | 0.000110      | −1.1                          | 4.3           |
| DDH-MX-S-76                            | 0.23     | 1.00     | 0.1476                            | 0.512150                          | 0.000010      | −1.5                          | 0.4           |
| DDH-MX-S-102                           | 0.42     | 1.71     | 0.1540                            | 0.512175                          | 0.000009      | −2.1                          | 0.3           |
| DDH-MX-S-110                           | 0.48     | 1.93     | 0.1577                            | 0.512276                          | 0.000009      | −0.7                          | 0.4           |
| DDH-MX-S-123                           | 0.46     | 1.62     | 0.1774                            | 0.512355                          | 0.000013      | −2.4                          | 0.5           |
| DDH-MX-S-128                           | 0.37     | 1.53     | 0.1534                            | 0.512148                          | 0.000010      | −2.5                          | 0.4           |
| DDH-MX-S-137                           | 0.54     | 2.12     | 0.1606                            | 0.512209                          | 0.000013      | −2.5                          | 0.5           |
| DDH-MX-S-144                           | 0.49     | 1.87     | 0.1668                            | 0.512245                          | 0.000008      | −2.8                          | 0.3           |
| DDH-MX-S-154                           | 0.77     | 3.27     | 0.1488                            | 0.512174                          | 0.000009      | −1.3                          | 0.4           |
| DDH-MX-S-160                           | 0.90     | 3.81     | 0.1486                            | 0.512177                          | 0.000006      | −1.2                          | 0.2           |
| DDH-MX-S-171                           | 1.33     | 5.75     | 0.1454                            | 0.512203                          | 0.000005      | −0.1                          | 0.2           |
| DDH-MX-S-182                           | 1.56     | 6.54     | 0.1496                            | 0.512203                          | 0.000009      | −0.8                          | 0.4           |
| DDH-MX-S-192                           | 3.91     | 17.6     | 0.1400                            | 0.511830                          | 0.000004      | −6.6                          | 0.1           |
| DDH-MX-S-195                           | 2.20     | 11.2     | 0.1231                            | 0.511582                          | 0.000005      | −8.6                          | 0.2           |
| <i>Keel dyke</i>                       |          |          |                                   |                                   |               |                               |               |
| HDB-2001-MX5                           | 1.64     | 6.29     | 0.1641                            | 0.512290                          | 0.000008      | −1.5                          | 0.3           |

Initial  $\epsilon_{\text{Nd}}$  values were calculated on the basis of the  $^{147}\text{Nd}$  decay constant ( $\lambda$ ) of  $6.54 \times 10^{-12} \text{ year}^{-1}$  and the present-day parameters for chondritic uniform reservoir (CHUR) adopted from Jacobsen & Wasserburg (1980);  $^{147}\text{Sm}/^{144}\text{Nd} = 0.1967$ ,  $^{143}\text{Nd}/^{144}\text{Nd} = 0.512638$ .

## Re–Os isotope and PGE abundance data

### *HSE abundances of layered series and Keel dyke samples*

Re–Os isotope and PGE abundance data for the Muskox intrusion, Keel feeder dyke and local country rocks are presented in Table 6. The abundances of HSE are highly variable throughout the intrusion, with a similar range of abundances for Os, Ir and Ru (Ir- or I-PGE, after Barnes *et al.*, 1985;  $\sim 0.02$ –70 ppb) but more variable ranges in Pt, Pd (Pd or P-PGE, after Barnes *et al.*, 1985) and Re. Common Os ( $\text{Os}^*$ , corrected for radiogenic growth of Os) for the layered series peridotites (0.597–70.3 ppb) is generally lower for that of the main chromitite horizon

(39.9–201 ppb), whereas abundances of Re vary from <0.02 ppb in serpentinized dunite units and clinopyroxenites to 105 ppb in a marginal zone bronzite gabbro. Re concentrations vary between 0.65 and 1.75 ppb in the chromitite horizon and tend to be higher for samples with elevated  $\text{TiO}_2$  and low MgO (Fig. 9), indicating that Re behaves incompatibly and may be partly associated with, or hosted by, Fe–Ti-rich phases.

In comparative plots versus MgO (Fig. 9), the I-PGE follow similar correlations to those of Cr and Ni, indicating their compatibility during fractional crystallization; only the chromitite horizons deviate significantly from

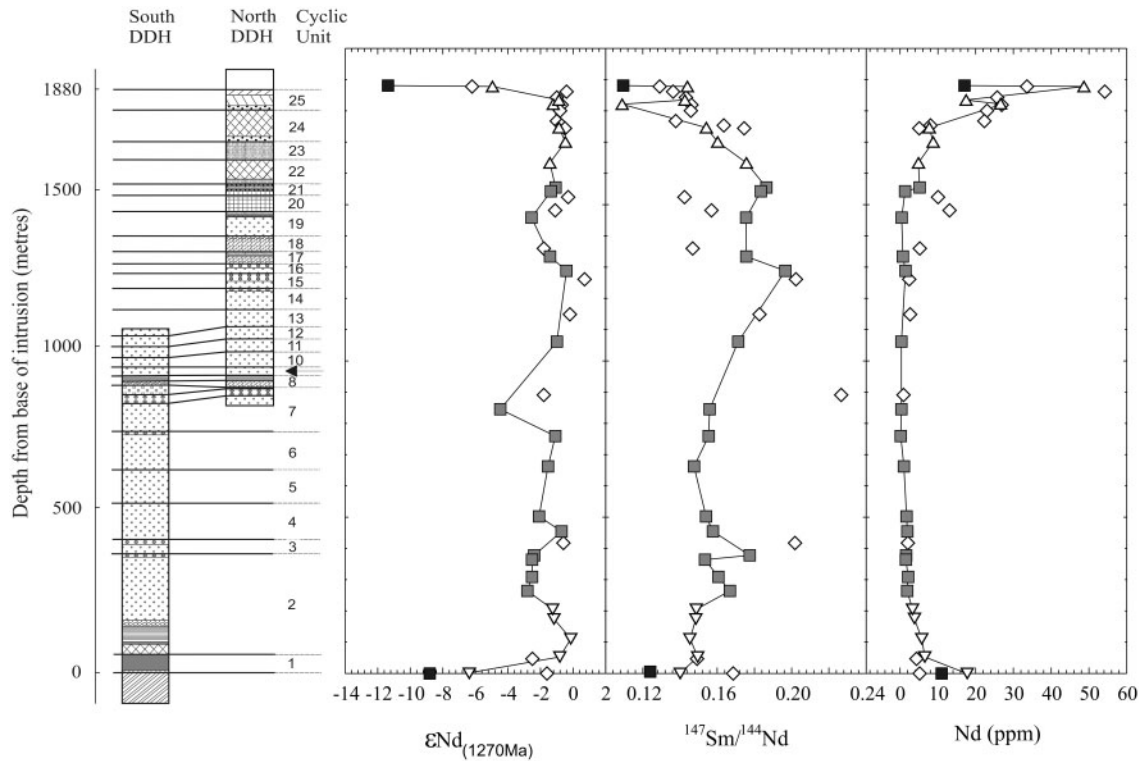


**Fig. 7.** Variations in initial  $\epsilon_{Nd}$  at 1270 Ma,  $^{147}\text{Sm}/^{144}\text{Nd}$  and Nd abundances with depth above the base of the Muskox intrusion.  $\diamond$ , Data from Stewart & DePaolo (1996). Other symbols are as for Fig. 4.

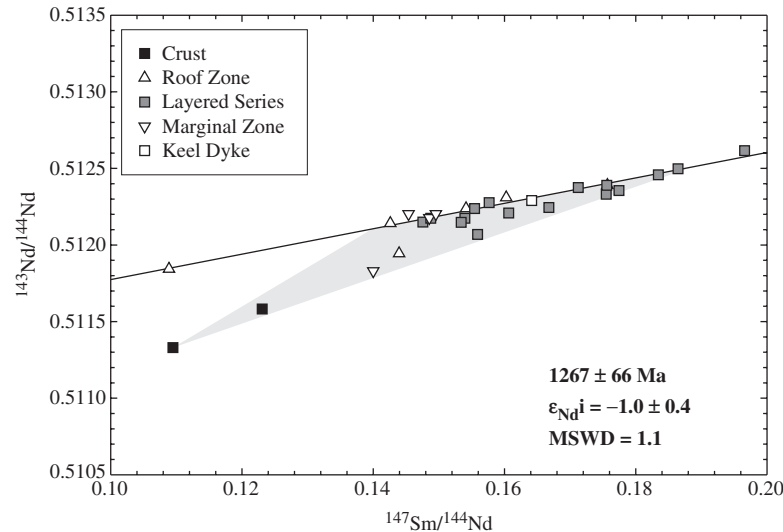


**Fig. 8.**  $^{147}\text{Sm}/^{144}\text{Nd}$  vs  $^{143}\text{Nd}/^{144}\text{Nd}$  plot for the Muskox intrusion layered series, Keel dyke, marginal and roof zone rocks; crustal samples are also shown for comparison but are excluded from isochron analysis. Also shown is the isochron derived from the upper layered series and the roof rocks ( $n = 7$ ) which gives an age of  $1267 \pm 66$  Ma with an initial  $\epsilon_{Nd}^i$  value of  $-1 \pm 2$  assuming a 0.38% relative error for  $^{147}\text{Sm}/^{144}\text{Nd}$  (see text for details). Isochron was calculated using ISOPLOT (Ludwig, 2003). Shaded region denotes possible mixing trajectories between crustal assimilants and Muskox intrusion layered series rocks.

these trends. P-PGE show general compatibility, forming positive correlations with MgO, but Re forms a weak negative correlation, consistent with the more incompatible nature of this element. It is also notable that P-PGE

are as enriched in the most MgO-rich roof and marginal zone rocks as they are in layered series cyclic units. Plots of HSE vs Cr further establish their compatibilities, with the I-PGE exhibiting positive correlations with Cr

Table 6: Highly siderophile element and Os isotope data for the Muskox intrusion

| Sample                                 | Os<br>(ppb) | Ir<br>(ppb) | Ru<br>(ppb) | Pt<br>(ppb) | Pd<br>(ppb) | Re<br>(ppb) | $^{187}\text{Re}/$<br>$^{188}\text{Os}$ | $^{187}\text{Os}/$<br>$^{188}\text{Os}$ | $\pm 2\sigma$ | $\gamma_{\text{Os}1270}$ | $\pm 2\sigma$ |
|--|-------------|-------------|-------------|-------------|-------------|-------------|---|---|---------------|--------------------------|---------------|
| <i>Muskox intrusion layered series</i> |             |             |             |             |             |             |   |   |               |                          |               |
| DDH-MX-N-1                             | 0.018       | 0.022       | 0.023       | 1.292       | 0.231       | 0.595       | 210.8                                   | 2.4180                                  | 0.0056        | -1863                    | 114           |
| DDH-MX-N-3                             | 0.040       | 0.024       | 0.043       | 2.046       | 1.756       | 0.703       | 105.5                                   | 2.0082                                  | 0.0010        | -308                     | 57            |
| DDH-MX-N-11                            | 0.038       | 0.057       | 0.222       | 4.975       | 7.273       | 0.613       | 96.13                                   | 1.7779                                  | 0.0011        | -334                     | 52            |
| DDH-MX-N-14                            | 0.874       | 0.612       | 0.637       | 5.103       | 4.394       | 0.706       | 4.020                                   | 0.18574                                 | 0.00004       | -15.7                    | 2.2           |
| DDH-MX-N-27                            | 0.197       | 0.131       | 0.470       | 0.893       | 7.211       | 0.347       | 8.861                                   | 0.28661                                 | 0.00008       | -17.9                    | 4.8           |
| DDH-MX-N-35                            | 1.827       | 1.484       | 5.235       | 19.41       | 83.09       | 1.672       | 4.424                                   | 0.28173                                 | 0.00004       | 58.1                     | 2.4           |
| DDH-MX-N-46                            | 2.916       | 1.804       | 8.095       | 68.34       | 146.8       | 0.119       | 0.196                                   | 0.13964                                 | 0.00005       | 14.4                     | 0.4           |
| HDB-2000-MX-04a                        | 39.94       | —           | —           | —           | —           | 0.771       | 0.093                                   | 0.15022                                 | 0.00011       | 25.2                     | 5.6           |
| HDB-2000-MX-26a                        | 56.75       | —           | —           | —           | —           | 1.754       | 0.149                                   | 0.14444                                 | 0.00003       | 19.3                     | 6.9           |
| HDB-2000-MX-40a                        | 201.4       | —           | —           | —           | —           | 0.656       | 0.016                                   | 0.13376                                 | 0.00003       | 12.7                     | 24.5          |
| DDH-MX-N-55                            | 1.580       | 1.058       | 1.802       | 0.388       | 0.819       | 0.184       | 0.565                                   | 0.14434                                 | 0.00005       | 11.7                     | 0.4           |
| DDH-MX-N-56                            | 1.469       | 0.927       | 1.723       | 0.851       | 2.843       | 0.146       | 0.482                                   | 0.14968                                 | 0.00007       | 17.7                     | 0.3           |
| DDH-MX-N-59                            | 0.693       | 0.546       | 8.123       | 11.22       | 8.853       | 0.095       | 0.661                                   | 0.14911                                 | 0.00007       | 14.0                     | 0.4           |
| DDH-MX-N-75                            | 70.44       | 50.19       | 49.65       | 36.84       | 21.58       | 0.312       | 0.021                                   | 0.12432                                 | 0.00000       | 4.6                      | 8.2           |
| DDH-MX-N-97                            | 14.44       | —           | —           | —           | —           | 6.329       | 2.129                                   | 0.18412                                 | 0.00005       | 17.1                     | 2.1           |
| DDH-MX-N-100                           | 0.597       | 0.855       | 3.077       | 26.29       | 1.611       | 0.018       | 0.146                                   | 0.12812                                 | 0.00005       | 5.6                      | 0.1           |
| DDH-MX-N-104                           | 4.255       | 1.660       | 19.17       | 10.11       | 6.763       | 0.135       | 0.153                                   | 0.12865                                 | 0.00004       | 5.9                      | 0.5           |
| DDH-MX-N-115                           | 1.621       | 1.491       | 8.142       | 25.57       | 37.64       | 0.509       | 1.487                                   | 0.16225                                 | 0.00005       | 10.2                     | 0.8           |
| DDH-MX-N-129                           | 19.30       | 11.36       | 78.86       | 48.13       | 200.5       | 2.704       | 0.678                                   | 0.14867                                 | 0.00000       | 13.3                     | 2.3           |
| DDH-MX-N-151                           | 4.517       | —           | —           | —           | —           | 0.208       | 0.222                                   | 0.13157                                 | 0.00004       | 7.1                      | 0.6           |
| DDH-MX-S-44                            | 7.741       | 9.765       | 17.18       | 8.597       | 2.671       | 0.022       | 0.012                                   | 0.12277                                 | 0.00003       | 3.5                      | 0.9           |
| DDH-MX-S-51                            | 5.706       | 3.036       | 9.111       | 37.98       | 26.42       | 0.105       | 0.089                                   | 0.12621                                 | 0.00003       | 5.0                      | 0.7           |
| DDH-MX-S-60                            | 0.956       | 0.575       | 2.162       | 99.78       | 80.91       | 0.035       | 0.185                                   | 0.14074                                 | 0.00008       | 15.5                     | 0.2           |
| DDH-MX-S-76                            | 14.52       | —           | —           | —           | —           | 0.160       | 0.053                                   | 0.12714                                 | 0.00003       | 6.4                      | 1.8           |
| DDH-MX-S-102                           | 2.044       | 1.305       | 11.02       | 17.49       | 14.63       | 0.103       | 0.250                                   | 0.14170                                 | 0.00004       | 15.2                     | 0.3           |
| DDH-MX-S-110                           | 3.887       | 2.929       | 7.597       | 29.13       | 28.50       | 0.079       | 0.087                                   | 0.12553                                 | 0.00001       | 4.4                      | 0.5           |
| DDH-MX-S-123                           | 1.846       | 0.928       | 6.711       | 83.18       | 4.663       | 0.029       | 0.076                                   | 0.13271                                 | 0.00059       | 10.7                     | 1.1           |
| Rpt                                    | 0.918       | 0.900       | 6.866       | 82.89       | 7.640       | 0.047       | 0.247                                   | 0.12881                                 | 0.00005       | 4.3                      | 0.2           |
| DDH-MX-S-128                           | 6.246       | 5.504       | 15.55       | 115.2       | 20.63       | 0.105       | 0.080                                   | 0.12444                                 | 0.00001       | 3.6                      | 0.7           |
| DDH-MX-S-133                           | 5.347       | 4.457       | 12.50       | 51.20       | 9.261       | 0.072       | 0.065                                   | 0.12353                                 | 0.00003       | 3.1                      | 0.7           |
| DDH-MX-S-137                           | 9.092       | —           | —           | —           | —           | 2.783       | 1.488                                   | 0.25393                                 | 0.00007       | 87.6                     | 1.4           |
| DDH-MX-S-144                           | 6.554       | 6.229       | 15.80       | 31.12       | 13.65       | 0.141       | 0.103                                   | 0.12614                                 | 0.00002       | 4.7                      | 0.8           |
| DDH-MX-S-151                           | 5.993       | 6.099       | 18.87       | 48.15       | 103.9       | 0.234       | 0.185                                   | 0.13015                                 | 0.00004       | 6.6                      | 0.7           |
| DDH-MX-S-154                           | 6.546       | 6.607       | 15.94       | 68.92       | 153.3       | 0.198       | 0.146                                   | 0.13198                                 | 0.00005       | 8.8                      | 0.8           |
| DDH-MX-S-160                           | 5.291       | —           | —           | —           | —           | 1.262       | 1.159                                   | 0.19159                                 | 0.00005       | 40.9                     | 0.9           |
| DDH-MX-S-171                           | 3.098       | 3.280       | 6.847       | 11.63       | 49.73       | 0.348       | 0.531                                   | 0.13811                                 | 0.00004       | 7.1                      | 0.5           |
| DDH-MX-S-182                           | 2.470       | 1.955       | 6.665       | 28.83       | 2.585       | 0.378       | 0.734                                   | 0.13626                                 | 0.00005       | 1.8                      | 0.5           |
| DDH-MX-S-192                           | 3.342       | 1.297       | 46.50       | 14.72       | 22.331      | 119.5       | 207.6                                   | 2.93012                                 | 0.00053       | -1373                    | 112           |
| DDH-MX-S-195                           | 0.189       | 0.106       | 0.288       | 2.287       | 6.318       | 0.631       | 15.59                                   | 0.73451                                 | 0.00037       | 238.9                    | 8.4           |
| <i>Muskox Keel dyke</i>                |             |             |             |             |             |             |   |   |               |                          |               |
| MU 033.241.21                          | 2.203       | 1.749       | 7.027       | 14.58       | 1.065       | 0.330       | 0.723                                   | 0.13661                                 | 0.00003       | 2.3                      | 0.5           |
| MU 033.252.76                          | 1.937       | 1.581       | 6.157       | 10.21       | 2.457       | 0.398       | 0.997                                   | 0.14797                                 | 0.00226       | 7.0                      | 3.9           |
| Rpt                                    | 1.894       | 1.562       | 4.916       | 9.600       | 2.330       | 0.416       | 1.068                                   | 0.14242                                 | 0.00004       | 1.0                      | 0.6           |
| HDB-2001-MX5                           | 1.612       | 1.441       | 5.845       | 15.79       | 4.257       | 0.482       | 1.446                                   | 0.15401                                 | 0.00004       | 4.0                      | 0.8           |

Initial  $\gamma_{\text{Os}}$  values were calculated on the bases of the  $^{187}\text{Re}$  decay constant ( $\lambda$ ) of  $1.666 \times 10^{-11} \text{ year}^{-1}$  [see Selby *et al.* (2007) for a review] and the present-day average chondritic composition adopted from Shirey & Walker (1998):  $^{187}\text{Re}/^{188}\text{Os} = 0.40186$ ,  $^{187}\text{Os}/^{188}\text{Os} = 0.1270$ .

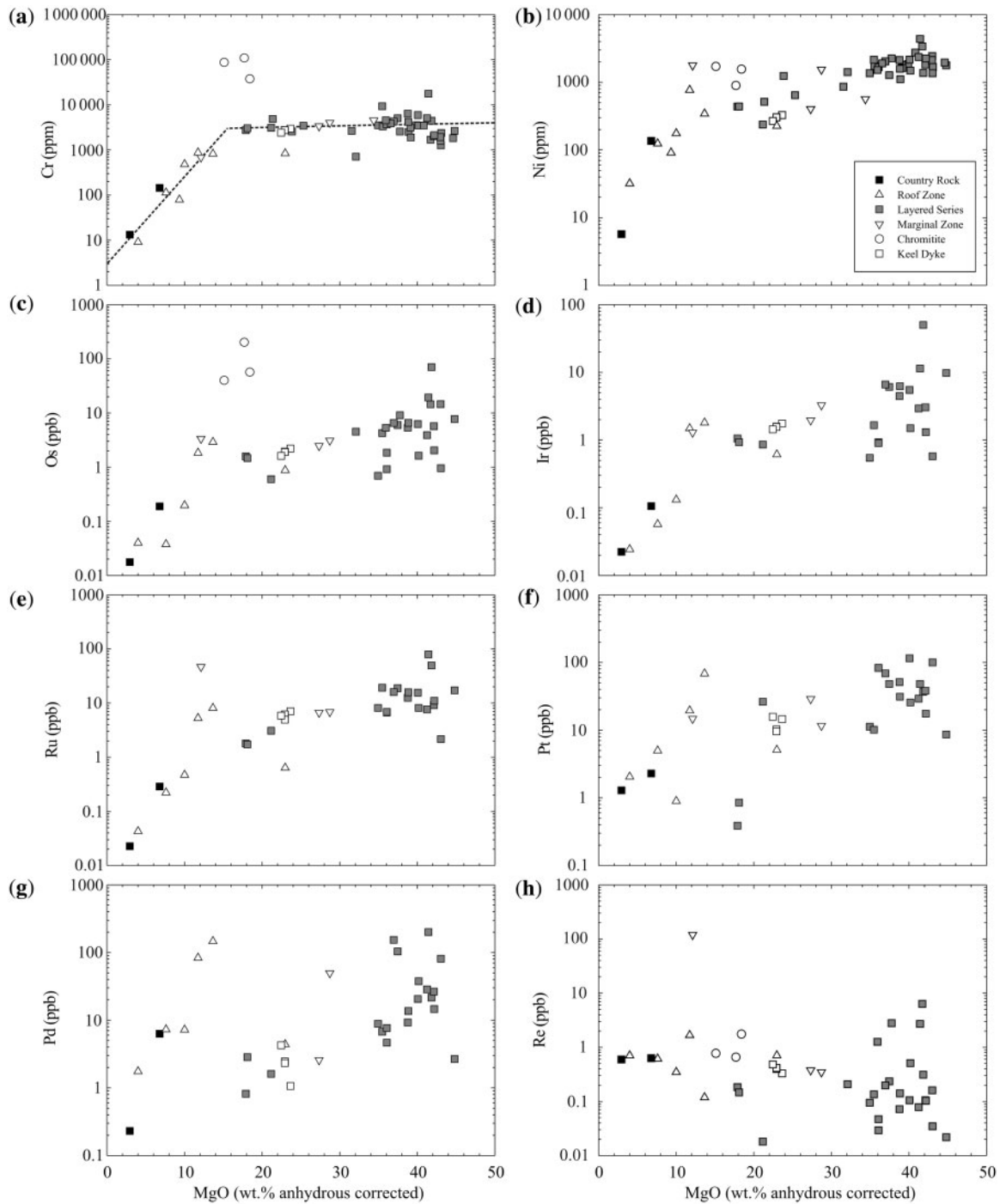


**Fig. 9.** MgO vs (a) Cr, (b) Ni and (c–h) highly siderophile elements in the Muskox intrusion units. Ir platinum-group elements (I-PGE; Os, Ir, Ru) show similar correlations with MgO to the compatible elements Cr and Ni. P-PGE (Pt, Pd) show more scatter vs MgO, but are generally compatible, and Re is the only element to show a broadly inverse correlation with MgO. Line in (a) reflects accumulation/fractionation trajectories defined by Cr-MgO relationships.

( $R^2$  value  $>0.7$ ) and the P-PGE and Re showing weaker correlations ( $R^2$  value  $<0.2$ ), especially for the layered series units (Fig. 10). It was previously suggested that cumulus chromite and olivine would control the I-PGE and Pt,

whereas Pd, Au, Re and Cu behave incompatibly (Barnes & Francis, 1995). Our data indicate that the I-PGE are likely to be controlled by chromite and olivine, but that the P-PGE and Re are less compatible. These plots help to

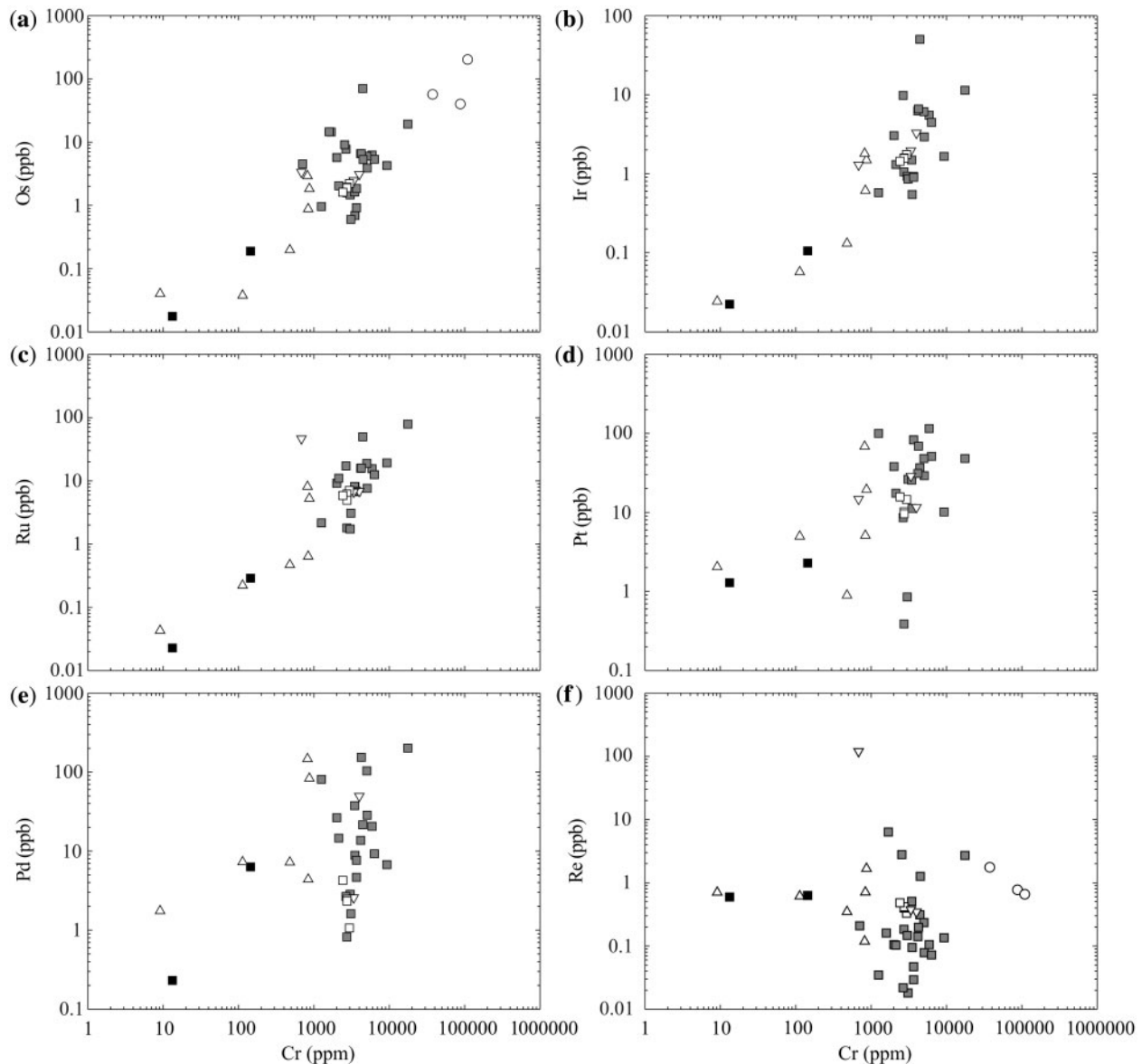


**Fig. 10.** Cr vs (a) Os, (b) Ir, (c) Ru, (d) Pt, (e) Pd and (f) Re in the Muskox intrusion units. I-PGE show well-defined positive correlations with Cr, whereas P-PGE and Re show greater scatter. These results are consistent with early formed phases (PGE-rich inclusions within chromite and olivine) controlling I-PGE distribution in the Muskox intrusion layered series units.

establish a relative order of compatibility of PGE and Re in the intrusion:

$$D_{\text{Ir}} \sim D_{\text{Os}} \sim D_{\text{Ru}} > D_{\text{Pt}} > D_{\text{Pd}} > D_{\text{Re}}.$$

This is consistent with the work of Barnes & Francis (1995) and also with the correlations between I-PGE ( $R_{(\text{Os}/\text{Ir})} = 0.98$ ;  $R_{(\text{Ru}/\text{Ir})} = 0.89$ , excluding samples N-129 and S-192 for Ru/Ir) and P-PGE vs Ir, the latter of which show little or no correlation (Fig. 11).

There is a diverse range of HSE patterns for Muskox intrusion rocks (Fig. 12), with layered series rocks having distinctive patterns according to their cyclic units.

Some of the variability, especially in samples with less than 10 ppb of Os, Ir, Ru, Pt, Pd or Re, may result from the 'nugget effect', where the limited sample mass (2–3 g) digested and PGE-mineral distribution and grain size play a major role; this, however, should have limited effect on the HSE patterns exhibited in Fig. 12. Some of the variability can also be ascribed to lithological differences. Pyroxenites (N-100, S-123) have distinctive inverted 'V' shaped patterns and are characterized by supra-chondritic  $(\text{Pt}/\text{Os})_n$  of  $\sim 30$ . Websterites in cyclic units 16–21 (N-55, N-56) have relatively flat patterns with relative depletion in Pt compared with Pd and Ru. Dunites generally have

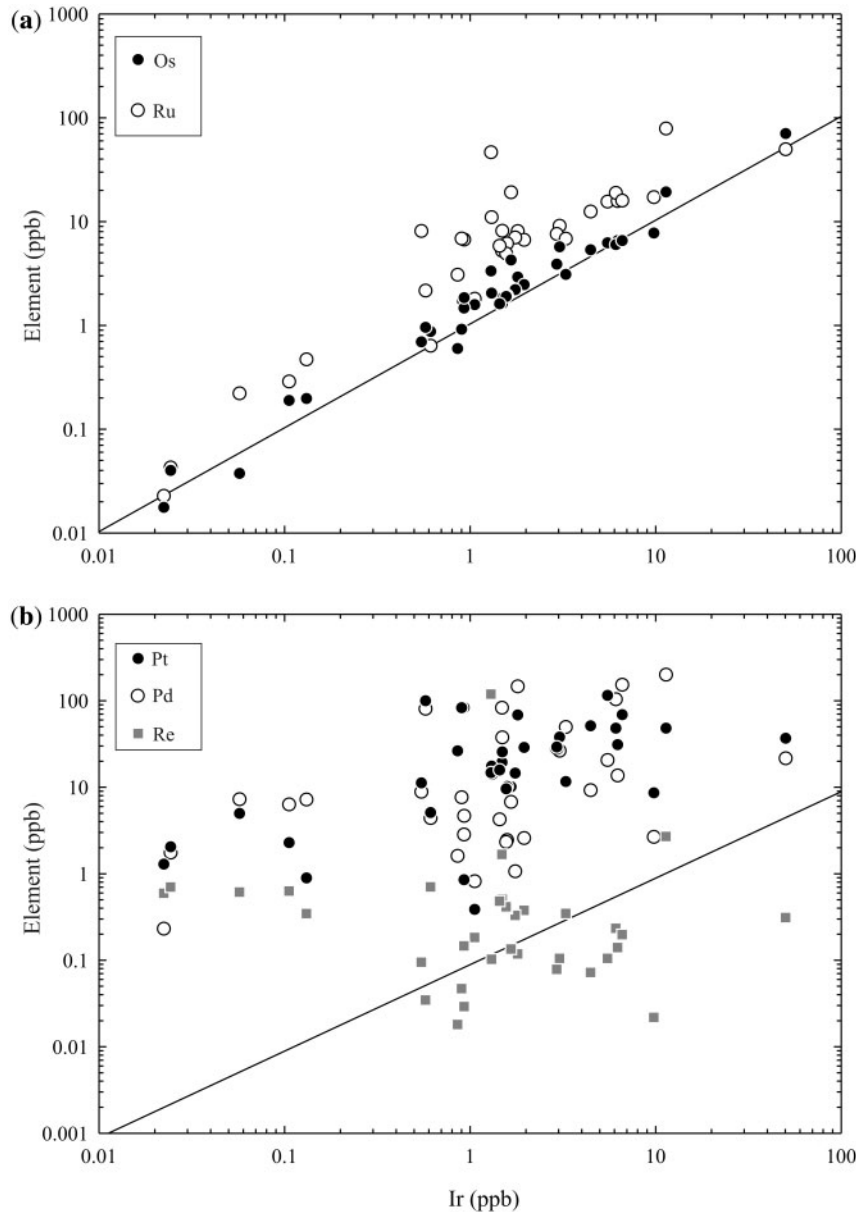


**Fig. 11.** Covariations of the concentrations (in parts per billion) of (a) I-PGE, Os and Ru and (b) P-PGE (Pt, Pd) and Re vs Ir for Muskox intrusion rocks. Os and Ru show good correlation with Ir ( $R^2=0.98$  and  $0.85$ , respectively, excluding S-192 and N-129 from Ru correlation) but the P-PGE and Re show little to no correlation with I-PGE ( $R^2 < 0.1$ ). Chondritic lines for (a) Os and (b) Re are from Horan *et al.* (2003).

HSE patterns characterized by positive slopes for the PGE. Apparent depletions in Pt relative to Pd and Ru in some layered series rocks may reflect localized fractionation of Cu-rich sulphide liquid; pyrrhotite, pentlandite and monosulphide solid solution have been shown to exhibit these characteristics in Noril'sk, Bushveld and Great Dyke samples (Barnes *et al.*, 2006, 2008). Barnes & Francis (1995) noted a similar Cu-rich sulphide sample (Eq 16) to S-192 in their analyses of Muskox intrusion rocks. Keel dyke samples of gabbro norite possess HSE patterns with Pd depletions, are relatively homogeneous and show

similar patterns to picritic magmas from other localities (Crocket, 2002; Fig. 12). Some of the variability in HSE patterns cannot solely be attributed to lithology and instead is probably related to sulphide control, especially in the marginal zones, or crustal assimilation, with country rocks having positive HSE profiles and supra-chondritic (Re, P-PGE/I-PGE)<sub>n</sub> (normalized to CI-Chondrite, Orgueil). Many of the roof zone samples are characterized by positive HSE patterns, similar to those of the Hornby Bay sandstone roof rock, or Wopmay paragneiss. Even some of the layered series dunites (S-151, S-154) show enrichments

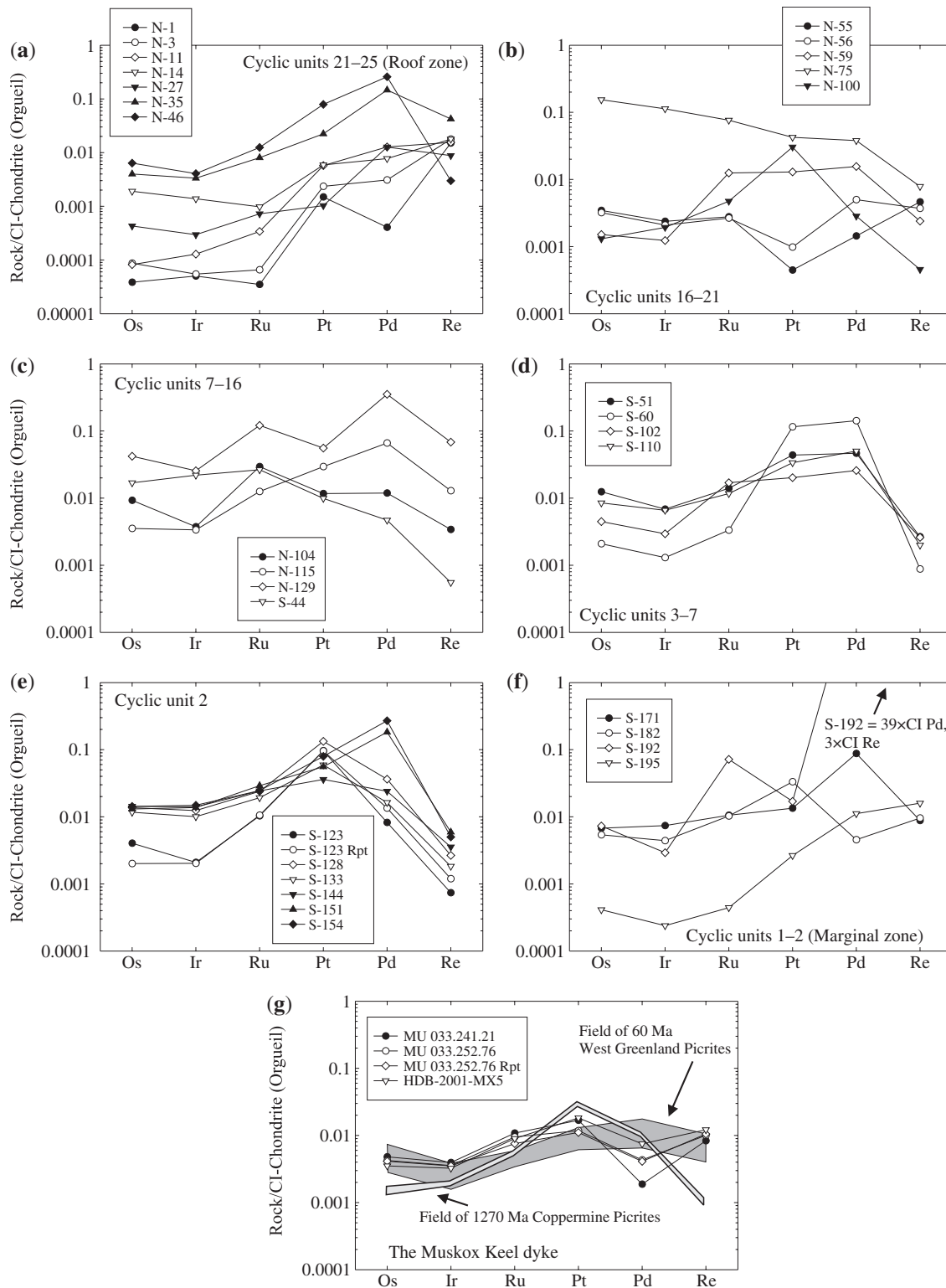


**Fig. 12.** Highly siderophile element (HSE) patterns for Muskox intrusion rocks, including (a) the roof zone; (b) cyclic units 16–21; (c) cyclic units 7–16; (d) cyclic units 3–7; (e) cyclic unit 2; (f) cyclic units 1 and 2 (the marginal zone); (g) the Muskox Keel feeder dyke. There are distinct differences in HSE patterns between the different lithologies, with pyroxenites possessing inverted ‘V’ patterns, websterites (N-55 and N-56) having relatively flat patterns with Pt depletions relative to Ru and Pd and dunites having high P-PGE/I-PGE but low Re. Samples in the roof zone show similar abundance patterns to country rocks with an extremely limited range of Re abundances. Marginal zone rocks show enrichments in Pd; the Keel dyke shows Pd depletion relative to Pt and Re. Normalization values are from Horan *et al.* (2003), field of West Greenland picrite data from Pearson & Woodland (2000), field of Coppermine volcanic picrites from Day *et al.* (in preparation).

in Pd in the lower portion of cyclic unit 2, adjacent to the marginal zone.

PGE data for the Muskox intrusion have previously been obtained by nickel sulphide fire assay and instrumental neutron activation analysis (INAA) by Barnes & Francis (1995). That work focused extensively on PGE-rich marginal zone sulphides and a detailed description of the sulphide mineralogy of the intrusion. We compare our isotope dilution HSE data with the NiS-INAA data of Barnes & Francis (1995) and find overall agreement in PGE and Re concentrations as a function of S, even with country rock gneiss and Cu-rich sulphide samples included (Fig. 13). There is clear evidence for sulphide control, in both our dataset and that of Barnes & Francis (1995), especially for the marginal zone samples and country rocks. Base metal sulphide (BMS) liquid, which has extremely high affinity for the HSE, probably played an important role in the distribution of these elements in the marginal zones of the intrusion, with layered series rocks showing less dependence on this process (Fig. 13). Indeed, Barnes & Francis (1995) noted correlations between Cu, Re, Rh, Pd, and Au in marginal zone samples, which they attributed to sequestration of HSE through sulphide addition from country rocks; the marginal zone samples from this study appear to be consistent with their conclusions, although the layered series units do not.

A striking aspect of the I-PGE data is that the layered series rocks of the Muskox intrusion have near-chondritic  $(\text{Os}/\text{Ir})_n$  that varies by only 0.68–2.50 through the intrusion as a whole. In contrast, supra-chondritic ratios of  $(\text{Pt}/\text{Os})_n$ ,  $(\text{Re}/\text{Os})_n$  and  $(\text{Pd}/\text{Ir})_n$  are evident in both the roof and marginal zone rocks but are less pronounced in dunitic and peridotitic units [ $(\text{Os}/\text{Ir})_n = 1.2 \pm 0.6$ ,  $(\text{Pt}/\text{Os})_n = 3.9 \pm 2.9$ ,  $(\text{Re}/\text{Os})_n = 0.6 \pm 0.9$ ] and in Keel dyke samples [ $(\text{Os}/\text{Ir})_n = 1.2 \pm 0.1$ ,  $(\text{Pt}/\text{Os})_n = 3.5 \pm 1.2$ ,  $(\text{Re}/\text{Os})_n = 2.7 \pm 0.7$ ]. It is useful to consider the relationship of HSE with depth in the intrusion, considering the interpretation of replenishment episodes to form the layered series cyclic units (Findlay & Smith, 1965; Irvine & Smith, 1967). The I-PGE behave like Cr in the intrusion (Fig. 14), whereas Re acts more incompatibly and is lowest in the layered series peridotites and pyroxenites. The P-PGE show pronounced oscillations and, with the I-PGE, are consistent with periodic magma replenishment and fractional crystallization defining the formation of the Muskox layered series cyclic units. With depth from the base of the intrusion (defined as the contact between the country rock and the floor of the intrusion), Os/Ir is essentially invariant,  $\sim 1$ –1.5, but Pt/Ir shows much greater variation, again consistent with magmatic fractionation of the I-PGE and P-PGE and periodic magma replenishment to the intrusion. Re/Os ratios are greatest in the marginal and roof zone rocks and can be extremely low in the layered series and chromitite horizon (Fig. 14). Fluid-immobile

lithophile and chalcophile elements, such as Pb, also show change in abundance with depth from base in the intrusion, consistent with periodic magma replenishment to form the layered series cyclic units, but more mobile lithophile elements are depleted, especially in the heavily serpentinized areas of the intrusion (cyclic units 6–21; Table 1).

#### *HSE abundances of country rocks*

The two country rocks analysed, the Hornby Bay sandstone and Wopmay paragneiss, both have distinctive HSE patterns, with  $(\text{Re}, \text{P-PGE}) > \text{I-PGE}$  (Fig. 12). Broadly speaking, both country rocks have lower HSE abundances than the layered series rocks and the Keel dyke, with the Hornby Bay sandstone having systematically lower PGE and Re abundances than the Wopmay paragneiss.

#### *Re–Os isotope systematics*

Measured  $^{187}\text{Os}/^{188}\text{Os}$  ( $^{187}\text{Os}/^{188}\text{Os}_m$ ) for the Muskox intrusion and Keel dyke samples are sub-chondritic to highly radiogenic (0.1228–2.93). Layered series units have the lowest  $^{187}\text{Os}/^{188}\text{Os}_m$  (0.1228–0.2539), and the chromitite horizon also exhibits a restricted range of  $^{187}\text{Os}/^{188}\text{Os}_m$  compositions (0.1338–0.1502). Initial Os isotope compositions ( $\gamma_{\text{Os}i}$ ; age corrected to 1270 Ma) are in excess of chondritic values for all layered series peridotites and span a large range (+1.8 to +87.6), showing oscillating variation with stratigraphic height and more positive  $\gamma_{\text{Os}i}$  values progressively up the layered series succession (Fig. 14). Keel dyke samples have a more restricted range of positive  $\gamma_{\text{Os}i}$  values (+1 to +7). Variations in  $\gamma_{\text{Os}i}$  weakly correlate with cyclic unit intervals in the intrusion. Cyclic unit 2, the thickest of the ultramafic layered series units studied, exhibits almost the entire range measured for  $\gamma_{\text{Os}i}$  in the intrusion. It includes layers with high Os\* abundances (0.92–9.1 ppb) but highly variable  $\gamma_{\text{Os}i}$  (+3.1 to +87.6). The highest  $\gamma_{\text{Os}i}$  is seen in the high Os\* dunite (S-137), which has been interpreted as the cryptic representation of a laterally discontinuous chromite-rich horizon in cyclic unit 2.  $\gamma_{\text{Os}i}$  is  $>10$  for all of the chromitite horizon rocks. There are no obvious correlations between Os\* and  $\gamma_{\text{Os}i}$  in the Muskox intrusion rock suite.

Muskox intrusion samples do not define an isochronous relationship and show considerable scatter on a Re–Os isochron plot (Fig. 15). The main correlation defines a much younger mean age than the age of crystallization of the intrusion from U–Pb concordia (LeCheminant & Heaman, 1989). Some of the scatter in the Re–Os isochron plot can be explained by post-crystallization disturbance via apparent Re loss or gain. A number of the marginal and roof zone samples have Re excess such that their  $\gamma_{\text{Os}i}$  values are highly negative; these samples include S-192; N-3, N-11, N-14 and N-27, all of which lie either side of a 900 Ma reference isochron in Fig. 15. In addition to Re mobilization, these samples possess fluid-mobile element

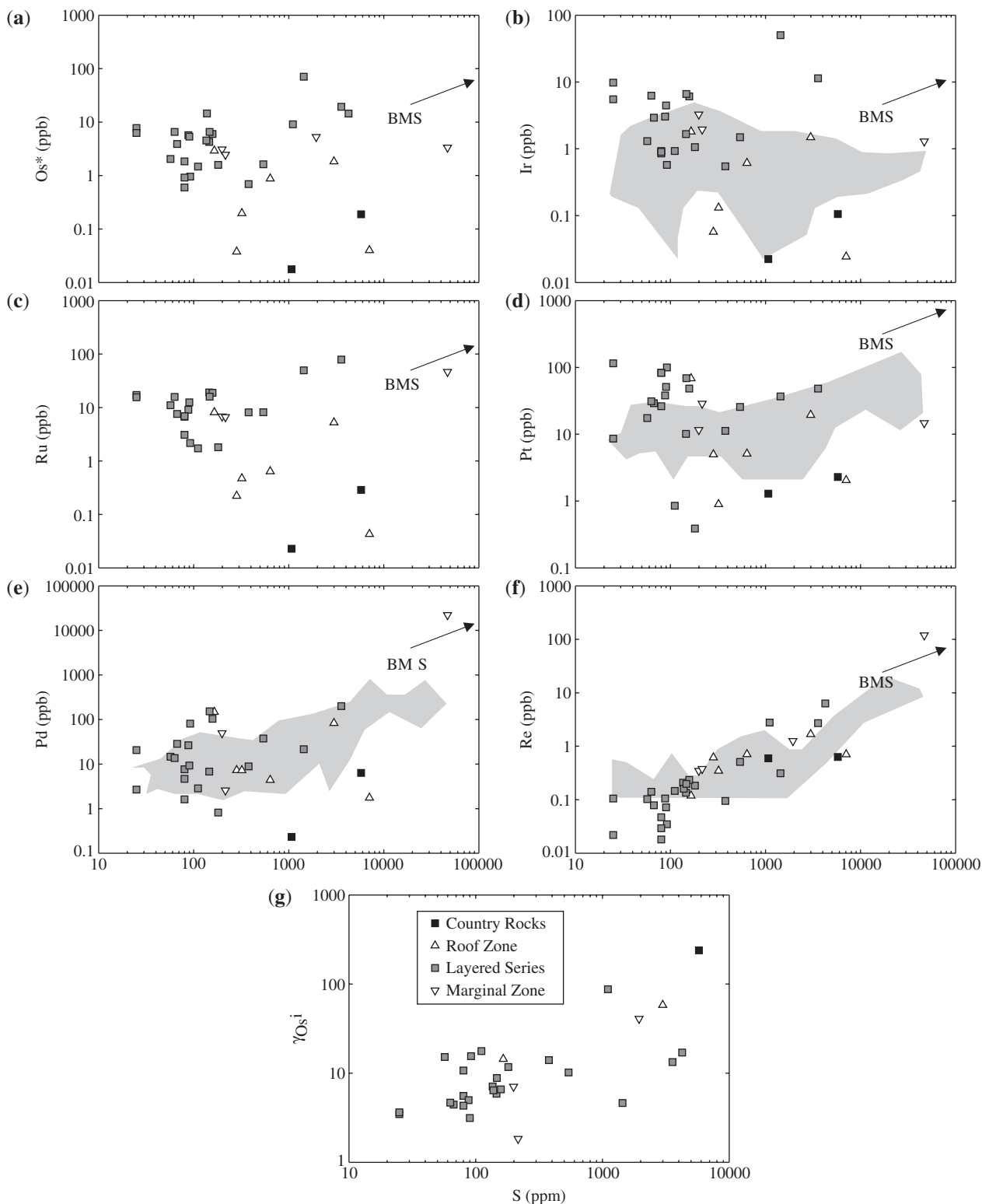


**Fig. 13.** Covariations of highly siderophile elements and  $\gamma_{Os1270Ma}$  with sulphur content in the Muskox intrusion. (a) Os\*, (b) Ir, (c) Ru, (d) Pt and (e) Pd show little to no correlation with S but it is notable that the marginal and roof zone rocks lie toward the compositions of the country rocks. A good correlation exists between Re and S (f) and also, to a lesser degree, between  $\gamma_{Os1270Ma}$  and S (g). These correlations are attributed to interaction with base metal sulphide species [BMS—vector calculated from data of Barnes & Francis (1995) and Barnes *et al.* (2006, 2008)] as well as possible hydrothermal mobilization of Re from the centre to the top of the Muskox intrusion. Shaded field is from Barnes & Francis (1995) based on their INAA data for Muskox intrusion samples.

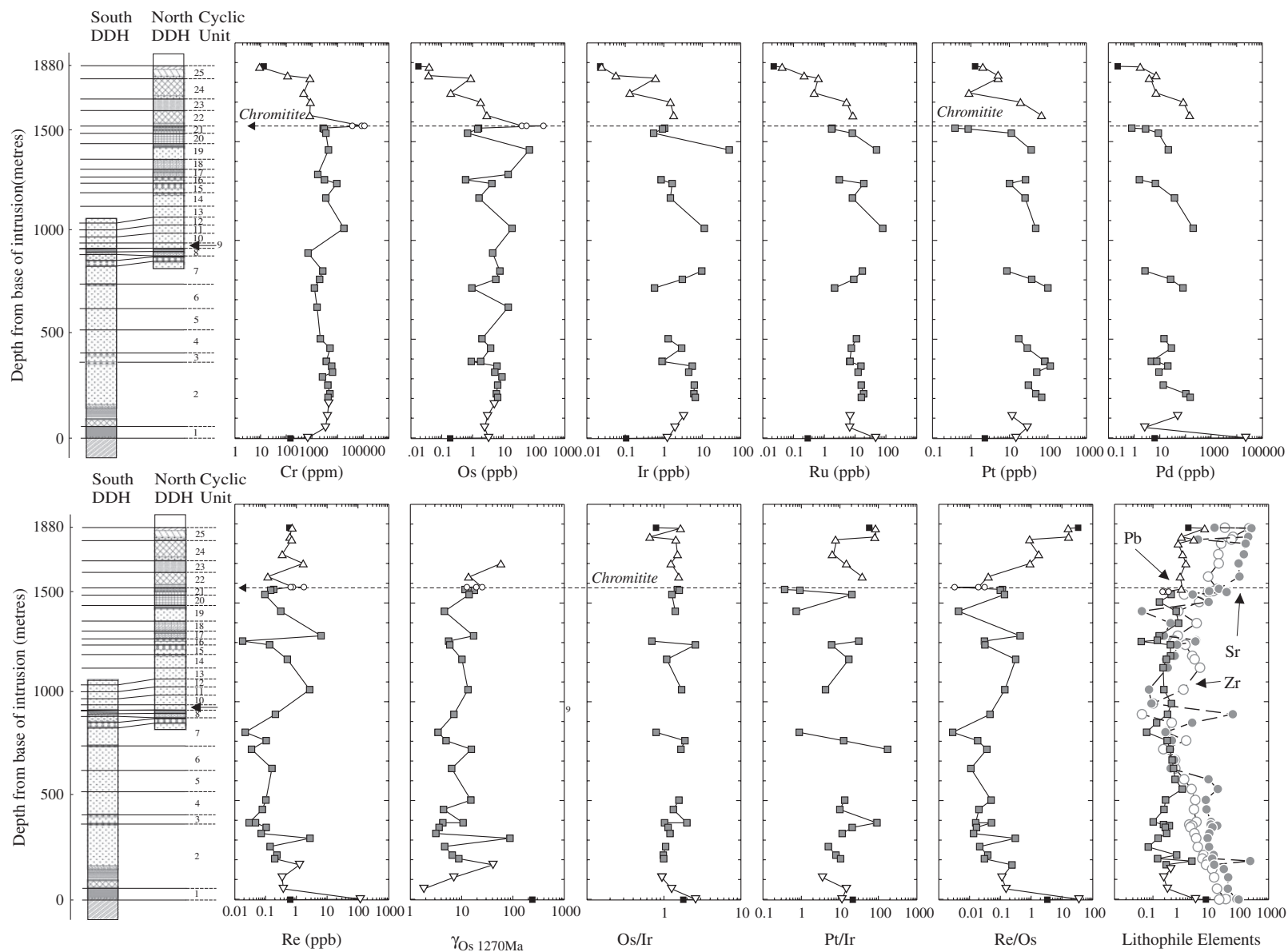


**Fig. 14.** Variations in Cr, Os, Ir, Ru, Pt, Pd and Re abundances,  $\gamma_{Os1270Ma}$ , Os/Ir, Pt/Ir, Re/Os and lithophile element (Pb, Sr and Zr) abundances with depth from base in the MuskoX intrusion. Arrows denote the locations of the main chromitite horizons. There are notable similarities between oscillating variation in I-PGE abundances and Cr and between P-PGE and depth. Some of this oscillation can be explained via new magma pulses feeding the layered series cyclic units. Much of the variation can also be explained via fractionation and accumulation of mafic minerals in the intrusion.

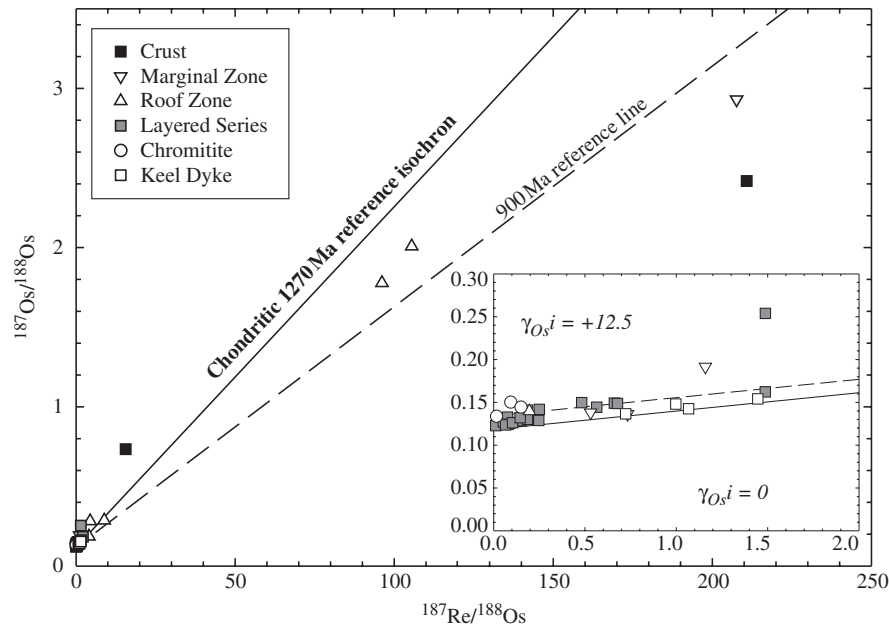


**Fig. 15.**  $^{187}\text{Re}/^{188}\text{Os}$  vs  $^{187}\text{Os}/^{188}\text{Os}$  plot for the Muskox intrusion layered series, Keel dyke, marginal and roof zone rocks; crustal samples are also shown for comparison. A best-fit 900 Ma reference line (excluding crustal samples) is shown for roof and marginal zone rocks along with a chondritic 1270 Ma reference isochron. Inset shows low Re/Os samples. Most layered series and all Keel dyke samples lie along, or slightly above the chondritic 1270 Ma isochron with Keel dyke samples having  $\gamma_{\text{Os}^i} = +1.2 \pm 0.3$ . Whereas most layered series cyclic units lie on or around the chondritic 1270 Ma reference line, chromitites and some high  $\text{Os}^*$  layered series rocks lie on or above a 1270 Ma reference isochron corresponding to a  $\gamma_{\text{Os}^i}$  value of  $\sim +12.5$ . The non-isochronous relations for the Muskox intrusion rocks probably reflect post-magmatic disturbance and heterogeneous melt compositions from mixing between new pulses of magma feeding the intrusion and crustally contaminated, evolved liquid compositions.

(e.g. Ba, Rb) anomalies (e.g. Fig. 6). More coherent behaviour is observed when samples from the marginal and roof zones are excluded. The Keel dyke samples, along with the majority of layered series rocks, scatter around a 1270 Ma chondritic reference isochron. The most radiogenic layered series peridotites from cyclic units 2–19 are displaced and scatter about a similar 1270 Ma reference isochron that has a higher  $\gamma_{\text{Os}^i}$  value of approximately +12.5. This relationship indicates initial isotopic heterogeneity in the magmas hosted within the intrusion, accounting for some of the scatter in the Re–Os isochron plot (Fig. 15). Such isotopic heterogeneity is consistent with the dynamic interplay of magma replenishment, fractional crystallization and crustal assimilation already noted from the elemental systematics of the intrusion and with other layered intrusions (e.g. Lambert *et al.*, 1994). Filtering the dataset to remove samples affected by post-crystallization disturbance (negative  $\gamma_{\text{Os}^i}$ ), or that possess elevated  $\gamma_{\text{Os}^i}$  (greater than +10), yields an imprecise ‘errorchron’ age of  $1276 \pm 170$  Ma (MSWD = 260,  $n = 19$ ) with a positive  $\gamma_{\text{Os}^i}$  ( $+5 \pm 2$ ). Regressing a 1270 Ma reference isochron through Keel dyke samples yields  $\gamma_{\text{Os}^i} = +1.2 \pm 0.3$ . Variability in initial Os compositions of Muskox intrusion rocks strongly argues for different parental melt compositions as a result of periodic magma replenishment episodes to feed the layered series cyclic units and a crucial role for crustal assimilation processes.

## DISCUSSION

### Hydrothermal alteration and mobilization of rhenium

Post-crystallization hydrothermal alteration of Re or radiogenic Os has previously been postulated for a number of layered intrusions (Hart & Kinloch, 1989; McCandless & Ruiz, 1991; Marcantonio *et al.*, 1993, 1994; Lambert *et al.*, 1994). This process has been interpreted to occur via addition of crust-derived Os through transfer in fluids during cryptic metasomatism (Marcantonio *et al.*, 1994).

There is extensive petrographic and geochemical evidence for hydrothermal processes altering some of the Muskox intrusion layered cyclic units. This includes: (1) cryptic metasomatism in layered series rocks (Irvine, 1980); (2) serpentinization and presence of Mg-rich chlorite in middle (cyclic units 7–16) layered series peridotites (Table 1); (3) absence of sulphides, zonation of native metals (e.g. awaruite, wairuite, mackinawite, vallerite) and existence of native iron and copper in the core zone of the Muskox intrusion (Chamberlain & Delano, 1965; Chamberlain *et al.*, 1965; Chamberlain, 1967); (4) deuterium oxygen isotope exchange between minerals and fluids (Taylor, 1968). These features can be explained by hot fluids fluxing through the intrusive pile subsequent to crystallization. Chamberlain (1967) suggested that, during

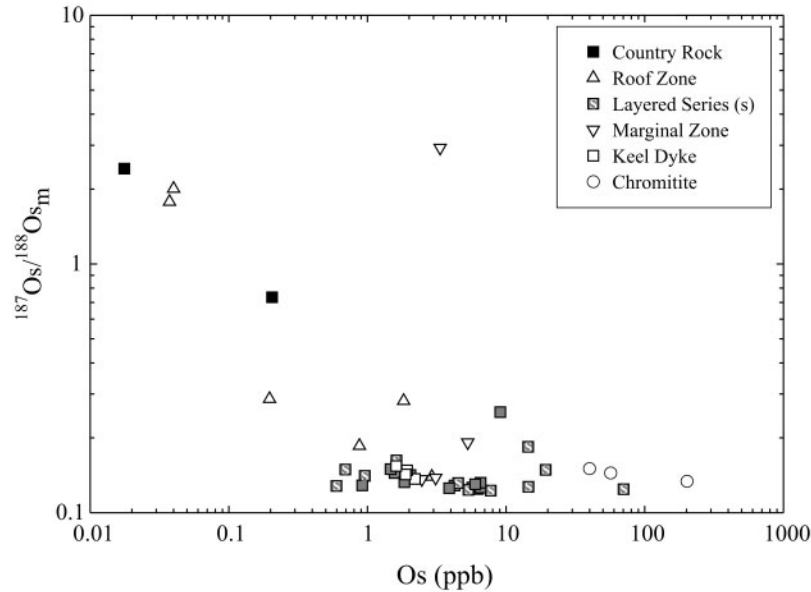


**Fig. 16.** Initial  $^{187}\text{Os}/^{188}\text{Os}$  vs Os (ppb) for Muskox intrusion rocks. The relationship of low Os and radiogenic  $^{187}\text{Os}/^{188}\text{Os}$  has previously been ascribed to hydrothermal mobilization of radiogenic Os in the Wellgreen intrusion (Marcantonio *et al.*, 1994). For the Muskox intrusion it is more likely that Re has been mobilized, as this can more effectively account for low Os abundance marginal and roof zone rock Os isotope compositions and Re/Os ratios; the radiogenic  $^{187}\text{Os}/^{188}\text{Os}$  for high Os abundance samples are therefore related to crustal contamination. Samples that fall in the serpentinized zone of the intrusion (Fig. 2) are denoted by an 's' within the symbol.

serpentinization of the intrusion, hydrothermal fluids became progressively O-depleted, resulting in the decomposition of sulphide phases, ultimately resulting in formation of native metal species in the serpentinized units and  $\text{H}_2\text{S}$  in the fluid phase. It should be noted that, although evident in some samples, this process has by no means been pervasive through the intrusion, with the most focused alteration occurring in the 'core' of the intrusion from  $\sim 500$  to  $\sim 1500$  m depth from base (DFB) and away from the side-walls of the intrusion (e.g. Fig. 2).

Concentrations of fluid-immobile elements such as the REE, Hf, Nb and Th have not been altered by hydrothermal alteration in the Muskox intrusion, but LILE (e.g. Rb, Sr, Ba, Cs) show greater scatter, relative to indices of fractionation such as Zr (Table 3). The highly negative  $\gamma_{\text{Os},i}$  values for some of the roof and marginal zone rocks indicate disturbance of the Re–Os isotope system. There is a trend to evolved, lower Os abundance marginal and roof zone rocks that possess more radiogenic measured  $^{187}\text{Os}/^{188}\text{Os}$  (Fig. 16); this relationship can be attributed to high Re/Os ratios in low Os abundance samples that are sensitive to Re gain, as well as the increasing effect of crustal contamination. We suggest that Re gain occurred through addition of a rhenium sulphide species relating to low oxygen activity fluids. Rhenium correlates positively with sulphur in the intrusion, implying that fluids broke down and transported interstitial sulphide phases from the base to the top and sides of the intrusion (Fig. 13). Further, the samples that possess the most negative  $\gamma_{\text{Os},i}$

values also have large positive fluid-mobile element anomalies (e.g. Fig. 6). Conversely, the PGE show no well-defined correlations with S (Fig. 13). Rhenium gain in samples can explain negative  $\gamma_{\text{Os},i}$  values, which also semi-correlate with S (Fig. 13), for some of the marginal and roof zone rocks, accounting for their scatter to the right of the 1270 Ma reference isochron line and yielding an artificially younger 'age' than the 'true age' of the intrusion (Fig. 15).

In contrast to marginal and roof zone rocks, the effect of Re mobilization has been minimal for layered series peridotites, which show a relatively limited range of  $^{187}\text{Os}/^{188}\text{Os}_m$  with variable Os concentration (Fig. 16). There is no evidence for radiogenic Os gain through hydrothermal mobilization for samples with high Os concentrations and radiogenic  $^{187}\text{Os}/^{188}\text{Os}$  in the Muskox intrusion. If this were true, it would be expected that a relationship should exist between the degree of serpentinization in ultramafic layered series rocks and initial  $^{187}\text{Os}/^{188}\text{Os}$ , yet no correlation can be defined (see Table 1 and Fig. 16). Furthermore, similar stratigraphic profiles for the I-PGE vs compatible elements (e.g. Cr, Ni; Fig. 14) indicate that layered series units have preserved their magmatic Os abundances. Similar observations have been made for Os in extensively altered komatiitic flows (Walker & Nisbet, 2002; Gangopadhyay & Walker, 2003). We therefore suggest that Re and not Os mobility during hydrothermal alteration played a role in the time-integrated  $^{187}\text{Os}/^{188}\text{Os}$  isotope heterogeneity in marginal

and roof zone rocks and that this process has had a minor or insignificant effect on layered series rocks. This conclusion is justified by the low Re/Os ratios of serpentinized dunites in the intrusion relative to unserpentinized dunites, but the similar range in measured and initial  $^{187}\text{Os}/^{188}\text{Os}$  ratios. Variable Os and Nd isotope and PGE compositions of layered series rocks are therefore interpreted as primary magmatic features.

A key question relating to hydrothermal alteration in large mafic–ultramafic intrusions is its timing and extent. Chamberlain (1967) demonstrated that much of the alteration in the Muskox intrusion took place in the ‘core’, and suggested that progressively O-depleted high-temperature ( $\sim 450^\circ\text{C}$ ) fluid fluxed through the intrusion as a consequence of convective heat loss from the cooling cumulate pile—a process not likely to last more than a few hundred thousand to a few million years. Taylor (1968) also invoked hydrothermal activity, but of fluid rich in oxygen in the roof zone of the intrusion, to explain the elevated  $\delta^{18}\text{O}$  values measured in those rocks. These fluid types are not mutually exclusive, as precipitation of S and Re into the upper portions of the intrusion can occur through oxygenation of a low redox fluid flux from the core of the intrusion. However, calculated Re–Os isotope disturbance ‘ages’ (timing from Chondritic Uniform Reservoir at 1270 Ma) for roof zone rocks with negative  $\gamma_{\text{Os,i}}$  imply hydrothermal alteration  $\sim 130$ – $290$  Ma after the formation of the Muskox intrusion. These ages contrast with field evidence for hydrothermal alteration soon after cooling of the intrusion. It is likely that the range in disturbance ‘ages’ is an artefact because  $^{187}\text{Os}/^{188}\text{Os}_m$  is a combination of initial  $^{187}\text{Os}/^{188}\text{Os}$ , magmatic  $^{187}\text{Re}/^{188}\text{Os}$  and elevated  $^{187}\text{Re}/^{188}\text{Os}$  after hydrothermal mobilization and addition of Re. From  $^{187}\text{Os}/^{188}\text{Os}_m$  and the calculated ‘age’ of Re–Os isotope disturbance, the Hornby Bay sandstone has received an  $\sim 50\%$  addition of Re through hydrothermal alteration, whereas the roof rocks with negative  $\gamma_{\text{Os,i}}$  (N-3, N-11, N-14, N-27) have experienced between 10 and 27% Re addition. In combination with undisturbed  $^{187}\text{Os}/^{188}\text{Os}_m$  for layered series rocks that have undergone Re loss, hydrothermal alteration took place within a few million years after the formation of the Muskox intrusion. Hydrothermal alteration was a pervasive process, based on (1) S–Re relationships (Fig. 13), (2) oxygen isotope variations in roof zone whole-rock samples (Taylor, 1968) and (3) systematic serpentinization and presence of native metals in the ‘core’ of the Muskox intrusion, as has also been documented for other layered mafic–ultramafic intrusions (e.g. Marcantonio *et al.*, 1994).

### Crustal assimilation and fractional crystallization

Fluid-immobile elements preserve evidence for crustal contamination effects on Muskox intrusion layered series, marginal and roof zone rocks, including large positive Pb

anomalies (Fig. 6) and oscillating ranges in fluid-immobile element abundances through layered series cyclic units (Fig. 14). Additional evidence for crustal assimilation comes from sulphur (Sasaki, 1969; L. J. Hulbert, unpublished data, 2001), oxygen (Taylor, 1968; this study), Sr and Nd (Stewart & DePaolo, 1992, 1996; this study) isotope compositions in marginal and roof zone rocks. These geochemical signatures correlate with petrological observations such as enhanced modal orthopyroxene along the intrusive contacts and the presence of xenolith country rock material within the marginal zones (Francis, 1994).

It has been noted in previous studies of layered intrusions that lithophile and Os isotope evidence for crustal contamination are rarely consistent, resulting in conflicting interpretations of Os isotope variations as either mantle source heterogeneity (Lambert *et al.*, 1989; Walker *et al.*, 1994, 1995, 1997a, 1997b; Marques *et al.*, 2003), or hydrothermal mobilization (Marcantonio *et al.*, 1994). Discrepancy between lithophile and Os isotope estimates for crustal contamination in mafic magma chambers can be reconciled if the role of fractional crystallization is addressed. Layered series rocks are, by definition, cumulates (Irvine, 1982), and early formed cumulates are generally incompatible-element depleted and compatible-element enriched.

Highly siderophile element, initial Os isotope (Fig. 14) and trace element (Fig. 6) variations with depth from base in the Muskox intrusion layered series cyclic units indicate progressive recharge of mafic magma into the chamber, resulting in fluctuating variations in crustal and mantle isotope signatures. It has been suggested, based upon lithophile element abundances and isotopic compositions, that the layered series was buffered by sealing of the margins by crystal cumulates, and that large-scale contamination was infrequent and/or episodic (Francis, 1994; Barnes & Francis, 1995; Stewart & DePaolo, 1996). The detailed Nd isotope stratigraphy presented in Fig. 7 supports this, with clear spikes in initial Nd isotopic ratios being noted in cyclic units 4, 7 and 19. Muskox intrusion layered series units have low Nd and Sm abundances, making them highly susceptible to small crustal additions. This is exemplified by S-44, a dunite with low Sm and Nd concentrations and the most negative  $\epsilon_{\text{Nd,i}}$  for the layered series, but with relatively unradiogenic initial  $^{187}\text{Os}/^{188}\text{Os}$ . Such large variations in Sm and Nd abundances result in overestimates of the amount of crustal assimilation that has taken place relative to higher abundance samples such as those from the marginal and roof zones. Conversely, Os is a compatible element relative to Sm and Nd, and is at high abundances in cumulate rocks relative to the parental magmas. This leads to the paradoxical relationship of crustal contamination greatly affecting Os isotopes but having more limited impact on the Nd isotope compositions of the marginal and roof zone rocks, with the opposite being

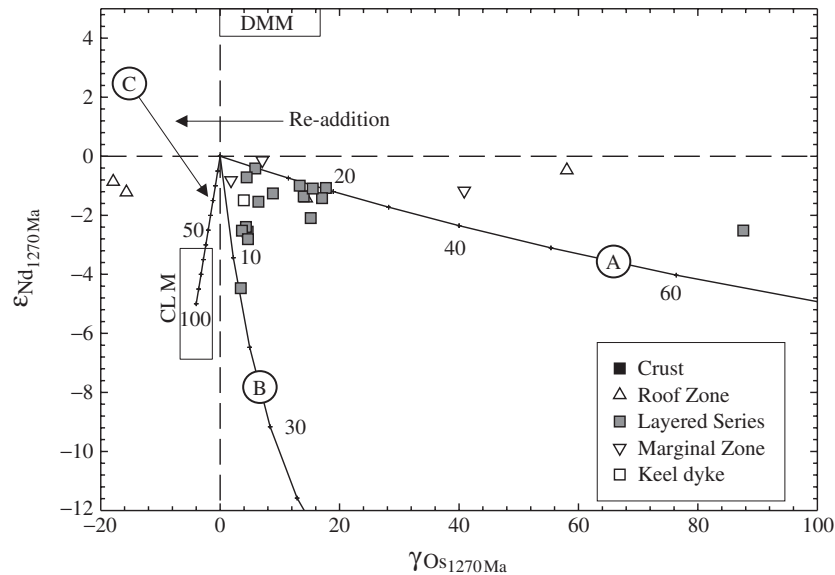


**Fig. 17.**  $\epsilon_{\text{Nd}}^{1270\text{Ma}}$  vs  $\gamma_{\text{Os}}^{1270\text{Ma}}$  diagram illustrating the effects of crustal contamination on the isotopic composition of Muskox intrusion rocks. Primary magma composition assumes  $[\text{Nd}] = 30$  ppm,  $[\text{Os}] = 1$  ppb (based on Marques *et al.*, 2003), and broadly chondritic  $\epsilon_{\text{Nd}}$  and  $\gamma_{\text{Os}}$ . Curves indicate binary mixing between primary magma and the following: A, Wopmay paragneiss,  $[\text{Nd}] = 11.2$  ppm,  $[\text{Os}] = 0.2$  ppb,  $\epsilon_{\text{Nd}} = -8.7$ ,  $\gamma_{\text{Os}} = 240$ ; B, granitic and sedimentary country rock,  $[\text{Nd}] = 50$  ppm,  $[\text{Os}] = 0.05$  ppb,  $\epsilon_{\text{Nd}} = -20$ ,  $\gamma_{\text{Os}} = 400$ ; C, continental lithospheric mantle (CLM), which is assumed to have identical Nd and Os abundances and  $\epsilon_{\text{Nd}} = -5$ ,  $\gamma_{\text{Os}} = -4$ . Fractional crystallization plays a fundamental role in the distribution of different elements in cumulate and evolved magmas such that mixing curves will not be unique. For example, higher  $[\text{Nd}]$  or lower  $[\text{Os}]$  will result in strongly convex curves for mixing model A and concave curves for low  $[\text{Nd}]$  or high  $[\text{Os}]$  abundances in primary magma relative to the crustal assimilant. Values for crust and CLM are from this study, Stewart & DePaolo (1996) and Pearson *et al.* (2003). Primary magmatic values are estimated from initial isotopic values from this study and Stewart & DePaolo (1996). Labels along the curves denote per cent increments of crustal addition. A number of marginal and roof zone samples lie at extremely negative  $\gamma_{\text{Os}}$  because of post-magmatic Re addition. For the Muskox intrusion there is no evidence of sub-continental lithospheric mantle (CLM) melting to source magmatism, suggesting that the Mackenzie LIP was almost exclusively sourced from the asthenospheric mantle. DMM, depleted MORB mantle.

true for high Os abundance, low REE abundance layered series rocks.

The difference in Os and Nd behaviour in the cumulate rocks, and the resultant over- or underestimation of contamination, can be illustrated using Os–Nd isotope relations for the Muskox intrusion. Because Os and Nd isotopes have been analysed for different types of crustal host rocks constraints can potentially be placed on assimilation processes acting on the Muskox intrusion parental magmas. Model calculations for Os–Nd isotope variations indicate that substantial crustal additions (2–70%) to Muskox intrusion marginal and roof zone rocks may have occurred (Fig. 17). For layered series rocks, up to 20% crustal assimilation can be modelled from their Os and Nd isotope systematics, with up to 70% in one extreme case (Fig. 17). Such excessive amounts of calculated assimilation would not yield cumulate rocks dominated by olivine, as observed. Thus, although Os–Nd relationships demonstrate that at least two crustal contaminants are required, which can correspond to Hornby Bay sandstone roof rock and Wopmay paragneiss, they do not show agreement in the amounts of crustal assimilation between Os and Nd.

To more effectively model the effect of crustal assimilation on the layered series rocks we have estimated the

initial concentration of the Muskox parental melts by assuming an Os concentration equal to that of gabbro norites thought to represent parental liquids ( $\sim 0.6$  ppb, Barnes & Francis, 1995) and a chondritic initial  $^{187}\text{Os}/^{188}\text{Os}$  ( $\text{Re}/\text{Os}^* = \sim 0.08$ ,  $\gamma_{\text{Os}} = 0$ ) (Fig. 18). The model uses estimated parental melt abundance and not abundances of elements for cumulate rocks. Despite the absence of definitively ‘uncontaminated’ chilled margin samples for the Muskox intrusion (Bhattacharji & Smith, 1964), we justify the use of the gabbro norites as a proxy for the parental melt Os composition based on calculations presented later in the discussion. The model in Fig. 18 shows mixing curves for an assimilation and fractional crystallization (AFC) ratio ( $M_{\text{Assimilant}}/M_{\text{Magma}}$ ) of 0.8 and an Os bulk  $D$  of 15, indicating that 2–4% contamination by upper crustal gneisses or crustal granulites can explain the entire range of Os isotope variation observed in the layered series. For AFC ratios of 0.2 or unity, 16 and 22% assimilation would be required, respectively. These two extreme AFC scenarios are unrealistic in that extreme contamination or fractionation levels are greatly at odds with the overall ultramafic nature of the intrusion, but they may be locally relevant to some layered series and marginal zone units.

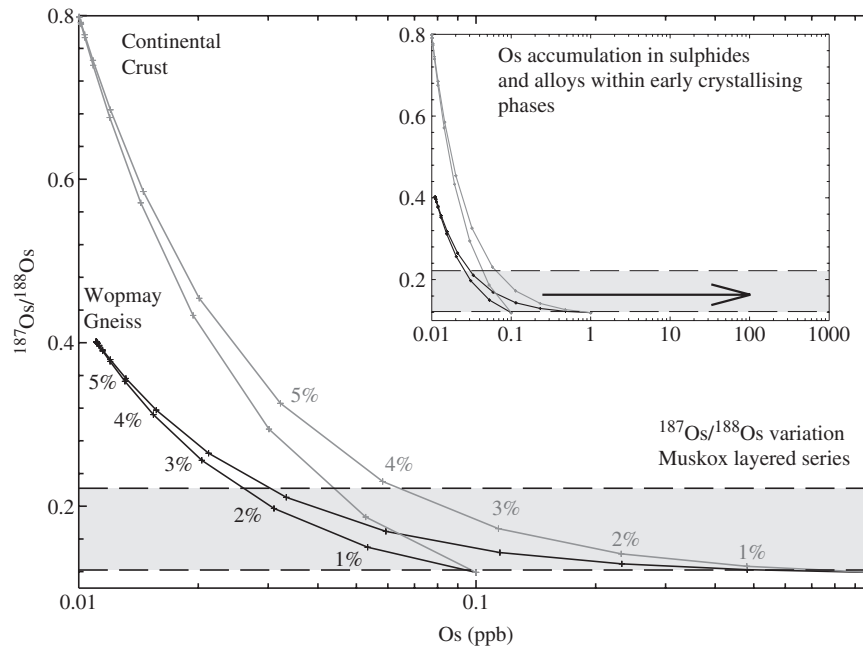


**Fig. 18.** Calculated initial  $^{187}\text{Os}/^{188}\text{Os}$  vs Os. Model to show the effect of crustal assimilation and concomitant fractional crystallization on Muskox melts. This model indicates that, with a fractional crystallization to assimilation ratio of 0.8, <3% crustal addition of Wopmay gneiss and <5% crustal addition of continental crust (Saal *et al.*, 1998) can explain the entire Os variation in the Muskox intrusion layered series units. Subsequent accumulation of Os would result in the high Os concentrations seen in the layered series rocks. If the ratio of fractional crystallization to assimilation decreases the amount of contamination proportionally increases and if the ratio increases less contamination is required. Variation of  $^{187}\text{Os}/^{188}\text{Os}$  measured in layered series peridotites is shown as a grey band. These results demonstrate that  $^{187}\text{Os}/^{188}\text{Os}$  is not impervious to crustal contamination effects if contamination occurred prior to pre-concentration of Os in the cyclic units.

Minor crustal contributions are consistent with the restricted range in  $\epsilon_{\text{Nd}i}$  and trace element variations for the majority of layered series rocks, especially if assimilation of granitic country rocks with elevated Nd abundances and strongly negative  $\epsilon_{\text{Nd}i}$  are considered (see Stewart & DePaolo, 1996). The  $\delta^{18}\text{O}$  values of minerals (as low as +5.5‰), are also consistent with a limited amount of crustal contamination (generally <10% assuming crustal assimilation with  $\sim +11\%$ ; Taylor, 1968). This degree of crustal contamination can explain the entire range in initial  $^{187}\text{Os}/^{188}\text{Os}$  calculated for layered series rocks, and the supra-chondritic  $\gamma_{\text{Os}}$  calculated from the Re–Os errorchron (Fig. 15).

Estimates of crustal assimilation indicate that the layered series are significantly less contaminated than most of the marginal and roof zone rocks. Hence, layered series rocks, along with the Keel dyke, offer the most potential for constraining the isotopic characteristics of the Muskox intrusion parental melt. However, in addition to crustal contamination in the intrusion itself (upper crustal levels), as discussed above, there is also potential for crustal assimilation in the lower portions of the magmatic plumbing system (lower crustal levels). Magmas feeding the intrusion were mafic in character with high Os abundances (probably >0.5 ppb), compared with 3–200 ppt for lower crustal rocks (Saal *et al.*, 1998), requiring in excess of

$\sim 5\%$  lower crustal level assimilation to significantly affect the Os compositions. Although Pb anomalies are pervasive, even in the Keel dyke (Fig. 6), assimilation of large quantities of lower crustal material would have significantly affected the mafic character, through fractionation of the magma, as well as yielding high initial  $\gamma_{\text{Os}}$  values and negative initial  $\epsilon_{\text{Nd}}$  because of the incompatible element enriched nature of continental crust.

### Determination of a Muskox parental melt composition

We interpret variations in both  $\gamma_{\text{Os}}$  and  $\epsilon_{\text{Nd}}$  in the layered series to reflect small but significant upper crustal level contributions to fresh pulses of mantle-derived magma that generated the layered series cyclic units; the initial values presented below are therefore minimum estimates of the Mackenzie LIP mantle source composition. Calculated  $^{187}\text{Os}/^{188}\text{Os}$  and  $^{143}\text{Nd}/^{144}\text{Nd}$  initial isotope values for primitive Muskox intrusion magmas are chondritic to slightly supra-chondritic ( $\gamma_{\text{Os}i} \leq +1.2 \pm 0.3$ ,  $\epsilon_{\text{Nd}i} \geq -1.0 \pm 0.4$ ). Oxygen isotope ratios of fresh minerals, which are not susceptible to the alteration observed in whole-rocks (Taylor, 1968) have  $\delta^{18}\text{O}$  close to typical mantle peridotite ( $\sim +5.5\%$ ). Fractional crystallization has played a key role in generating the relationships between HSE abundance and depth in the Muskox

intrusion (Fig. 14). Indeed, much of the variation in HSE patterns for the Muskox layered series rocks can be explained by the different compatibilities of I-PGE and P-PGE during fractionation of Muskox parental magmas. There is limited evidence for crustal assimilation affecting HSE patterns in layered series rocks (Fig. 12), apart from in roof zone rocks that possess similar patterns to the Hornby Bay sandstone and Wopmay paragneiss country rocks. Roof zone samples also show a surprisingly restricted range in Re, possibly consistent with Re addition through hydrothermal mobilization. The HSE patterns in Fig. 12 therefore reflect the interplay of fractionation of cumulus minerals with relatively minor contributions from assimilation of crustal materials, Re mobilization and, in the case of the marginal zone, base metal sulphide fractionation.

Assuming a primitive magma composition of ~13–15 wt % MgO, based on the break in slope for plots of compatible elements (Cr) vs MgO (Fig. 9) and the estimate of Francis (1994) for magmas in equilibrium with olivine in the intrusion, it is possible to calculate an average initial parental magma composition for the Muskox intrusion. The calculated initial parental magma composition for the Muskox intrusion is 0.5–1.1 ppb Os, 0.4–0.8 ppb Ir, 5.0–5.9 ppb Ru, 11.8–14.2 ppb Pt, 19.0–20.7 ppb Pd and 0.5 ppb Re. With the exceptions of the P-PGE, these estimated values are close to those of low-S gabbro norites from the marginal zone of the intrusion (0.6 ppb Os, 0.6 ppb Ir, 1.2 ppb Ru, 11.4 ppb Pt, 13.4 ppb Pd; Barnes & Francis, 1995), which have ~15 wt % MgO, consistent with the calculated parental liquid of Francis (1994). These values are lower than for the Keel dyke samples, which are partial cumulates. The estimated initial melt compositions for Mackenzie LIP magmas are consistent with >15% partial melting (e.g. Keays, 1995; Rehkämper *et al.*, 1999) and a lack of residual sulphide in the mantle source.

### Magma mixing and the formation of stratiform chromitites and PGE-rich sulphides

Numerous models have been proposed for the formation of stratiform chromitite deposits in layered intrusions, including liquid immiscibility, increase in oxygen activity or pressure, original (high-Cr) magma compositions, or magma mixing and crustal contamination (Marques *et al.*, 2003, and references therein). The Muskox intrusion is the type locality for the long-standing petrological model that invokes mixing between more primitive mafic and more fractionated, crustally contaminated and silica-rich, magmas, forcing chromite crystallization (Irvine, 1975, 1977). Single chromite crystals within the Muskox main chromitites contain small (<50 µm) silicate inclusions (>60 wt % SiO<sub>2</sub>; Irvine, 1977), which indicate that magma mixing between a mafic and a contaminated silicic magma end-member occurred to form the

stratiform chromite deposits. Subsequent studies on melt inclusions in chromites from the Stillwater intrusion underlined the possible role of crustal contamination as a driving force for chromitite mineralization (Spandler *et al.*, 2005).

Our new Re–Os isotope data are consistent with the model of Irvine (1975, 1977) for the generation of Muskox chromitites. Chromitites and Os-rich dunites are characterized by low Re/Os\*, but anomalously high  $\gamma_{Os,i}$  (+12.7 to +86.5), which stand out against background  $\gamma_{Os,i}$  values that are generally less than +5 in the adjacent layered series rocks. These elevated initial Os isotope ratios are best explained by introduction of radiogenic crustal Os into the system from which the chromitites were formed. Based on our mixing calculations, accounting for Os abundances in the melt, as little as 4% crustal addition to the silicic melt can account for the radiogenic Os measured in the chromitites (Fig. 18). This estimate seems reasonable considering the close correspondence of REE and multi-element patterns between whole-rock chromitites and Keel dyke samples (Figs 5 and 6).

Chromitite ores in other layered intrusions vary in their initial Os isotope ratios. Those from the 2.06 Ga Bushveld ( $\gamma_{Os,i}$  = +10 to +55; Schoenberg *et al.*, 1999) and 2.70 Ga Stillwater ( $\gamma_{Os,i}$  = +12 to +34; Lambert *et al.*, 1994) intrusions are elevated, similar to the Muskox intrusion, indicating a significant crustal component involved in their petrogenesis. Even layered intrusions with lower initial Os isotope ratios such as the 2.58 Ga Great Dyke ( $\gamma_{Os,i}$  = –6.9 to +4.4; Schoenberg *et al.*, 2003) and the 2.04 Ga Ipueira–Medrado sill ( $\gamma_{Os}$  = –4.6 to +3.3; Marques *et al.*, 2003) are considered to have significant fractions of crustal input, but in the case of Ipueira–Medrado, into a magma with a component sourced from depleted continental lithosphere, which moderates the resulting Os isotope compositions. Hence, in many PGE-mineralized stratiform chromitite occurrences studied to date there appears to be an important role for magma mixing and contamination by continental crust.

The great majority of mafic–ultramafic systems host marginal zone (side-wall) Cu–Ni–PGE deposits as a consequence of assimilation of crust, or crust-derived sulphur, into sulphide-undersaturated basaltic, picritic or komatiitic magmas (Keays, 1995; Foster *et al.*, 1996; Lambert *et al.*, 1998, 1999). Our new Os isotope and HSE data preclude significant sulphide saturation and immiscible base metal sulphide ore formation in the layered series; these processes are more likely to occur in the marginal zones. One marginal zone sample analysed in this study (S-192) yielded ~22 ppm Pd. Similarly, Barnes & Francis (1995) measured a number of sulphide-rich marginal zone samples with high PGE concentrations, including one with as much as 7 ppm Pt and 84 ppm Pd. Ni–Cu–PGE ores from layered

intrusions such as those of Noril'sk, Voisey's Bay or Sudbury, which have supra-chondritic  $\gamma_{\text{Os}}$ , have most commonly been interpreted as forming through sulphide saturation and immiscible sulphide ore formation processes. Campbell & Naldrett (1979) have defined the R-factor, which is the effective mass of silicate magma with which a given mass of sulphide magma has equilibrated (Campbell & Naldrett, 1979). Examples of marginal zone sulphide ores with high Re/Os\* and  $\gamma_{\text{Os}}$  include those of Voisey's Bay (Lambert *et al.*, 1999), Duluth (Ripley *et al.*, 1998) and the Sudbury igneous complex (e.g. Morgan *et al.*, 2002).

Because limited crustal sulphide addition occurred within the Muskox intrusion layered series rocks and sulphide addition from country rocks was significant only for magmas in the marginal and roof zones, the layered series of the intrusion do not conform to an R-factor model. Locally, however, marginal zone rocks in the Muskox intrusion may conform to an R-factor model. Barnes & Francis (1995) convincingly argued that the silicate to sulphur ratio dominated the formation of sulphide ores in the marginal zone of the intrusion, with sulphur isotope data (Sasaki, 1969; L. J. Hulbert, unpublished data, 2001) demonstrating the provision of S from assimilation of S-rich country rock. However, local Wopmay paragneiss and, by virtue of their similar Os concentrations and  $^{187}\text{Os}/^{188}\text{Os}$  compositions, lower crustal rocks (Saal *et al.*, 1998) are unable to explain the trends to sulphide enrichment seen in Ni–Cu–PGE side-wall deposits. This observation suggests that some intrusions will trend to greater Os (and therefore precious metal) enrichment if sulphide-rich, high Re/Os lithologies are present in the country rock formations that they intrude. For example, sulphide over-saturation in the Noril'sk intrusion, which has generated some of the most PGE-rich sulphide ores globally, is primarily attributed to assimilation of sulphide-rich anhydrite into the primary magmas (e.g. Arndt *et al.*, 2003). It is therefore likely that precious- and base-metal mineralization in the Muskox intrusion is entirely hosted in localized, sulphur-rich side-wall deposits.

### Absence of a continental lithospheric mantle component

Continental lithospheric mantle (CLM) has been invoked as an important source input to the Stillwater Complex (Lambert *et al.*, 1994) and the Ipueira–Medrado sill (Marques *et al.*, 2003). The Muskox intrusion has intruded through an area of 1.6–1.9 Ga basement 80 km west of the Slave craton. Kimberlite-borne peridotite fragments of the Slave CLM exhibit signs of metasomatic Os isotope disturbance at the time of Mackenzie LIP inception (Irvine *et al.*, 2003), indicating that interaction between asthenospheric melts and lithosphere may have taken place. The input of CLM into Muskox magmas would have its

clearest manifestation in the resulting Os isotope signatures. Larsen *et al.* (2003) identified the influence of CLM in the magmatic system developed beneath West Greenland during the evolution of the Palaeocene North Atlantic LIP via the development of unradiogenic initial Os isotope signatures ( $\gamma_{\text{Os}i}$  –2.2 to –16). The lowest  $\gamma_{\text{Os}i}$  value for unaltered Muskox layered series rocks and the Keel dyke is +1.2. The extent to which this process affected Muskox intrusion magmas must therefore have been extremely limited. The close to chondritic  $\epsilon_{\text{Nd}i}$  compositions and the lack of suitable combined Os–Nd isotope trends (Fig. 17) imply that the CLM did not play a significant role in the generation of the Muskox intrusion, or in its mineralization. Instead, the generation of large volumes of tholeiitic melt associated with the Mackenzie LIP would require significant thinning of any existing CLM, acting to reduce its influence. Absence of CLM signatures in Muskox intrusion rocks is consistent with other studies suggesting that some LIP magmas pass through the CLM without appreciable modification (Schoenberg *et al.*, 2003).

### The Muskox intrusion mantle source

Crustal assimilation and magma chamber processes can fully account for the range of Os and Nd isotope compositions of Muskox intrusion rocks. The least contaminated samples yield  $\gamma_{\text{Os}i}$  values close to chondritic and  $\delta^{18}\text{O}$  similar to modern-day mantle rocks. Furthermore, regressions of HSE data indicate melting of an undepleted mantle source. The chondritic to slightly radiogenic  $\gamma_{\text{Os}i}$  and  $\epsilon_{\text{Nd}i}$  values of Muskox parental melts imply a convecting mantle source for the portion of the Mackenzie LIP event represented by the Muskox intrusion, as previously suggested by Stewart & DePaolo (1996). The coeval Coppermine River CFB has an initial Os isotope ratio that is within error of our estimate for the Muskox initial ratio (Day *et al.*, in preparation), suggesting a relatively homogeneous source for the Mackenzie LIP as a whole. This close-to-chondritic estimate of source composition is similar to that of Archaean intraplate ultramafic rocks, komatiites, and some Phanerozoic CFB (Allègre *et al.*, 1999; Schaefer *et al.*, 2000; Puchtel *et al.*, 2001, 2004; Bennett *et al.*, 2002; Gangopadhyay & Walker, 2003; Wilson *et al.*, 2003). We note, however, that there is no discrepancy between long-term incompatible element depletion from Nd isotope systematics and undepleted characteristics for Os isotopes in the Muskox intrusion mantle source, unlike that for some komatiitic mantle sources (Gangopadhyay & Walker, 2003). The  $\gamma_{\text{Os}i}$  of Mackenzie LIP magmatism determined from the Muskox intrusion represents a useful tie-point in the Os isotopic evolution of Earth's mantle. Few mafic–ultramafic lavas and related rocks from the mid-Proterozoic have been studied extensively, or are well preserved. Only one other point lies close to the inferred Os isotope mantle evolution curve in the period between 0.6 and 2 Ga; the 1.1 Ga

Keewenawan CFB, which is considered to originate from an 'enriched' plume source ( $\gamma_{\text{Os}} +5.4$ ; Shirey, 1997).

The estimated Muskox intrusion parental melt composition is plotted versus time in Fig. 19 together with the averages of ophiolite chromitites, abyssal peridotites, komatiites, chondrites (carbonaceous, enstatite and ordinary), estimates for primitive upper mantle (PUM) from global studies of mantle xenoliths, and the Solar System initial (SSI). A large number of layered intrusions and LIPs deviate from the chondritic evolution line to more radiogenic  $^{187}\text{Os}/^{188}\text{Os}$ , suggesting a supra-chondritic Re/Os source. However, many of these layered intrusions (and associated CFB) are either likely to have been, or are demonstrably, contaminated with crustal material and therefore their use in delineating the PUM mantle evolution curve is contentious. In other cases, an outer core (Walker *et al.*, 1997a), or recycled oceanic crust contributions (Shirey, 1997) have been proposed to explain some of the deviations. Therefore, using a filtered dataset reflecting only errorchron or isochron initial values that are unambiguously unaffected by crustal contamination allows determination of the Os isotopic compositions of the contemporary mantle. A regression line through SSI and the Mackenzie LIP source intersects the present day at  $^{187}\text{Os}/^{188}\text{Os} = 0.1296 \pm 0.0071$  in agreement with PUM estimates ( $0.1296 \pm 0.0008$ ; Meisel *et al.*, 2001) (Fig. 19). This requires that the source of the Mackenzie LIP evolved with a  $^{187}\text{Re}/^{188}\text{Os}$  similar to that of PUM.

### Generation of the Muskox intrusion and Mackenzie LIP

Geochemical variations in the Muskox intrusion highlight the importance of crustal assimilation processes at all levels within continental intraplate magmatic systems. In the case of the Muskox intrusion, it is possible to 'see through' the effects of crustal contamination and magma chamber processes, allowing estimation of the source composition of the magmas feeding the Mackenzie LIP. The observation of an undepleted asthenospheric mantle source for the Muskox intrusion is consistent with the notion of an anomalous mantle upwelling model for the generation of the Mackenzie LIP. The large volume of magma produced during the relatively short period of time determined for the Mackenzie LIP (LeCheminant & Heaman, 1989), the high degrees of partial melting (>15%), the presence of high MgO and Mg/Fe lavas in the early phases of magmatism (Day *et al.*, in preparation), the uplift–subsidence history, and the topographic drainage and gravity structure of the region (Baragar *et al.*, 1996), which coincides with the focal point of Mackenzie dyke propagation (Ernst & Baragar, 1992), all appear to indicate anomalous mantle melting, possibly related to failed rifting (Fahrig, 1987). The undepleted source composition is similar to estimated PUM compositions (Becker *et al.*, 2006). The source for the Muskox intrusion parental

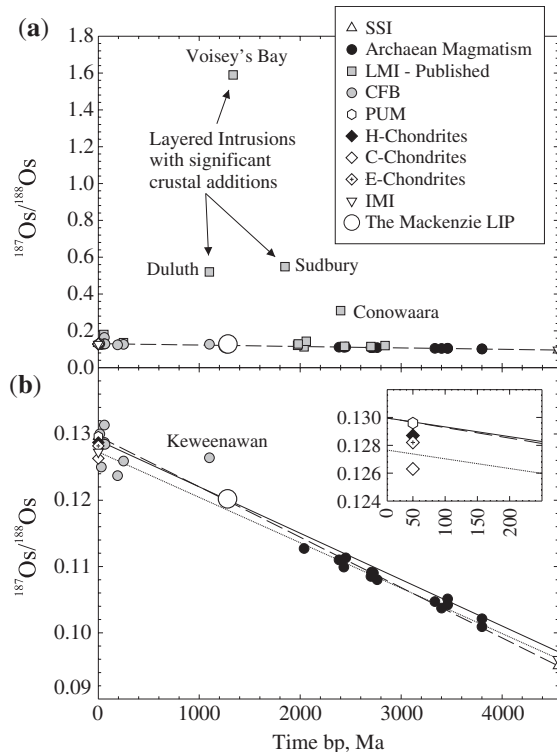


**Fig. 19.** Evolution diagram of  $^{187}\text{Os}/^{188}\text{Os}$  vs time for selected mantle-derived materials, chondrites, Solar System initial (SSI) and iron meteorite initial (IMI). (a) Dashed line represents regression line through SSI (Shirey & Walker, 1998) and that of the Mackenzie LIP source. (b) Crustally contaminated LMI and CFB removed from plot; dotted line, IMI composition regression; dashed line, SSI composition regression. Mackenzie LIP have Keel (+1.2) and layered series ( $\sim 0$ ) initial  $\gamma_{\text{Os}}$ . These models indicate that chondritic  $^{187}\text{Os}/^{188}\text{Os}$  compositions have been a feature of the mantle source for intraplate magmatism and mantle-derived melts for at least 3.8 Gyr (Bennett *et al.*, 2002), until at least the mid-Proterozoic. Keewenawan samples appear anomalous and are associated with the demonstrably crustally contaminated Duluth intrusion. Data sources: Shirey & Walker (1998) and Puchtel *et al.* (2004), and references therein. LMI, layered mafic intrusions; CFB, continental flood basalts; PUM, primitive upper mantle.

magmas therefore appears to be derived from a region of mantle that has not previously witnessed significant melt extraction, and is consistent with the concept of a deep mantle upwelling or 'plume' beneath the Canadian Shield during the mid-Proterozoic. Results of this study do not support notions of recycled or core contributions to the Mackenzie LIP.

### CONCLUSIONS

Detailed study of trace elements, platinum-group elements, and Re–Os, Sm–Nd and O isotope systematics through the stratigraphy of the Muskox layered intrusion reveals the complex interplay of magma chamber processes, as inferred for layered intrusions world-wide. Post-magmatic hydrothermal alteration has resulted in redistribution of

Re in the intrusion affecting initial Os isotope values in marginal and roof zone samples, but has had a negligible effect on the layered series units or the Muskox Keel feeder dyke. Crustal contamination has played a fundamental role in generating the range of Os isotope compositions measured within the layered series, marginal and roof zones of the intrusion. Crustal contamination via wall-rock assimilation is best exemplified in the roof zone of the intrusion. Limited crustal assimilation has taken place in the layered series but a small amount (<4% by weight) of crustal contamination, in conjunction with crystal fractionation, can explain the entire range in isotopic and elemental variations seen in the cyclic units. Ultimately, crustal assimilation may provide a trigger mechanism for the formation of chromitite horizon precious metal deposits via interaction with fresh, mantle-derived magma pulses into the intrusion, and also for side-wall sulphide deposits by providing sulphur to the system. Accounting for the effects of crustal assimilation, least contaminated samples and errorchron initial values indicate an undepleted source composition ( $\gamma_{Os} \leq +1.2 \pm 0.3$ ;  $\epsilon_{Nd} > -1.0$ ;  $\delta^{18}O \sim +5.5\%$ ). This composition is slightly supra-chondritic relative to carbonaceous chondrites but is similar to estimates of the primitive upper mantle at 1.27 Ga. The Muskox intrusion and Mackenzie LIP were probably sourced from asthenospheric mantle material unaffected by long-term, large-scale melt depletion, consistent with an anomalous mantle melting event beneath present-day Canada during the mid-Proterozoic.

## ACKNOWLEDGEMENTS

We thank D. Lowry and D. Matthey for their help in obtaining the oxygen isotope values presented in this paper, and G. M. Nowell and C. J. Ottley for technical assistance with plasma mass spectrometry. We are particularly grateful for critical comments by S. J. Barnes, M. Wilson, R. W. Carlson and two anonymous reviewers, and informal comments by T. Yokoyama, which have helped to improve the focus of this work. This study was conducted as part of a Natural Environment Research Council (UK) funded PhD scholarship (NER/S/A/2000/03304), a Society of Economic Geologists Canada Foundation Award, and the Edgar Pam Fellowship (Institute of Material, Minerals and Mining, UK) to J.M.D.D.

## REFERENCES

- Allègre, C. J., Birc, J.-L., Capmas, F. & Courtillot, V. (1999). Age of the Deccan traps using  $^{187}\text{Re}$ – $^{187}\text{Os}$  systematics. *Earth and Planetary Science Letters* **170**, 197–204.
- Arndt, N. T., Czamanske, G. K., Walker, R. J., Chauvel, C. & Fedorenko, V. A. (2003). Geochemistry and origin of the intrusive hosts of the Noril'sk–Talnakh Cu–Ni–PGE sulphide deposits. *Economic Geology* **98**, 494–515.
- Baragar, W. R. A. (1969). *The Geochemistry of the Coppermine River Basalts*. Geological Survey of Canada Paper **69-44**, 43 pp.
- Baragar, W. R. A., Ernst, R. E., Hulbert, L. & Peterson, T. (1996). Longitudinal petrochemical variation in the Mackenzie dyke swarm, Northwestern Canadian Shield. *Journal of Petrology* **37**, 317–359.
- Barnes, S.-J. & Francis, D. (1995). The distribution of platinum-group elements, nickel, copper, and gold in the Muskox layered intrusion, Northwest Territories, Canada. *Economic Geology* **90**, 135–154.
- Barnes, S. J., Naldrett, A. J. & Gorton, M. P. (1985). The origin of the fractionation of platinum-group elements in terrestrial magmas. *Chemical Geology* **53**, 303–323.
- Barnes, S.-J., Cox, R. A. & Zientek, M. L. (2006). Platinum-group element, gold, silver and base metal distribution in compositionally zoned sulphide droplets from the Medvezky Creek mine, Noril'sk, Russia. *Contributions to Mineralogy and Petrology* **152**, 187–200.
- Barnes, S.-J., Prichard, H. M., Cox, R. A., Fisher, P. C. & Godel, B. (2008). The location of the chalcophile and siderophile elements in platinum-group element ore deposits (a textural, microbeam and whole rock geochemical study): Implications for the formation of the deposits. *Chemical Geology* **248**, 295–317.
- Becker, H., Horan, M. F., Walker, R. J., Gao, S., Lorand, J.-P. & Rudnick, R. L. (2006). Highly siderophile element composition of the Earth's primitive upper mantle: Constraints from new data on peridotite massifs and xenoliths. *Geochimica et Cosmochimica Acta* **70**, 4528–4550.
- Bennett, V. C., Nutman, A. P. & Esat, T. M. (2002). Constraints on mantle evolution from  $^{187}\text{Os}/^{188}\text{Os}$  isotopic compositions of Archaean ultramafic rocks from southern West Greenland (3.8 Ga) and Western Australia (3.46 Ga). *Geochimica et Cosmochimica Acta* **66**, 2615–2630.
- Bhattacharji, S. & Smith, C. H. (1964). Flowage differentiation. *Science* **145**, 150–153.
- Birc, J.-L., Roy-Barman, M. & Capmas, F. (1997). Re–Os isotopic measurements at the femtomole level in natural samples. *Geostandards Newsletter* **21**, 21–28.
- Bowring, S. A. & Ross, G. M. (1985). Geochronology of the Narakay Volcanic Complex: implications for the age of the Coppermine Homocline and Mackenzie Igneous events. *Canadian Journal of Earth Science* **22**, 774–781.
- Campbell, I. H. & Naldrett, A. J. (1979). The influence of silicate/sulphide ratios on the geochemistry of magmatic sulphides. *Economic Geology* **74**, 1503–1505.
- Chamberlain, J. A. (1967). Sulfides in the Muskox intrusion. *Canadian Journal of Earth Science* **4**, 105–154.
- Chamberlain, J. A. & Delano, R. N. (1965). Mackinawite and vallerite in the Muskox Intrusion. *American Mineralogist* **50**, 682–695.
- Chamberlain, J. A., McLeod, C. R., Traill, R. J. & Lachance, G. R. (1965). Native metals in the Muskox intrusion. *Canadian Journal of Earth Science* **2**, 188–215.
- Cohen, A. S. & Waters, F. G. (1996). Separation of osmium from geological materials by solvent extraction for analysis by thermal ionisation mass spectrometry. *Analytica Chimica Acta* **332**, 269–275.
- Crocket, J. H. (2002). Platinum-group element geochemistry of mafic and ultramafic rocks. In: Cabri, L. J. (ed.) *The Geology, Geochemistry, Mineralogy and Mineral Beneficiation of Platinum-Group Elements*. Canadian Institute of Mining Special Volume **54**, 177–210.
- Day, J. M. D., Pearson, D. G. & Nowell, G. M. (2003a). High precision rhenium and platinum isotope dilution analyses by plasma ionisation multi-collector mass spectrometry. In: Holland, J. G. & Tanner, S. D. (eds) *Plasma Source Mass Spectrometry: Applications and Emerging Technologies*. London: Royal Society of Chemistry, pp. 374–390.

- Day, J. M. D., Hulbert, L. J., Pearson, D. G. & Nowell, G. M. (2003b). Re–Os isotopic study of the Muskox intrusion, NWT, Canada. *Geophysical Research Abstracts* **5**, number 06848.
- Dowall, D. P., Nowell, G. M. & Pearson, D. G. (2003). Chemical pre-concentration procedures for high-precision analyses of Hf–Nd–Sr isotopes in geological materials by plasma ionisation multi-collector mass spectrometry (PIMMS) techniques. In: Holland, J. G. & Tanner, S. D. (eds) *Plasma Source Mass Spectrometry: Applications and Emerging Technologies*. London: Royal Society of Chemistry, pp. 321–337.
- Eales, H. V. & Cawthorn, R. G. (1996). The Bushveld Complex. In: Cawthorn, R. G. (ed.) *Layered Intrusions*. Amsterdam: Elsevier, pp. 181–230.
- Eiler, J. M., Farley, K. A., Valley, J. W., Hoffman, A. W. & Stolper, E. M. (1996). Oxygen isotope constraints on the sources of Hawaiian volcanism. *Earth and Planetary Science Letters* **144**, 453–468.
- Eiler, J. M., Farley, K. A., Valley, J. W., Hauri, E., Craig, H., Hart, S. R. & Stolper, E. M. (1997). Oxygen isotope variations in ocean island basalt phenocrysts. *Geochimica et Cosmochimica Acta* **61**, 2281–2293.
- Eiler, J. M., Schiano, P., Kitchen, N. & Stolper, E. M. (2000a). Oxygen-isotope evidence for recycled crust in the sources of mid-ocean-ridge basalts. *Nature* **403**, 530–534.
- Eiler, J. M., Crawford, A., Elliott, T., Farley, K. A., Valley, J. W. & Stolper, E. (2000b). Oxygen isotope geochemistry of oceanic arc lavas. *Journal of Petrology* **41**, 229–256.
- Ernst, R. E. & Baragar, W. R. A. (1992). Evidence from magnetic fabric for the flow pattern of magma in the Mackenzie giant radiating dyke swarm. *Nature* **356**, 511–513.
- Ernst, R. E., Head, J. W., Parfitt, E., Grosfils, E. & Wilson, L. (1995). Giant radiating dyke swarms on Earth and Venus. *Earth-Science Reviews* **39**, 1–58.
- Fahrig, W. F. (1987). The tectonic settings of continental mafic dyke swarms: failed arm and early passive margin. In: Halls, H. C. & Fahrig, W. F. (eds) *Mafic Dyke Swarms*. Geological Association of Canada Special Paper **34**, 331–348.
- Findlay, D. C. & Smith, C. H. (1965). *The Muskox Drilling Project*. Geological Survey of Canada Paper **64-44**, 170 pp.
- Foster, J. G., Lambert, D. D., Frick, L. R. & Maas, R. (1996). Re–Os isotopic evidence for genesis of Archaean nickel ores from uncontaminated komatiites. *Nature* **382**, 703–706.
- Francis, D. (1994). *Chemical Interaction between Picritic Magmas and Upper Crust along the Margins of the Muskox Intrusion, Northwest Territories*. Geological Survey of Canada Paper **92-12**, 94 pp.
- French, J. E., Heaman, L. M. & Chacko, T. (2002). Feasibility of chemical U–Th–total Pb baddeleyite dating by electron microprobe. *Chemical Geology* **188**, 85–104.
- Gangopadhyay, A. & Walker, R. J. (2003). Re–Os systematics of the ca. 2.7-Ga komatiites from Alexo, Ontario, Canada. *Chemical Geology* **196**, 147–162.
- Hamilton, M. A., Pearson, D. G., Thompson, R. N., Kelley, S. P. & Emeleus, C. H. (1998). Rapid eruption of the Skye lavas inferred from precise U–Pb and Ar–Ar dating of the Run and Cuillin plutonic complexes. *Nature* **394**, 260–263.
- Hanski, E., Walker, R. J., Huhma, H. & Suominen, I. (2001). The Os and Nd isotopic systematics of c. 2.44-Ga Akanvaara and Koitelainen mafic layered intrusions in northern Finland. *Precambrian Research* **109**, 73–102.
- Hart, S. R. & Kinloch, E. D. (1989). Osmium isotope systematics in Witwatersrand and Bushveld ore deposits. *Economic Geology* **84**, 1651–1655.
- Hofmann, P. F. (1980). Wopmay orogen: a Wilson cycle of Early Proterozoic age in the northwest of the Canadian Shield. In: Strangway, D. W. (ed.) *The Continental Crust and its Mineral Deposits*. Geological Association of Canada Special Paper **20**, 523–552.
- Horan, M. F., Morgan, J. W., Walker, R. J. & Cooper, R. W. (2001). Re–Os isotopic constraints on magma mixing in the peridotite zone of the Stillwater complex, Montana, USA. *Contributions to Mineralogy and Petrology* **141**, 446–457.
- Horan, M. F., Walker, R. J., Morgan, J. W., Grossman, J. N. & Rubin, A. E. (2003). Highly siderophile elements in chondrites. *Chemical Geology* **196**, 5–20.
- Irvine, T. N. (1975). Crystallization sequences in the Muskox intrusion and other layered intrusions—II. Origin of chromitite layers and similar deposits of other magmatic ores. *Geochimica et Cosmochimica Acta* **39**, 991–1020.
- Irvine, T. N. (1977). Origin of chromitite layers in the Muskox intrusion and other stratiform intrusions: A new interpretation. *Geology* **5**, 273–277.
- Irvine, T. N. (1980). Magmatic infiltration metasomatism, double-diffusive fractional crystallization, and accumulus growth in the Muskox intrusion and other layered intrusions. In: Hargreaves, R. B. (ed.) *Physics of Magmatic Processes*. Princeton, (NJ): Princeton University Press, pp. 325–383.
- Irvine, T. N. (1982). Terminology for layered intrusions. *Journal of Petrology* **23**, 127–162.
- Irvine, T. N. & Smith, C. H. (1967). The ultramafic rocks of the Muskox intrusion. In: Wyllie, P. J. (ed.) *Ultramafic and Related Rocks*. New York: John Wiley, pp. 20–38.
- Irvine, G. J., Pearson, D. G., Kjarsgaard, B. A., Carlson, R. W., Kopylova, M. G. & Dreibus, G. (2003). A Re–Os and PGE study of kimberlite-derived peridotite xenoliths from Somerset Island and a comparison to the Slave and Kaapvaal cratons. *Lithos* **71**, 461–488.
- Jacobsen, S. B. & Wasserburg, G. J. (1980). Sm–Nd isotopic evolution of chondrites. *Earth and Planetary Science Letters* **50**, 139–155.
- Keays, R. R. (1995). The role of komatiitic and picritic magmatism and S-saturation in the formation of ore deposits. *Lithos* **34**, 1–18.
- Kerans, C., Ross, G. M., Donaldson, J. A. & Geldsetzer, H. J. (1981). Tectonism and depositional history of the Helikian Hornby Bay and Dismal Lake Groups, District of Mackenzie. In: Campbell, F. H. A. (ed.) *Proterozoic Basins of Canada*. Geological Survey of Canada, Paper **81-10**, 157–182.
- Lambert, D. D., Morgan, J. W., Walker, R. J., Shirey, S. B., Carlson, R. W., Zientek, M. L. & Koski, M. S. (1989). Rhenium–osmium and samarium–neodymium isotopic studies of the Stillwater Complex. *Science* **244**, 1169–1174.
- Lambert, D. D., Walker, R. J., Morgan, J. W., Shirey, S. B., Carlson, R. W., Zientek, M. L., Lipin, B. R., Koski, M. S. & Cooper, R. L. (1994). Re–Os and Sm–Nd isotope geochemistry of the Stillwater Complex, Montana: Implications for the petrogenesis of the J-M Reef. *Journal of Petrology* **35**, 1717–1753.
- Lambert, D. D., Foster, J. G., Frick, L. R., Hoatson, D. M. & Purvis, A. C. (1998). Application of the Re–Os isotopic system to the study of Precambrian magmatic sulphide deposits of Western Australia. *Australian Journal of Earth Science* **45**, 265–284.
- Lambert, D. D., Foster, J. G., Frick, L. R., Li, C. & Naldrett, A. J. (1999). Re–Os isotopic systematics of the Voisey's Bay Ni–Cu–Co magmatic ore system, Labrador, Canada. *Lithos* **47**, 69–88.
- Larsen, L. M., Pedersen, A. K., Sundvoll, B. & Frei, R. (2003). Alkali picrites formed by melting of old metasomatized lithospheric mantle: Manitdlat Member, Vaigat Formation, Palaeocene of West Greenland. *Journal of Petrology* **44**, 3–38.
- LeCheminant, A. N. & Heaman, L. M. (1989). Mackenzie igneous events, Canada: Middle Proterozoic hotspot magmatism associated with ocean opening. *Earth and Planetary Science Letters* **96**, 38–48.

- Lowry, D., Appel, P. W. U. & Rollinson, H. R. (2003). Oxygen isotopes of an early Archaean layered ultramafic body, southern West Greenland: implications for magma source and post-intrusion history. *Precambrian Research* **126**, 273–288.
- Ludwig, K. R. (2003). Isoplot. Program and documentation, version 2.95. Revised edition of US Open-File report, 91–445.
- Marcantonio, F., Zindler, A., Reisberg, L. & Mathez, E. A. (1993). Re–Os isotopic systematics in chromitites from the Stillwater Complex, Montana, USA. *Geochimica et Cosmochimica Acta* **57**, 4029–4037.
- Marcantonio, F., Reisberg, L., Zindler, A., Wyman, D. & Hulbert, L. (1994). An isotopic study of the Ni–Cu–PGE-rich Wellgreen intrusion of the Wrangellia Terrane: evidence for hydrothermal mobilisation of rhenium and osmium. *Geochimica et Cosmochimica Acta* **58**, 1007–1017.
- Marques, J. C., Ferreira Filho, C. F., Carlson, R. W. & Pimentel, M. M. (2003). Re–Os and Sm–Nd isotope and trace element constraints on the origin of the chromite deposit of the Ipueira–Medrado sill, Bahia, Brazil. *Journal of Petrology* **44**, 659–678.
- Mattey, D. P. & Macpherson, C. G. (1993). High-precision oxygen isotope microanalysis of ferromagnesian minerals by laser fluorination. *Chemical Geology* **105**, 305–318.
- Mattey, D. P., Lowry, D. & Macpherson, C. (1994). Oxygen isotope composition of mantle peridotite. *Earth and Planetary Science Letters* **128**, 231–241.
- McCandless, T. E. & Ruiz, J. (1991). Osmium isotopes and crustal sources for platinum-group mineralization in the Bushveld Complex, South Africa. *Geology* **19**, 1225–1228.
- McDonough, W. F., Sun, S.-s. (1995). The composition of the Earth. *Chemical Geology* **120**, 223–253.
- Meisel, T. & Moser, J. (2004). Reference materials for geochemical PGE analysis: new analytical data for Ru, Rh, Pd, Os, Ir, Pt and Re by isotope dilution ICP-MS in 11 geological reference materials. *Chemical Geology* **208**, 319–338.
- Meisel, T., Walker, R. J., Irving, A. J. & Lorand, J.-P. (2001). Osmium isotopic compositions of mantle xenoliths: a global perspective. *Geochimica et Cosmochimica Acta* **65**, 1311–1323.
- Morgan, J. W., Walker, R. J., Horan, M. F., Beary, E. S. & Naldrett, A. J. (2002).  $^{190}\text{Pt}$ – $^{186}\text{Os}$  and  $^{187}\text{Re}$ – $^{187}\text{Os}$  systematics of the Sudbury Igneous Complex, Ontario. *Geochimica et Cosmochimica Acta* **66**, 273–290.
- Nier, A. O. (1950). A redetermination of the relative abundances of the isotopes of carbon, nitrogen, oxygen, argon, and potassium. *Physics Reviews* **77**, 789–793.
- Ottley, C. J., Pearson, D. G. & Irvine, G. I. (2003). A routine method for the dissolution of geological samples for the analysis of REE and trace elements via ICP-MS. In: Holland, J. G. & Tanner, S. D. (eds) *Plasma Source Mass Spectrometry: Applications and Emerging Technologies*. London: Royal Society of Chemistry, pp. 221–230.
- Pearson, D. G. & Woodland, S. J. (2000). Solvent extraction/anion exchange separation and determination of PGEs (Os, Ir, Pt, Pd, Ru) and Re–Os isotopes in geological samples by isotope dilution ICP-MS. *Chemical Geology* **165**, 87–107.
- Pearson, D. G. & Nowell, G. M. (2005). Accuracy and precision in plasma ionisation multi-collector mass spectrometry: Constraints from neodymium and hafnium isotope measurements. In: Holland, J. G. & Bandura, D. R. (eds) *Plasma Source Mass Spectrometry, Current Trends and Future Developments*. London: Royal Society of Chemistry, pp. 284–314.
- Pearson, D. G., Canil, D. & Shirey, S. B. (2003). Mantle samples included in volcanic rocks: xenoliths and diamonds. In: Carlson, R. W. (ed.) *Treatise on Geochemistry*, 2. Amsterdam: Elsevier, pp. 171–275.
- Pearson, D. G., Irvine, G. J., Ionov, D. A., Boyd, F. R. & Dreibus, G. E. (2004). Re–Os isotope systematics and platinum-group element fractionation during mantle melt extraction: a study of massif and xenolith peridotite suites. *Chemical Geology* **208**, 29–59.
- Puchtel, I. S., Brüggemann, G. E. & Hofmann, A. W. (1999). Precise Re–Os mineral isochron and Pb–Nd–Os isotope systematics of a mafic–ultramafic sill in the 2.0 Ga Onega plateau (Baltic Shield). *Earth and Planetary Science Letters* **170**, 447–461.
- Puchtel, I. S., Brüggemann, G. E., Hofmann, A. W., Kulikov, V. S. & Kulikova, V. V. (2001). Os isotope systematics of komatiitic basalts from the Vetryny belt, Baltic Shield: evidence for a chondritic source of the 2.45 Ga plume. *Contributions to Mineralogy and Petrology* **140**, 588–599.
- Puchtel, I. S., Brandon, A. D. & Humayan, M. (2004). Precise Pt–Re–Os isotope systematics of the mantle from 2.7-Ga komatiites. *Earth and Planetary Science Letters* **224**, 157–174.
- Rehkämper, M., Halliday, A. N., Fitton, J. G., Lee, D.-C., Wieneke, M. & Arndt, N. T. (1999). Ir, Ru, Pt and Pd in basalts and komatiites: new constraints for the geochemical behaviour of the platinum-group elements in the mantle. *Geochimica et Cosmochimica Acta* **63**, 3915–3934.
- Ripley, E. M., Lambert, D. D. & Frick, L. R. (1998). Re–Os, Sm–Nd and Pb isotopic constraints on mantle and crustal contributions to magmatic sulphide mineralization in the Duluth complex. *Geochimica et Cosmochimica Acta* **62**, 3349–3365.
- Saal, A. E., Rudnick, R. L., Ravizza, G. E. & Hart, S. R. (1998). Re–Os isotope evidence for the composition, formation and age of the lower crust. *Nature* **393**, 58–61.
- Sasaki, A. (1969). *Sulphur Isotope Study of the Muskox Intrusion*, District of Mackenzie. *Geological Survey of Canada Paper* **68-46**, 68 pp.
- Schaefer, B. F., Parkinson, I. J. & Hawkesworth, C. J. (2000). Deep mantle plume osmium isotope signatures from West Greenland Tertiary picrites. *Earth and Planetary Science Letters* **175**, 105–118.
- Schoenberg, R., Kruger, F. J., Nägler, T. F., Meisel, T. & Kramers, J. D. (1999). PGE enrichment in chromitite layers and the Merensky Reef of the Bushveld Complex; a Re–Os and Rb–Sr isotope study. *Earth and Planetary Science Letters* **172**, 49–64.
- Schoenberg, R., Nägler, Th. F., Gnos, E., Kramers, J. D. & Kamber, B. S. (2003). The source of the Great Dyke, Zimbabwe, and its tectonic significance: evidence from Re–Os isotopes. *Journal of Geology* **111**, 565–578.
- Selby, D., Creaser, R. A., Stein, H. J., Markey, R. J. & Hannah, J. L. (2007). Assessment of the  $^{187}\text{Re}$  decay constant by cross calibration of Re–Os molybdenite and U–Pb zircon chronometers in magmatic ore systems. *Geochimica et Cosmochimica Acta* **71**, 1999–2013.
- Shirey, S. B. (1997). Re–Os isotopic composition of Midcontinent rift system picrites: implications for plume–lithosphere interaction and enriched mantle sources. *Canadian Journal of Earth Sciences* **34**, 489–503.
- Shirey, S. B. & Walker, R. J. (1995). Carius tube digestion for low-blank rhenium–osmium analysis. *Analytical Chemistry* **67**, 2136–2141.
- Shirey, S. B. & Walker, R. J. (1998). The Re–Os isotope system in cosmochemistry and high-temperature geochemistry. *Annual Review of Earth and Planetary Sciences* **26**, 423–500.
- Spandler, C., Mavrogenes, J. & Arculus, R. (2005). Origin of chromitites in layered intrusions: Evidence from chromite-hosted melt inclusions from the Stillwater Complex. *Geology* **33**, 893–896.
- Stewart, B. W. & DePaolo, D. J. (1992). Diffusive isotopic contamination of mafic magma and coexisting silicic liquid in the Muskox intrusion. *Science* **255**, 708–711.
- Stewart, B. W. & DePaolo, D. J. (1996). Isotopic studies of processes in mafic magma chambers: III. The Muskox intrusion, Northwest

- Territories, Canada. In: Basu, A. & Hart, S. (eds) *Earth Processes: Reading the Isotopic Code. Geophysical Monograph, American Geophysical Union* **95**, 277–292.
- Sun, S.-s. & McDonough, W. F. (1989). Chemical and isotopic systematics of oceanic basalts: implications for mantle compositions and processes. In: Saunders, A. D. & Norry, M. J. (eds) *Magmatism in the Ocean Basins. Geological Society, London, Special Publications* **42**, 313–345.
- Taylor, H. P., Jr (1968). The oxygen isotope geochemistry of igneous rocks. *Contributions to Mineralogy and Petrology* **19**, 1–71.
- Wager, L. R. & Brown, G. M. (1968). *Layered Igneous Rocks*. Edinburgh: Oliver & Boyd.
- Wager, L. R., Brown, G. M. & Wadsworth, W. J. (1960). Types of igneous cumulates. *Journal of Petrology* **1**, 73–85.
- Walker, R. J. & Nisbet, E. (2002).  $^{187}\text{Os}$  isotope constraints on Archean mantle dynamics. *Geochimica et Cosmochimica Acta* **66**, 3317–3325.
- Walker, R. J., Morgan, J. W., Horan, M. F., Czamanske, G., Krogstad, E. J., Fedorenko, V. A. & Kunilov, V. E. (1994). Re–Os isotopic evidence for an enriched-mantle source for Noril'sk-type, ore bearing intrusions, Siberia. *Geochimica et Cosmochimica Acta* **58**, 4179–4197.
- Walker, R. J., Morgan, J. W. & Horan, M. F. (1995). Osmium-187 enrichment in some plumes: evidence for core–mantle interaction? *Science* **269**, 819–822.
- Walker, R. J., Morgan, J. W., Hanski, E. J. & Smolkin, V. F. (1997a). Re–Os systematics of Early Proterozoic ferropicrites, Penchenga Complex, north western Russia: evidence for ancient  $^{187}\text{Os}$ -enriched plumes. *Geochimica et Cosmochimica Acta* **61**, 3145–3160.
- Walker, R. J., Morgan, J. W., Beary, E. S., Smoliar, M. I., Czamanske, G. K. & Horan, M. F. (1997b). Applications of the  $^{190}\text{Pt}$ – $^{186}\text{Os}$  isotope system to geochemistry and cosmochemistry. *Geochimica et Cosmochimica Acta* **61**, 4799–4807.
- Wilson, A. H., Shirey, S. B. & Carlson, R. W. (2003). Archean ultra-depleted komatiites formed by hydrous melting of cratonic mantle. *Nature* **423**, 858–860.